(U-Th)/He thermochronology of the Aishihik batholith, central Yukon: Evidence for stable crust in the Cretaceous

Meghan Moher

Supervisor: David Schneider, University of Ottawa

A thesis submitted to the Faculty of Graduate and Postdoctoral Studies in partial fulfillment of the requirements for the degree of
Master of Science in Earth Sciences

University of Ottawa
Ottawa, Canada

Abstract

The 190-180 Ma Aishihik batholith is located in southcentral Yukon in the North American Cordillera. Low-temperature (U-Th)/He thermochronology is used to assess the thermal history of the batholith and the surrounding host rock to provide an understanding of the Jurassic-Cretaceous tectonism. The Yukon Tanana terrane (YTT) shows a steady cooling of ~5°C/m.y from the Early Jurassic to the Late Cretaceous, when it reaches the surface. Sections of YTT adjacent to the batholith exhibits moderate cooling rates of 7°C/m.y from the Early to Late Jurassic and then slows down to 1.5°C/m.y until reaching the surface in the Late Cretaceous. The batholith itself exhibits relatively fast cooling from the Early to Late Jurassic (15°C/m.y) and then slows down (1.5°C/m.y) until it reaches surface conditions in the Late Cretaceous. All rocks are at the surface at the latest by the Late Cretaceous with no evidence that there were any subsequent substantial thermal events, which indicates that the Yukon has a mature landscape compared to the rest of the North American Cordillera.

Sommaire

Le batholite Aishihik, datant de 190-180 Ma, est situé au Yukon Sud-central dans la cordillère nord-américaine. La thermochronologie basse température (U-Th)/He est utilisée pour reconstituer l'histoire thermique du batholite et des roches-hôtes environnantes afin de comprendre la tectonique du Jurassique-Crétacé. Le terrane de Yukon-Tanana (YT) démontre un refroidissement constant de ~5°C/ma du Jurassique précoce au Crétacé tardif lorsqu'il atteint la surface. Les sections adjacentes au batholite révèlent un refroidissement modéré à un taux de 7°C/ma commençant au Jurassique précoce à tardif. Par la suite, ce refroidissement a ralenti à un

taux de 1.5°C/ma jusqu'à ce que les roches atteignent la surface pendant le Crétacé tardif. Le batholite démontre un refroidissement relativement rapide du Jurassique précoce à tardif (15°C/ma) suivi d'un ralentissement qui atteint un taux de 1.5°C/ma lorsque les roches atteignent la surface durant le Crétacé tardif. Toutes les roches étaient à la surface au plus tard durant le Crétacé tardif et il n'y a aucune preuve d'autres évènements thermiques substantiels subséquemment. Ces résultats indiquent que le Yukon a un paysage mature par rapport au reste de la cordillère nord-américaine.

Acknowledgements

I would like to thank my supervisor, David Schneider, for his guidance and support throughout the duration of the project. Thank you for all of the opportunities you have given me and for introducing me to thermochronology. I thank the Geological Survey of Canada (Vancouver and Ottawa) for access to their archived samples and the NRCan GEM II Program for financial support. I thank Jim Ryan (Geological Survey of Canada) for his discussions about the regional geology, Rebecca Flowers and James Metcalfe (University of Colorado – Boulder) for their assistance with (U-Th)/He dating, Nancy Joyce and Dawn Kellett (Geological Survey of Canada) for their insight and discussion regarding the regional geology, and to the thermochronology research group (University of Ottawa) for their thoughtful discussion and assistance with numerical modelling. Thanks to the Faculty of Graduate and Postdoctoral Studies and the Department of Earth and Environmental Science at the University of Ottawa.

Table of Contents

(U-Th)/He thermochronology of the Aishihik batholith, central Yukon: Evidence for stable crust in the Cretaceous

Abstract

The 190-180 Ma Aishihik batholith is the largest within the main belt of late Jurassic plutons in the northern Canadian Cordillera, and is thought to stitch assemblages of the Yukon-Tanana terrane with the Stikine terrane. Assessing the thermal history via zircon (ZHe) and apatite (AHe) (U-Th)/He thermochronology of samples from the Aishihik batholith against those of Paleozoic to Mesozoic host rocks can provide insight into the low-temperature (<200°C) window of Jurassic-Cretaceous tectonism and crustal exhumation. We analyzed sixteen plutonic samples that possess a single population of zircon and apatite grains (demonstrated by typical igneous zoning and lacking metamorphic overgrowths). Samples are grouped into three categories based on geographic location and rock type, and each set illustrates a differing thermal history. Within the first group (AHe ages: 48.5 ± 4.9 Ma to 123.6 ± 9.4 Ma; ZHe ages: 57.3 ± 5.4 Ma to 188.8 ± 13.4 Ma), numerical modeling of the data in the southeast portion of the study area, within the Aishihik batholith, suggests relatively rapid (~15°C/m.y.) cooling immediately after emplacement of the batholith. The batholith cooled by the Campanian, coinciding with the Carmacks unconformity (ca. 73-68 Ma), however some data suggests that the centre of the batholith cooled earlier (Albian), which overlaps with the Mount Nansen unconformity (ca. 110-90 Ma). The second group in the central area of the study region (AHe ages: 32.7 ± 2.8 Ma to 178.44 ± 12.4 Ma; ZHe ages: 118.3 ± 8.3 to 309.5 ± 21.5 Ma) exhibits steady cooling (~5°C/m.y.) until it reaches the surface in the Campanian. The third group in the northwest (AHe ages: 31.9 ± 5.0 Ma to 84.9 ± 6.2 Ma; ZHe ages: 29.8 ± 5.9 Ma to 90.3 ± 24.0 Ma) records moderate (~10-6°C/m.y.) cooling until surface temperatures are met in the Campanian. This research adds to the network of thermochronologic data in exploring Cretaceous crustal exhumation and tectonism of the Yukon Cordillera compared to the Alaskan and British Columbia Cordillera, which recorded Eocene

exhumation signatures. Increased understanding of low-temperature tectonothermal history can allow for better understanding of shallow crustal processes and their relationships to adjacent metal-bearing regions.

1. Introduction

During the Late Permian through the Cenozoic, terranes were episodically accreted onto the western margin of Laurentia (Monger et al., 1972; Gehrels et al., 2009). Synchronously, voluminous batholiths have intruded the North America Cordillera and are thought to have been derived from eastward-dipping subduction under the growing orogenic wedge (e.g. Berman et al., 2007; Nelson et al., 2013; Mortensen, 1992). Although sometimes appearing monotonous, batholiths are structures with complex histories and compositions, commonly an aggregation of plutonic bodies of felsic to intermediate material that have formed during deep seated melting and deformation (Paterson and Fowler, 1993; Gehrels et al., 2009). Although much is known about the source of melting, and style and timing of emplacement, little is known about the thermal history of these important crustal components once crystallization has occurred and ascent has been arrested.

The understanding of how intrusive bodies cool has been the aim of research for several decades (e.g. Lovering, 1935; Larsen, 1945; Harrison and Clarke, 1979). Moreover, exposures of the batholiths can only be observed at the surface after erosional or tectonic unroofing has removed the overlying rock, which may be driven by processes that differentially cool and expose the large bodies (e.g. Krol and Zeitler, 1996; Ortega-Rivera, 2003). This means the igneous bodies may stay warm (>300°C) for an extended period of time after intrusion: some batholiths in the Cordillera remained deep and warm for up to 60 m.y. after crystallization, with measurably slower cooling in the center of the igneous complex (e.g. Harrison et al., 1979; Gehrels et al., 2009; Fayon et al., 2017). Not surprisingly, the cooling rates can vary depending on the emplacement depths of these intrusions, such that deeper intrusions cooled slower than shallow intrusions. Furthermore, faults

or shear zones may also exhume all or parts of a batholith such that the steady cooling history of a region maybe punctuated by a tectonic event (e.g. Adriasola et al., 2005; Knight et al., 2013).

The Yukon Tanana Terrane (YTT) collided into North America in the Early Jurassic which resulted in widespread magmatism. The Aishihik batholith (ca. 190-180 Ma) is the largest within the main belt of Late Jurassic plutons in the northern Cordillera, and is thought to stitch assemblages of the YTT with those of the Stikine Terrane. In addition, there are two important regional unconformable contacts with the batholith that are somewhat equivocal due to the paucity of outcrop: the ca. 110-90 Ma Mount Nansen and the ca. 73-68 Ma Carmacks volcanic assemblages. The timing of cooling of this batholith can provide a framework for the growth of North America and offers a record of crustal stabilization through time.

To better understand the low temperature cooling and tectonic evolution of the region, a portion of the YTT in south central Yukon Territory was investigated (**Figure 1**). This study assesses the thermal history the Aishihik batholith and Paleozoic to Mesozoic host rocks to provide insight into the low temperature (<200°C) window of Jurassic-Cretaceous tectonism and crustal exhumation. To resolve the low temperature tectonothermal history of the region, zircon (ZHe) and apatite (AHe) (U-Th)/He thermochronology was applied. These new data will add to the network of thermochronologic data in exploring the Cretaceous history of the Yukon portion of the Canadian Cordillera that appears to have a different history compared to the Alaskan and British Columbian segments of the Cordilleran, which record a dominant Eocene exhumation signature. Refining the exhumation and cooling patterns of the Aishihik batholith will help resolve the low temperature thermal history witnessed in this region. In particular, we are interested in the northwest margin of the batholith that has been purported to be a tectonic contact (Johnston, 1993; Johnston and Ermder, 1995), which would be reflected in marked cooling age differential across

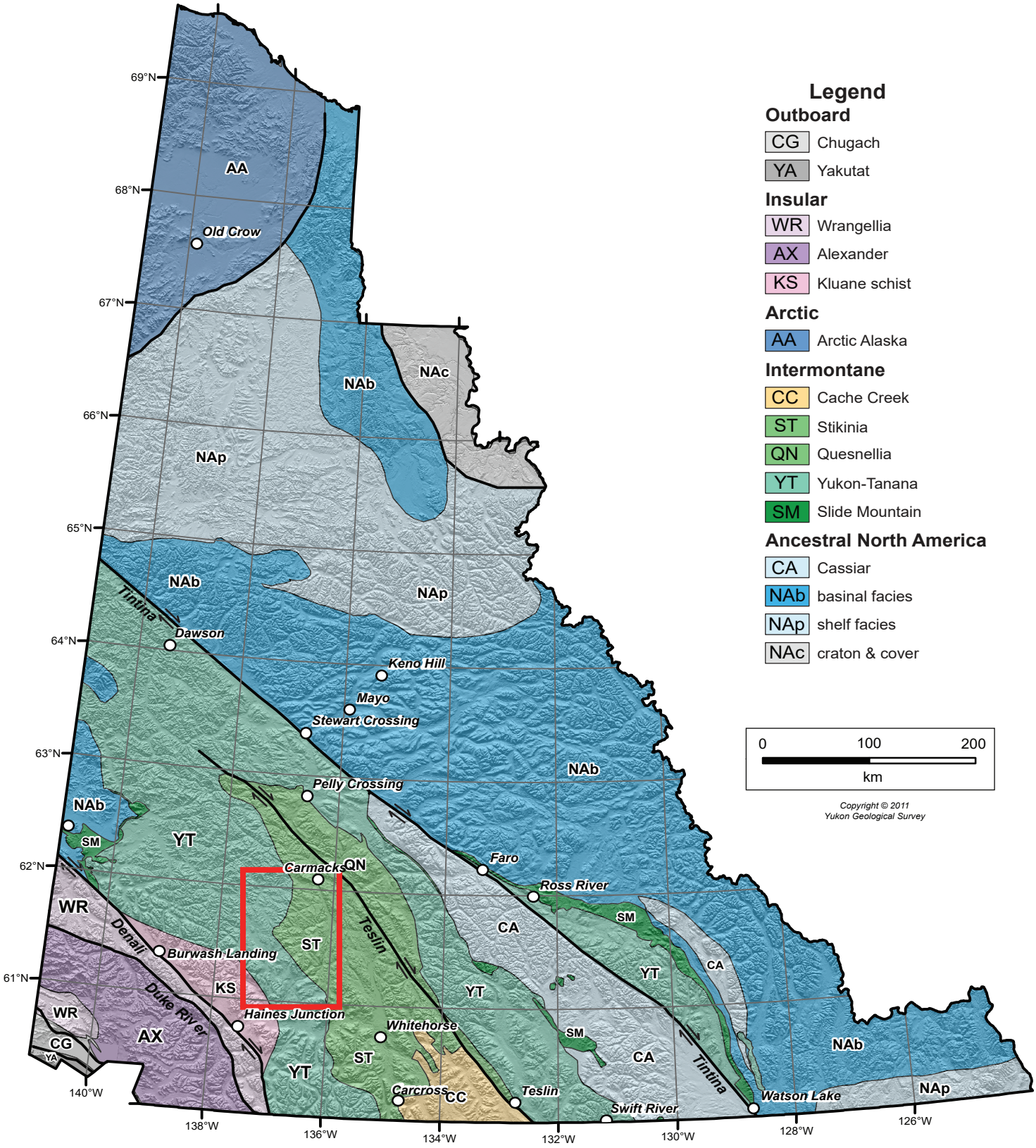

Figure 1: Terrane map of the Yukon Cordillera after Colpron and Nelson (2011). Red box denotes the location of figure 2. Terrane boundaries are represented by a thin black line and major post-accretionary faults are represented by a bold black line. Abbreviations for terrane names can be found in the legend.

the structural discontinuity. Increased recognition and understanding of the low-temperature tectonothermal history can allow for better understanding of tectonic relationships and shallow crustal processes in regions with minimal exposure.

2. Yukon Cordillera

2.1. Regional geological setting

YTT was one of the several parautochthonous and allochthonous terranes accreted onto North America during the Phanerozoic. It consists of various arc, back arc and continental margin lithotypes that are grouped into four assemblages (Mortensen, 1992; Colpron et al., 2006; Colpron et al., 2007; Nelson et al., 2006): 1) The Devonian Snowcap Assemblage is derived from the continental margin sediments and is the basement of YTT. An abundance of detrital zircons from Proterozoic or older basement rocks are characteristic to the Snowcap, along with a paucity of Silurian or younger detrital zircons (Piercey and Colpron, 2005; Nelson and Gehrels, 2007). It is comprised of polydeformed siliciclastic rock that has been metamorphosed under greenschist to amphibolite facies conditions (ca. 245 Ma, ca. 197-188 Ma; Morneau, 2017). 2) Devono-Mississippian Finlayson Assemblage is derived from an arc to back arc environment and is composed of metavolcanic and metasedimentary rock. 3) Mississippian-Permian Klinit Assemblage originated from an island arc as a combination of carbonate sedimentary units and intermediate to mafic volcanic rocks. 4) The mid-late Permian Klondike Assemblage is mostly felsic volcanic rocks.

The Phanerozoic evolution of the western margin of North America involved a long history of plate convergence, magmatism and terrane accretion that resulted in the development of an accretionary Cordilleran orogen (Monger et al., 1972). Arc activity in the middle Paleozoic caused

the opening of the Slide Mountain back arc basin behind an east-dipping subduction zone (Murphy et al., 2006; Colpron et al., 2006). The rifting that created the Slide Mountain Ocean occurred in the Late Devonian and is responsible for both the ca. 365-357 Ma Finlayson and ca. 357-342 Ma Wolverine magmatic cycles, ultimately forming the ca. 365-345 Ma Finlayson Assemblage. Subduction began in the Devono-Mississippian, generating the ca. 390-365 Ma Ecstall magmatic cycle, which is regionally defined as the ca. 365-360 Ma Simpson Range plutonic suite that intrudes both the Snowcap and the Finlayson assemblages. Finlayson, Wolverine, Little Salmon (ca. 342-314 Ma) and Klinkit (ca. 314-269 Ma) magmatic cycles are associated with Slide Mountain rifting (Nelson et al., 2006; Colpron et al., 2007). The end of the early Permian is marked by a cessation of magmatism and sedimentation, until widespread ca. 269-253 Ma Klondike magmatic cycle began that resulted in the formation of Sulphur Creek Suite.

Subduction flip, likely caused by plate collision, is purported to have occurred during the middle Permian allowing for the closure of Slide Mountain Ocean by Late Triassic (Nelson et al., 2006; Berman et al., 2007). The consumption of Slide Mountain Ocean permitted the accretion of YTT to ancestral North America. Subduction flipped again, to the east, and began consuming the Panthalassa Ocean. During the Late Triassic to Early Jurassic widespread magmatism resulted in the Long Lake Suite which comprises the ca. 190-180 Ma Aishihik batholith (Knight et al., 2013).

Three major deformation events have occurred in the YTT. The first event, evinced by S_1 pre-transposition fabrics (Johnston, 1993) and cross-cutting relationships between a late Permian pluton and ductile foliation, indicate that the Aishihik region was deformed prior to the Late Permian. An S_2 fabric is observed through aligned micas in pelitic rocks, transposed structures and lithological boundaries and leucocratic lenses within magmatic zones near the border of the Aishihik batholith (Clark, 2017). The D_2 event occurred in the Early Jurassic prior to the intrusion

of the Aishihik batholith, at a time when Johnston's (1993) proposed that thrusting along the batholith margin was active. D_3 can be observed through east verging F_3 folds, but it requires more detailed observations and analysis to further constrain the timing of the event (Clark, 2017).

Regionally, crystalline bedrock was residing in the middle crust (300-500°C) between ca. 200-175 Ma (Knight et al., 2013; Joyce et al., 2015; Staples et al., 2016; Clark, 2017). Within our study area, the $^{40}Ar/^{39}Ar$ biotite cooling age is 187.0 ± 1.3 Ma and hornblende is 186.0 ± 1.3 Ma (Joyce et al., 2015), which were obtained from the the Simpson Range plutonic suite, and will be used in our numerical modeling. The Mount Nansen volcanic sequence was formed by a pulse of magmatism between ca. 110-90 Ma creating an unconformity with the underlying material. In the Late Cretaceous (ca. 73-68 Ma), magmatism formed the Carmacks volcanic unit, which also created a second unconformity. Both unconformities were determined based on the age of volcanic rock directly residing on crystalline basement. These unconformities are important independent geologic constraints as they occurred during the Cretaceous, the period of time that is the focus of this investigation. The magmatism is thought to have produced hydrothermal fluids that circulated along brittle faults and fractures causing polymetallic deposits across southcentral Yukon (Knight et al., 2013; Joyce, 2002).

The landscape evolution of an orogen plays an important role in focussing strain, and source-to-sink relationships in the adjacent basins (cf. Koons et al., 2013). Within the Yukon Cordillera, the age of the topography has been somewhat equivocal, ranging from Early Cretaceous to Miocene (Tempelman-Kluit, 1980; Staples et al. 2016). Using geophysical and hydrological modelling, Ryan et al. (2017) evaluated the impact of Tintina fault displacement on the development of the Yukon River. Results indicate that there has been little net incision of the region since the Mesozoic (i.e. the last 100 m.y.), which allowed for the widespread preservation

of middle Cretaceous to Paleocene units. Consequently, the Mount Nansen and Carmacks unconformities resided at a similar elevation as the present-day erosional surface, making a case that this portion of the Cordillera exhibits a mature landscape.

2.2. Geology of the Aishihik batholith area

The Aishihik region (**Figure 2**) was originally assigned to the Yukon Group by Tempelman-Kluit (1974) and was then interpreted to be composed of Nisling and Nasina assemblages (Johnston et al., 1996; Mortensen, 1992). In 2006, Colpron et al. re-interpreted it for a second time, now belonging to the Devonian Snowcap and Devono-Mississippian Finlayson assemblages. Tectonized amphibolite-facies rocks in the Aishihik region record the burial of YTT to mid-crust conditions during the earliest Jurassic (D_2). Prograde metamorphism coeval with intense development of D_2 foliation increased from ~5 kbar and 500-550°C to ~7 kbar and 640-650°C prior to the intrusion of the Aishihik batholith (Clark, 2017). It is probable that since the batholith intruded relatively cool rocks (Knight et al., 2013; Joyce et al., 2016; Clark, 2017), emplacement generated a locally elevated geothermal gradient evinced by the appearance of high-grade index minerals within 5-10 km of the batholith's margins (Clark, 2017).

The 190-180 Ma (Joyce et al., 2016) Aishihik batholith intrudes Stikinia strata and YTT in south central Yukon. The Aishihik batholith is the largest of the Late Triassic-Early Jurassic plutons and extends from Whitehorse to Carmacks, YT. The batholith is one large, east-dipping, lopolith-shaped body that tapers to the west (Johnston and Erdmer, 1995). In the center of the batholith, the Long Lake Suite is typified by a coarse grained monzogranite to granodiorite with varying amounts of biotite and hornblende. Large (~2-6 cm) potassium feldspar crystals and 0.5-1 cm scale smokey quartz are a defining characteristic, with euhedral crystals not uncommon. The rock lacks a definitive planar or linear structure except for a sub-horizontal preferential weathering

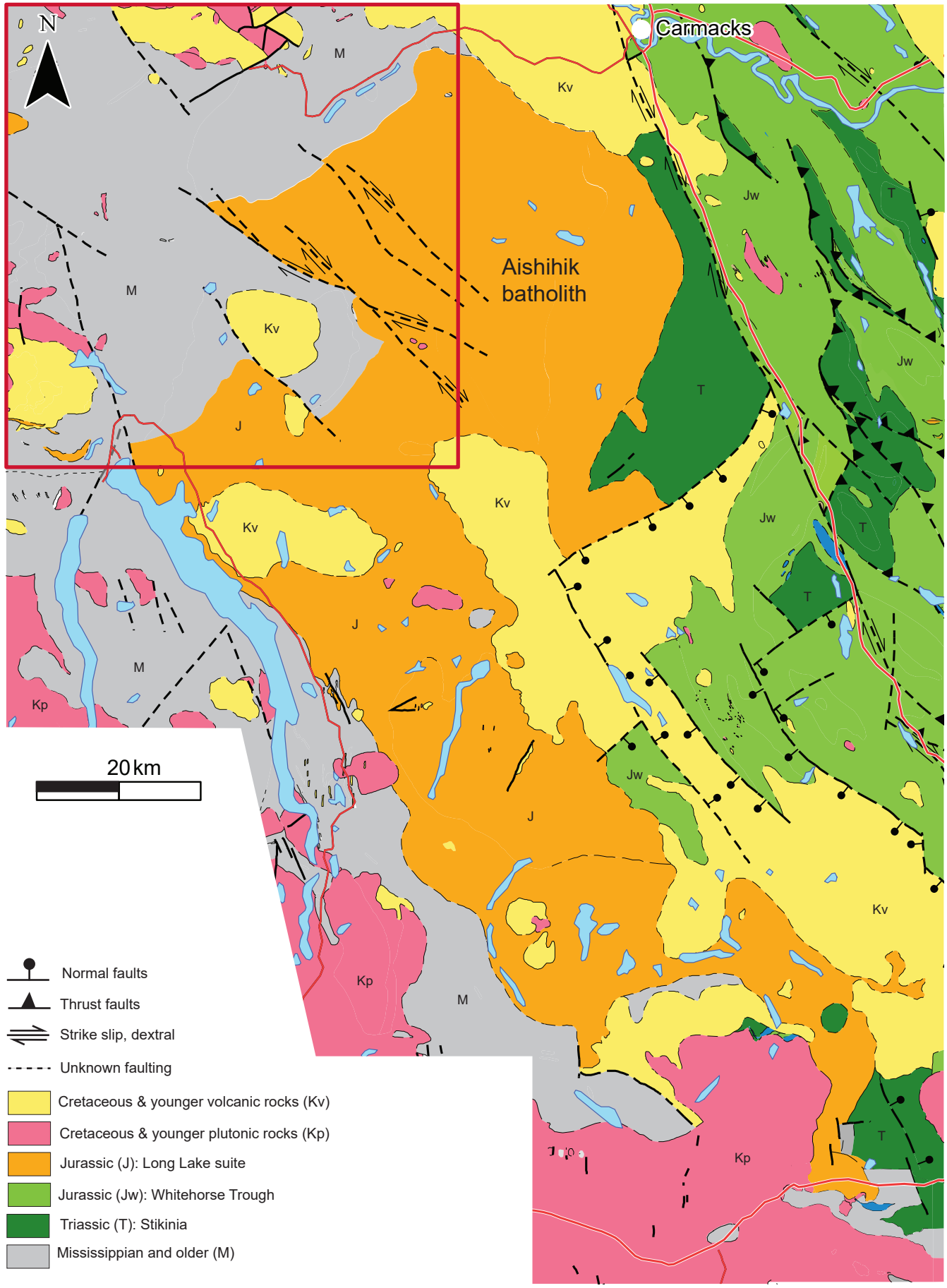

Figure 2: Geological map of the area surrounding the Aishihik batholith. Geology is coloured by terrane affinity. Red box denotes the location of figure 4. Map modified from Joyce et al. (2016).

pattern. Closer to the batholith margins, the large potassium feldspar crystals are absent, as the rock becomes dioritic in composition. Mafic phases (biotite, hornblende) increase in proportion and the rock takes on a weak to moderate foliation. The range of granitic lithologies and compositions throughout the batholith show gradational contacts. Two generations of dikes up to 30 cm wide also intrude the pluton. The first generation is a fine to medium grained granodioritic dike set that cross-cuts the suite. The second generation of dikes are aplites that cross cut both the first generation of dikes and the suite itself. These dikes appear to be common in, but not limited to, the northern part of the batholith (Joyce et al., 2016). The two generation of dikes have yet to be dated.

The Aishihik batholith was originally proposed to have intruded to mid-crustal depths (~30 km) based on the occurrence of a kyanite-bearing metamorphic aureole, metamorphic titanite located adjacent to the batholith and magmatic epidote (Johnston and Erdmer, 1995). However, Topham et al. (2015) reports Al-in-hornblende barometry for the batholith that yielded shallower conditions of 12-15 km (3-4 kbar). Previous thermochronology studies suggests that it began to immediately cool after emplacement: biotite and hornblende K-Ar ages from the batholith record 166-164 Ma cooling ages (Tempelman-Kluit and Wanless, 1975), and K-Ar and $^{40}Ar/^{39}Ar$ data indicate regional cooling in the Early Jurassic (Knight et al., 2013; Joyce et al., 2015; Clark, 2017).

In this study, we examine the thermal history of the Aishihik batholith region to assist in our understanding of the Cretaceous exhumation and tectonism in the Yukon Cordillera. Both apatite and zircon were analyzed using (U-Th)/He thermochronology to obtain cooling ages in the Aishihik batholith and within the host rock. This study examines age-temperature relationship, where time-temperature models show discrete cooling episodes, rates and changes in rates with

respect to the magmatic or tectonic evolution. The results give insight to into a low-temperature window to help better understand the Cordillera crust during the Cretaceous.

3. (U-Th)/He thermochronology

3.1 Introduction

Thermochronology assesses the thermal evolution of a sample or a region by dating the thermal events recorded in minerals or rocks. Commonly, thermochronology is used to specifically focus on the part of the pressure-temperature path that reveals the cooling and exhumation of an area. Despite the fact that the decay of uranium and thorium to produce helium has been known and recognized for a century (Rutherford, 1905), (U-Th)/He dating is still a relatively new technique. Preliminary studies showed that (U-Th)/He analysis yielded excessively young dates (Hurley, 1954) that were credited to the loss of helium, suggesting that helium ages only offer a minimum approximation to the time elapsed since their formation (Reiners, 2002). It was not until later that Zeitler et al. (1987) proposed that (U-Th)/He ages could be interpreted as cooling through low temperatures.

(U-Th)/He analysis provides a powerful tool for investigating upper crustal or near surface tectonic problems as it allows for a detailed examination of a narrow thermal window that corresponds to the brittle behavior of rocks. For example, the traditional approach in assessing the timing, duration, and rate of crustal extension, dates of intrusive rocks or stratigraphic units are used to constrain the timing of offset during extension. Those approaches, however, are not reliable if the area lacks obvious cross-cutting relationships or piercing points across the fault. Using low temperature thermochronology, one is able to date the cooling (i.e. exhumation) of footwall rocks of low-angle normal faults during extension, where the footwall will cool later relative to the

hanging wall, allowing for the timing of extensional exhumation to be resolved. The cooling age would then represent the timing of slip along the fault (Stockli, 2005). The duration and rate of unroofing can also be determined in areas of crustal thickening and mountain building, which is typically accomplished through vertical relief age-elevation relationships. Theoretically, the samples collected near the top of the section would have older cooling ages, as these rocks would have reached surface temperatures first relative to the samples collected near the base. Relief transects are useful to be able to determine the rate of exhumation within mountain belts, yet age-elevation transects may not be possible in ancient orogens due to their low relief (Spotila, 2005). Cooling through tectonic exhumation is typically measured when there is a positive relationship between elevation and He age, while cooling through erosion is generally recorded when there is a negative correlation between elevation and He age (Braun, 2002).

(U-Th)/He thermochronology is based on the retention of ^{4}He that is produced from α-decay of ^{238}U, ^{235}U, ^{232}Th and ^{147}Sm (Reiners, 2002; Harrison and Zeitler, 2005). A cooling date is the time when a mineral passes through a specific closure temperature (or blocking temperature) to diffuse the daughter product (Dodson, 1973). Different minerals have different closure temperatures in different systems, and this study focuses on the low temperature thermochronometers that document processes in the shallow crust. Zircon and apatite are two minerals commonly used in thermochronologic studies due to their low closure temperatures (T_c) (210°C and less), which are dependent upon, among other things, the cooling rate through the partial retention zone (PRZ), effective uranium concentration (eU), and grain size. The PRZ is the temperature range between a fully open and a fully closed diffusion system; in zircon, the PRZ is 130-210°C (Reiners et al., 2004; Stockli, 2005; Reiners and Brandon 2006; Wolfe and Stockli, 2010; Guenthner et al., 2013) and in apatite 30-90°C (Flowers et al., 2009). Above these

temperatures, helium diffuses openly out of a grain, the grain will be annealed and the He clock resets. Below these temperatures the grain is considered a closed system. The finite T_c of zircon (~180°C) and apatite (~70°C) can only be invoked if a rock has rapidly cooled and does not have a long residence time (millions of years) in the partial retention zone. Effective uranium concentration (eU = [U] + 0.235 • [Th]) can be used as a proxy for the amount of radiation damage a crystal has accumulated, and modelling software integrates eU with time spent below the annealing temperature to predict diffusivity. With elevated temperatures, that is within the PRZ, ^{4}He diffuses from an undamaged crystal preferentially along the c-axis (**Figure 3**, panel A). Radiation damage deforms the crystal lattice, creating a tortuous diffusion pathway, resulting in zircon crystals that are increasingly retentive of ^{4}He (**Figure 3**, panel B). However, once a threshold is reached, imperfections in the crystal lattice connect, forming fast diffusion pathways for ^{4}He to more quickly diffused from the crystal (**Figure 3**, panel C). With apatite, there is a predicted positive correlation between AHe date and eU values (Flowers et al., 2009). A similar positive trend is observed in zircon, except as radiation damage increases the relationship reverses and young ages are indicative from high eU grains (**Figure 3**; Guenther et al., 2013, 2014). The inflection, or roll over point, commonly occurs at an eU of 200-250 ppm. The positive correlation between ZHe and eU is thought to represent the effects of increasing radiation damage on helium diffusion at low α-doses (degree of damage), whereas a negative date-eU correlation illustrate zircons with high α-doses. Finally, grain size can control helium diffusivity, due to larger grains retaining more ^{4}He which then exhibit older cooling ages (Dodson, 1973). Grain specific parameters that can affect He diffusion kinetics, which can result in some age dispersion, include the cooling rate through the PRZ, grain size and the integrated accumulation of radiation damage within the crystal lattice.

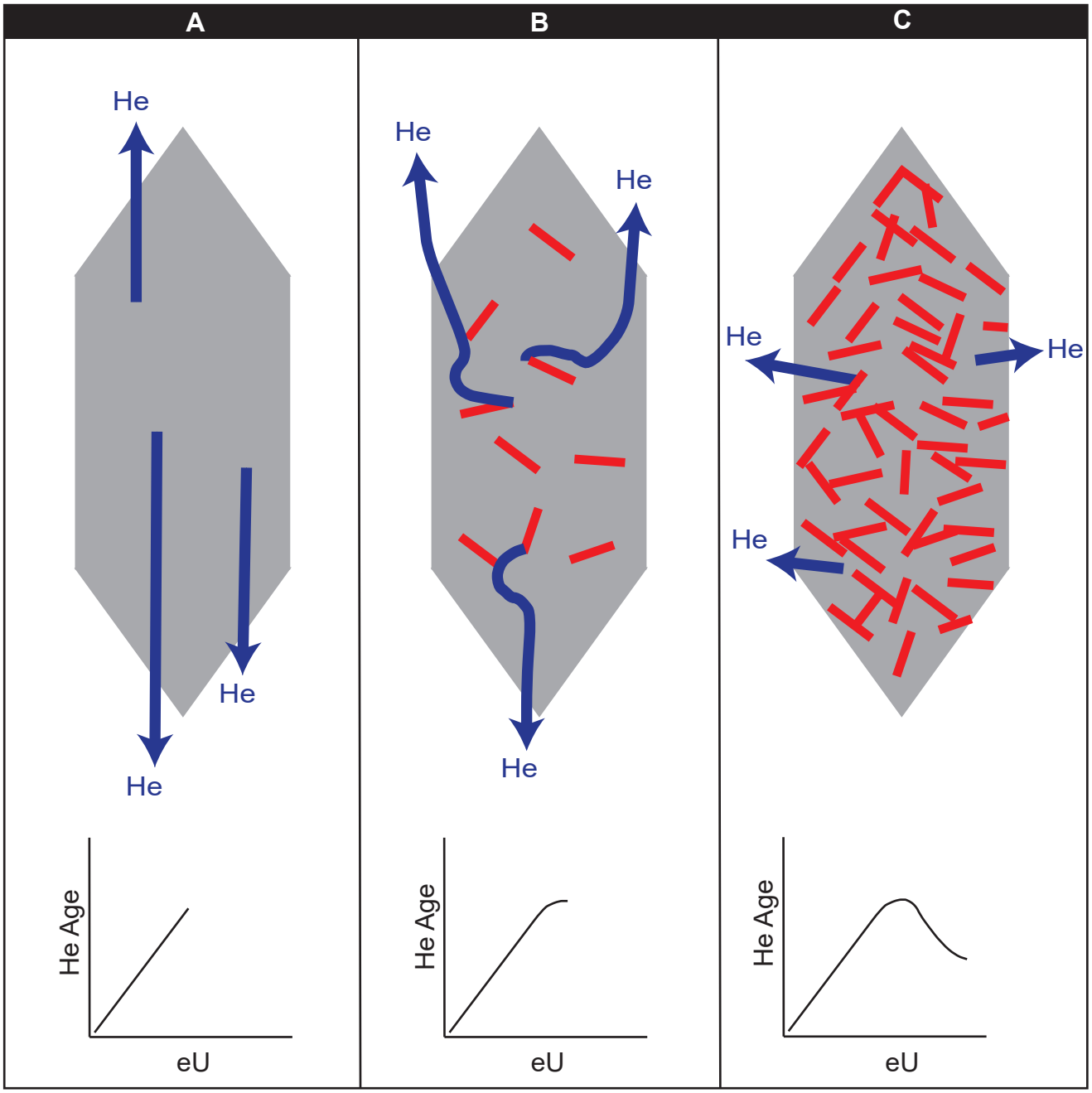

Figure 3: Schematic of He diffusion out of a zircon crystal. In Panel A, He diffuses openly out of a zircon crystal preferentially along the c-axis at temperatures above 210°C. The relationship between He age and eU that is recorded has a positive correlation. In Panel B, the zircon crystal begins to accumulate radiation damage as it goes through the PRZ. Traps/holes (red lines) form in the zircon's crystal lattice allowing for He to be retained within the crystal for longer periods of time. The relationship between He age and eU at this stage records an inflection point within the data. In Panel C, the zircon crystal has accumulated even more radiation damage and the trap/holes line up to create pathways for He to diffuse out the sides of the crystal. The relationship between He age and eU shows a negative correlation. Schematic modified from Chew and Spikings (2015).

3.2. Analytical approach and methods

Detailed mapping and sampling traverses were conducted within the Aishihik batholith region 1) to investigate the model of Johnston (1993) regarding the thrust contact nature of the northwestern margin of the Aishihik batholith and 2) to better understand the overall low-temperature history of the batholith relative to the YTT. The Aishihik batholith was chosen for this study because of its assumed simple cooling history, it is largely undeformed and its spatial relationship to mineral endowments. Rocks were sampled on both sides of known and proposed structural discontinuities to assess their significance and potential reactivation in the low-temperature (<200°C) realm. We predict that if there is any vertical displacement then samples collected on either sides of the fault should exhibit different cooling ages. The batholith was sampled from the margin to the interior to allow for a complete thermal history to be obtained. Rocks from the batholith were predicted to have simple cooling histories because of the single population of igneous grains (optically defined) that were selected, which should all possess similar crystallization ages and no inherited thermal histories. It is also predicted that the samples collected near the margin will have an older cooling age then the interior, as we predict that the edges would have cooled before the interior. The basement rocks of the YTT is the Snowcap Assemblage that is derived from continental margin sediments. These rocks host detrital grains that would be expected to have multiple populations of grains that may have been subjected to a variety of thermal histories (Piercey and Colpron, 2005; Nelson and Gehrels, 2007).

Sixteen samples from the Aishihik batholith and surrounding YTT were selected for (U-Th)/He thermochronology, yielding 79 zircon grains and 49 apatite grains (**Figure 4; Table 1**). To facilitate a systematic and simplified data analysis, three regions were defined to help resolve the low temperature thermal history of the study area: Northwestern, Central and Southeastern

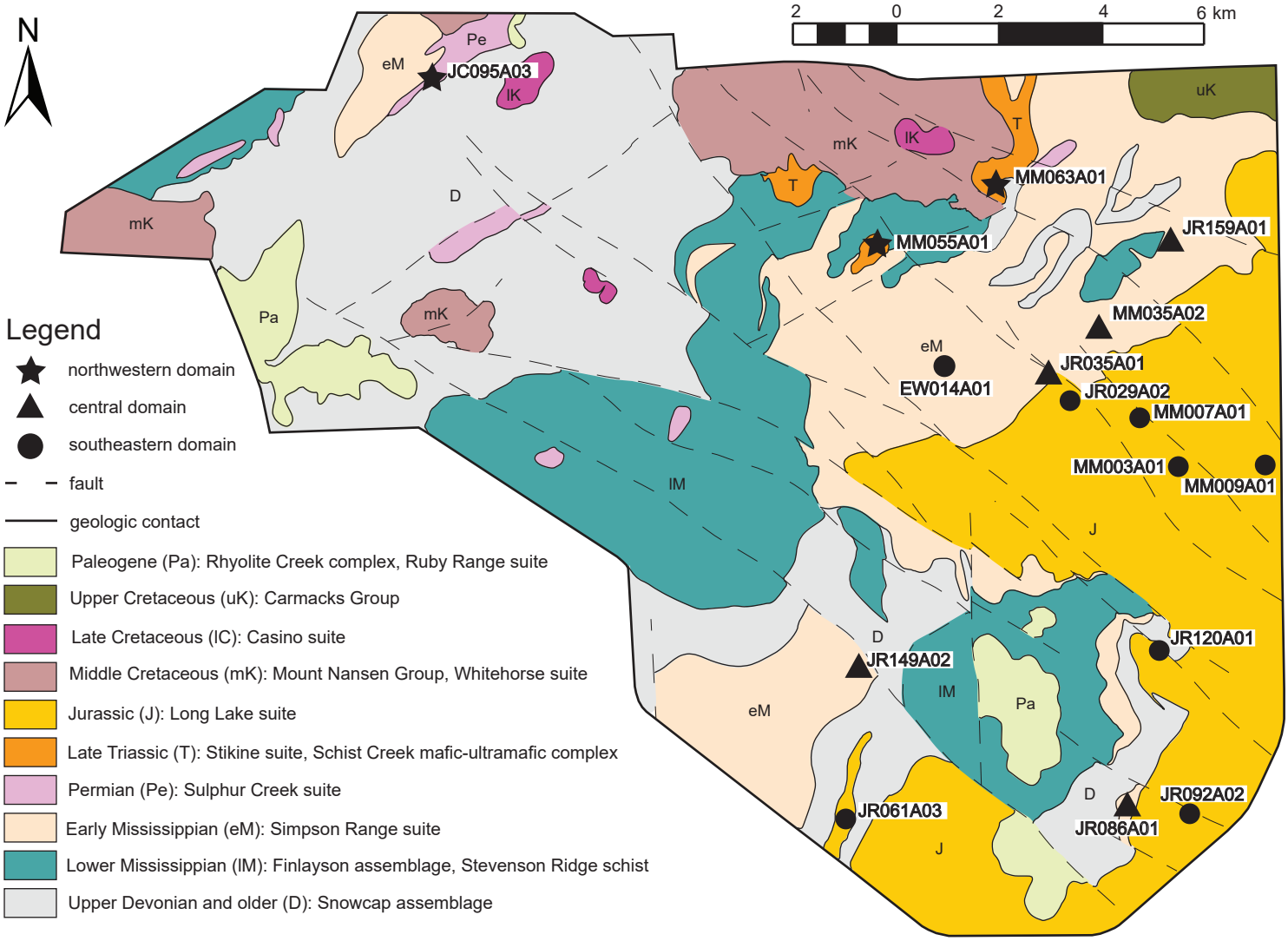

Figure 4: Simplified bedrock map of the Mount Nansen-Nisling River area, and sample locations within the Aishihik batholith and surrounding host rock. Lithological units have been grouped together based on crystallization age and samples have been divided into three domains based on geographic location and rock crystallization age. The region is underlain by dominantly Paleozoic rocks of YTT and overlain by Triassic to Paleogene rocks. Northwestern domain (stars) includes Sulphur Creek suite and Stikine suite rocks. Central domain (triangles) contains rocks from the Simpson Range plutonic suite. Southeastern domain (circles) contains rocks from the Long Lake suite. All sample points begin with 15RAY- and are then followed by their character sample name. Map modified from Ryan et al. (2016).

Table 1a. (U-Th)/ He single grain analyses of zircon and apatite from the northwestern domain

grain	mineral	corrected age (Ma)	±	raw age (Ma)	±	4He (nmol/g)	±	U (ppm)	±	Th (ppm)	±	Sm (ppm)	±	eU	Ft	.rs (µm)
15RAY-JC095A03 *(62.128N, 137.785W) 1341m Permian, Sulphur Creek, granodiorite*																
A01*	apatite	259.34	32.41	203.40	20.87	0.47	0.00	0.01	0.04	1.76	0.02	0.03	0.09	0.4	0.78	73.83
A02	apatite	38.34	5.42	23.49	2.92	0.31	0.01	0.00	0.00	10.38	0.25	0.31	0.58	2.4	0.61	39.75
A03	apatite	84.92	6.20	64.18	1.40	4.33	0.01	7.38	0.26	20.63	0.41	22.31	1.02	12.2	0.75	58.64
A04	apatite	31.88	4.97	19.86	2.30	0.27	0.01	0.12	0.28	10.22	0.18	0.00	0.00	2.5	0.62	41.55
A05	apatite	67.48	4.97	50.15	1.04	5.50	0.08	11.39	0.29	36.32	0.59	50.53	2.04	19.9	0.74	56.36
Z01	zircon	61.41	4.35	49.53	0.37	436.19	0.28	1453.39	12.50	737.55	7.08	5.28	2.34	1626.7	0.81	58.82
Z02	zircon	60.31	4.29	54.31	0.56	622.06	0.65	1922.38	21.65	818.19	26.44	8.35	0.74	2114.7	0.90	116.84
Z03	zircon	55.82	4.02	49.73	0.75	612.36	1.62	2099.10	35.01	746.92	8.40	12.71	1.48	2274.6	0.89	105.93
Z04	zircon	59.46	4.16	49.25	0.43	392.53	0.39	1354.90	13.24	500.39	5.15	2.44	1.06	1472.5	0.83	65.92
Z05	zircon	57.83	4.16	50.62	0.79	408.68	0.38	1362.24	23.99	548.49	7.06	21.20	2.75	1491.1	0.87	92.41
15RAY-MM063A01 *(62.061N, 137.099W) 1290m Late Triassic, Stikine Suite, granodiorite*																
A01	apatite	46.71	5.23	29.15	1.11	1.56	0.02	8.79	0.35	4.59	0.15	7.16	0.98	9.9	0.62	36.30
A02	apatite	58.76	9.31	34.60	1.06	3.16	0.03	13.02	0.49	16.05	0.51	9.05	1.35	16.8	0.59	33.70
A03	apatite	56.93	6.61	35.76	0.57	5.22	0.02	18.74	0.37	34.67	0.94	9.35	0.86	26.9	0.63	38.54
Z01	zircon	85.13	7.12	66.20	0.81	131.89	0.17	329.52	4.61	161.36	2.14	2.77	6.98	367.4	0.78	50.29
Z02	zircon	78.08	9.80	59.21	0.63	126.26	0.07	367.64	4.29	110.39	1.44	3.06	6.70	393.6	0.76	46.18
Z03	zircon	90.32	24.04	60.69	0.47	206.79	0.23	552.22	4.90	325.04	2.56	6.40	19.04	628.6	0.67	33.57
Z04	zircon	80.49	18.85	55.77	0.42	106.21	0.12	321.60	2.69	127.64	1.78	0.00	0.00	351.6	0.69	35.86
Z05	zircon	73.02	7.44	56.74	0.52	112.03	0.10	343.12	3.42	91.23	1.60	0.63	1.67	364.6	0.78	50.23
15RAY-MM055A01 *(62.032N, 137.256W) 1313m Late Triassic, Stikine Suite, granite*																
Z01	zircon	45.82	3.50	39.96	1.31	0.47	0.00	2.10	0.07	0.25	0.00	0.87	0.27	2.2	0.87	88.86
Z02	zircon	29.81	5.91	21.29	1.82	0.55	0.01	4.78	0.40	0.00	0.00	3.76	9.33	4.8	0.70	37.65
Z03*	zircon	492.73	97.82	366.54	69.76	1.27	0.02	0.44	0.12	0.80	0.02	0.00	0.00	0.6	0.74	43.91

* Grain not used in (U-Th)/He models

Table 1b. (U-Th)/ He single grain analyses of zircon and apatite from the central domain

grain	mineral	corrected age (Ma)	±	raw age (Ma)	±	4He (nmol/g)	±	U (ppm)	±	Th (ppm)	±	Sm (ppm)	±	eU	Ft	.rs (µm)
15RAY-JR035A01 *(61.954N, 137.029W) 1273m Mississippian, Simpson Range suite, granodiorite*																
Z01	zircon	309.52	21.50	248.26	1.47	50.76	0.07	13.69	0.16	99.97	0.63	6.79	0.86	37.2	0.80	61.33
Z02	zircon	252.38	17.24	196.80	1.96	82.62	0.08	41.35	0.41	149.69	2.74	11.63	0.90	76.5	0.78	53.24
Z03	zircon	198.03	13.68	163.22	1.74	97.69	0.10	74.01	1.16	150.48	1.28	11.37	0.48	109.4	0.82	66.37
Z04*	zircon	871.22	67.71	545.27	5.32	119.32	0.45	4.27	0.22	150.04	1.21	0.00	0.00	39.5	0.62	33.20
Z05*	zircon	367.33	25.61	297.16	2.52	76.22	0.08	22.47	0.30	102.23	1.13	5.70	0.67	46.5	0.81	62.15
15RAY-JR086A01 *(61.699N, 136.944W) 1407m Mississippian, Simpson Range suite, granodiorite*																
A01	apatite	76.53	5.46	53.90	1.08	4.37	0.02	14.68	0.30	0.97	0.06	10.98	0.60	14.9	0.70	45.17
A02	apatite	32.66	2.83	25.35	1.24	0.35	0.00	2.31	0.12	0.76	0.03	9.32	0.39	2.5	0.77	62.27
A03	apatite	80.79	13.51	52.93	8.24	0.21	0.01	0.43	0.11	1.29	0.10	0.09	0.51	0.7	0.65	42.86
A04	apatite	53.34	14.08	33.08	8.20	0.10	0.02	0.46	0.10	0.32	0.06	0.00	0.00	0.5	0.62	36.42
15RAY-J159A01 *(62.032N, -136.891W) 1247m Mississippian, Simpson Range suite, granodiorite*																
A01*	apatite	256.01	124.82	179.77	92.14	0.27	0.01	0.00	0.00	1.19	0.01	0.00	0.00	0.3	0.72	52.79
A02	apatite	45.75	3.42	37.06	0.92	0.89	0.00	4.08	0.11	1.43	0.05	5.44	0.18	4.4	0.81	72.86
A03	apatite	62.08	6.15	41.26	1.28	2.93	0.01	11.28	0.41	7.39	0.18	11.32	1.11	13.0	0.66	41.50
A04	apatite	78.71	7.56	49.79	2.49	2.40	0.02	8.12	0.46	3.03	0.03	9.63	1.06	8.8	0.63	36.47
A05	apatite	50.60	4.25	34.14	1.87	1.13	0.01	5.74	0.34	1.27	0.01	8.86	0.58	6.0	0.67	41.15
Z01	zircon	118.31	8.31	103.52	1.15	347.83	0.39	580.84	7.06	157.14	1.16	4.10	0.58	617.8	0.87	91.22
Z02	zircon	131.31	9.32	108.26	0.97	413.22	0.28	655.53	6.48	195.50	1.70	3.51	0.84	701.5	0.82	64.34
Z03	zircon	153.36	18.18	117.42	1.08	595.44	0.70	863.65	8.72	287.01	3.11	11.08	12.70	931.1	0.76	47.53
Z04	zircon	141.11	10.08	115.35	1.26	663.59	0.57	993.20	11.83	269.93	2.35	3.98	0.62	1056.6	0.82	61.64
Z05	zircon	153.45	11.05	124.59	2.01	322.29	0.33	440.43	7.90	145.90	1.50	0.00	0.00	474.7	0.81	59.80
15RAY-MM035A02 *(61.980N, 136.977W) 1177m Mississippian, Simpson Range suite, granite*																
A01	apatite	178.44	12.38	128.93	1.79	21.33	0.02	25.39	0.42	20.55	0.50	15.13	0.55	30.2	0.72	50.03
A02	apatite	68.02	6.69	47.05	1.38	1.83	0.01	6.53	0.21	2.75	0.04	2.98	0.68	7.2	0.69	44.93
A03	apatite	81.13	11.45	47.45	1.38	11.85	0.05	36.33	1.37	40.79	0.25	23.90	2.53	45.9	0.58	33.22
Z01	zircon	186.21	20.92	139.19	1.55	381.47	0.43	449.91	5.73	222.74	2.03	1.52	7.25	502.3	0.74	43.99
Z02	zircon	168.10	15.16	129.54	1.15	288.66	0.29	360.54	3.71	204.88	1.34	5.13	10.50	408.7	0.77	48.53
Z03	zircon	202.15	14.31	163.50	1.86	406.88	0.20	400.51	5.34	232.24	1.49	0.88	2.63	455.1	0.81	58.83
Z04	zircon	168.21	11.85	131.05	1.44	274.20	0.21	336.46	4.31	201.01	2.78	0.00	0.00	383.7	0.78	50.86
Z05	zircon	205.49	14.03	163.10	1.98	556.60	0.47	563.46	7.76	257.95	2.69	0.00	0.00	624.1	0.79	53.82
15RAY-JR149A02 *(61.788N, 137.260W) 1133m Mississippian, Simpson Range suite, granodiorite*																
Z01	zircon	145.72	11.43	111.45	1.29	93.70	0.09	139.03	1.82	65.50	1.17	3.51	7.78	154.4	0.76	46.74
Z02	zircon	182.47	23.27	130.17	1.51	217.28	0.32	272.25	3.59	144.13	2.22	2.42	4.86	306.1	0.71	38.61
Z03	zircon	167.48	28.41	111.27	1.83	174.70	0.22	259.32	4.87	123.86	1.14	0.00	0.00	288.4	0.66	32.30
Z04*	zircon	1615.87	134.11	1246.92	43.70	41.72	0.05	5.41	0.20	0.26	0.01	0.00	0.00	5.5	0.74	42.01
Z05	zircon	156.84	17.54	116.28	2.48	95.74	0.08	131.67	3.30	82.83	1.25	6.00	19.12	151.1	0.74	43.13

* Grain not used in (U-Th)/He models

Table 1c. (U-Th)/ He single grain analyses of zircon and apatite from the southeastern domain

grain	mineral	corrected age (Ma)	±	raw age (Ma)	±	4He (nmol/g)	±	U (ppm)	±	Th (ppm)	±	Sm (ppm)	±	eU	Ft	.rs (µm)
15RAY-JR029A02 *(61.938N, 137.002W) 1185m Early Jurassic, Long Lake Suite, granodiorite*																
A01	apatite	48.48	4.89	30.79	0.90	2.48	0.02	9.46	0.42	22.41	0.43	14.89	1.20	14.7	0.63	39.41
A02	apatite	86.17	5.97	60.50	1.44	4.08	0.02	8.02	0.29	18.16	0.28	15.89	0.71	12.3	0.70	47.58
A03	apatite	112.78	7.88	86.69	1.17	8.72	0.02	12.22	0.25	26.29	0.29	13.46	0.31	18.4	0.77	62.16
A04	apatite	76.12	6.20	49.68	0.81	4.77	0.03	10.71	0.23	29.13	0.63	14.32	1.21	17.6	0.65	41.57
Z01	zircon	164.82	11.65	147.24	1.72	320.46	0.86	370.19	4.68	120.87	1.42	0.22	0.36	398.6	0.89	107.32
Z02	zircon	133.17	13.28	103.49	1.63	538.15	0.67	900.51	15.50	236.14	3.27	18.81	19.80	956.0	0.77	50.02
Z03	zircon	182.61	13.01	154.18	2.20	751.42	0.62	848.43	13.12	185.40	2.09	2.16	3.54	892.0	0.84	72.00
Z04	zircon	169.02	11.88	148.73	1.53	164.26	0.15	184.09	2.13	77.07	0.91	2.50	3.16	202.2	0.88	94.93
Z05	zircon	161.95	11.49	147.07	1.33	195.73	0.57	222.63	2.13	89.83	1.29	0.16	0.19	243.7	0.91	125.43
15RAY-JR092A02 *(61.701N, 136.860W) 1437m Early Jurassic, Long Lake Suite, granodiorite*																
A01	apatite	61.97	9.77	38.73	2.01	2.18	0.01	8.57	0.55	7.44	0.20	7.74	1.29	10.3	0.62	36.39
A02	apatite	68.38	6.52	47.77	1.37	2.34	0.01	8.14	0.26	3.71	0.11	6.41	0.59	9.0	0.70	45.72
A03	apatite	58.82	4.09	47.39	0.50	4.39	0.00	15.10	0.18	8.26	0.09	8.24	0.21	17.0	0.80	72.10
A04	apatite	52.10	3.66	40.80	0.53	3.38	0.00	13.84	0.20	5.97	0.14	9.12	0.32	15.2	0.78	64.31
Z01	zircon	179.87	32.41	125.40	1.12	220.67	0.20	286.32	2.88	155.12	2.54	13.72	27.29	322.8	0.69	36.26
Z02	zircon	164.92	11.69	146.23	1.21	216.69	0.15	247.07	2.30	103.48	1.01	0.45	0.83	271.4	0.89	101.28
Z03	zircon	181.00	12.82	151.89	1.15	225.05	0.16	244.46	2.07	113.93	1.77	1.36	2.85	271.2	0.84	70.60
Z04	zircon	171.72	21.61	130.24	1.37	137.39	0.12	176.86	2.08	70.47	1.06	7.77	6.77	193.4	0.76	46.05
Z05	zircon	187.75	13.34	162.55	1.66	186.86	0.13	193.34	2.21	71.88	0.66	0.94	2.35	210.2	0.86	84.80
15RAY-JR120A01 *(61.800N, 136.906W) 1426m Early Jurassic, Long Lake Suite, monzogranite*																
A01	apatite	68.63	4.81	48.63	0.51	7.05	0.02	18.82	0.27	33.18	0.42	17.68	0.97	26.6	0.71	48.93
A02	apatite	88.38	6.38	66.12	1.11	5.66	0.01	13.93	0.27	7.52	0.14	9.53	0.61	15.7	0.75	55.18
A03	apatite	70.15	4.98	54.51	0.57	3.76	0.01	7.15	0.12	23.06	0.25	15.96	0.57	12.6	0.77	65.76
A04	apatite	51.33	2.88	34.12	0.27	2.92	0.01	8.59	0.11	30.16	0.23	10.03	0.16	15.7	0.66	75.04
A05	apatite	79.81	5.67	64.90	1.00	1.66	0.00	2.78	0.07	7.99	0.12	8.20	0.25	4.7	0.81	77.53
Z01	zircon	124.84	8.97	107.65	1.63	404.38	0.48	626.22	10.72	273.01	2.28	1.63	0.80	690.4	0.86	83.18
Z02	zircon	58.06	4.54	49.42	1.73	526.40	0.48	1772.35	70.65	828.24	27.48	55.52	5.61	1967.0	0.85	77.16
Z03	zircon	70.99	5.04	53.41	0.81	497.87	0.45	1551.95	26.63	719.93	10.90	16.24	16.81	1721.1	0.75	45.18
Z04	zircon	123.12	9.33	97.54	0.86	242.69	0.26	396.62	4.10	259.35	2.48	2.17	4.37	457.6	0.79	54.65
Z05	zircon	86.34	6.38	76.96	1.87	593.92	0.63	1227.96	35.39	824.29	18.19	17.73	1.04	1421.7	0.89	107.21
15RAY-JR061A03 *(61.707N, 137.277W) 1280m Early Jurassic, Long Lake Suite, granodiorite*																
Z01*	zircon	1376.61	96.94	1096.33	14.03	79.23	0.11	5.35	0.15	30.25	0.26	6.73	1.89	12.5	0.78	55.47
Z02*	zircon	318.79	22.58	249.99	4.11	17.33	0.02	8.09	0.15	18.95	0.60	6.98	5.68	12.5	0.78	52.91
Z03*	zircon	373.77	31.85	281.65	6.27	16.30	0.02	7.76	0.24	11.54	0.22	2.32	0.53	10.5	0.75	45.02
Z04	zircon	60.42	11.92	43.44	0.49	64.97	0.07	244.34	3.17	136.08	2.44	3.43	9.01	276.3	0.72	39.72
Z05	zircon	60.16	6.79	45.23	0.48	47.48	0.04	173.75	2.09	85.98	1.66	0.57	4.80	194.0	0.75	45.22
Z06	zircon	57.85	6.20	44.32	0.48	52.09	0.05	194.80	2.43	95.24	0.90	0.00	0.00	217.2	0.77	48.16
Z07	zircon	57.34	5.39	44.66	0.39	52.48	0.07	195.71	1.91	91.30	1.76	0.00	0.00	217.2	0.78	51.08
Z08	zircon	64.03	4.60	51.06	1.06	4.55	0.01	13.98	0.34	9.46	0.34	28.68	2.42	16.2	0.79	55.00
15RAY-EW014A01 *(61.954N, 137.137W) 1185m Early Jurassic, Long Lake Suite, monzonite*																
Z01	zircon	156.95	10.27	120.10	0.97	30.78	0.02	28.70	0.31	77.40	0.99	15.10	0.49	46.9	0.76	49.84
Z02*	zircon	1240.92	339.46	952.03	278.54	0.24	0.00	0.00	0.00	0.19	0.00	0.00	0.00	0.0	0.80	54.55
Z03*	zircon	203.90	14.14	177.13	2.01	65.11	0.05	57.36	0.78	41.45	0.35	5.83	0.38	67.1	0.87	87.18
Z04	zircon	178.61	12.57	146.17	2.45	30.94	0.03	31.90	0.66	28.88	0.41	9.61	0.26	38.7	0.82	62.39
Z05	zircon	171.06	22.90	130.44	1.68	180.33	0.30	237.26	3.33	69.45	0.75	0.00	0.00	253.6	0.76	46.75
Z06	zircon	166.15	20.35	127.01	1.17	203.25	0.27	278.42	2.77	64.67	0.54	0.00	0.00	293.6	0.76	47.05
Z07	zircon	166.84	12.59	134.89	2.21	148.60	0.14	190.59	3.41	48.46	0.62	0.02	1.58	202.0	0.81	58.51
Z08	zircon	172.72	12.47	138.84	2.09	221.44	0.27	271.26	4.53	89.57	0.56	0.04	1.08	292.3	0.80	57.17

Table 1c. cont'd

15RAY-MM003A01 *(61.915N, 136.899W) 1177m Early Jurassic, Long Lake Suite, granodiorite*

A01	apatite	65.87	4.59	46.82	0.92	2.15	0.01	5.91	0.16	10.83	0.17	3.38	0.31	8.5	0.71	49.21
A02*	apatite	119.14	13.10	78.12	2.71	4.54	0.02	7.34	0.38	14.05	0.09	6.13	1.01	10.6	0.65	40.50
A03*	apatite	156.17	43.12	85.13	8.50	4.97	0.04	9.16	1.10	6.45	0.18	9.55	1.79	10.7	0.54	29.97
A04*	apatite	125.75	10.83	68.74	3.38	3.45	0.02	6.69	0.47	10.67	0.16	6.71	0.76	9.2	0.54	31.90
A05	apatite	81.51	6.67	58.87	2.47	1.13	0.01	2.27	0.15	5.30	0.14	1.56	0.41	3.5	0.72	51.13
Z01*	zircon	243.92	16.45	156.54	1.96	40.57	0.23	19.44	0.23	118.34	2.02	21.28	6.25	47.2	0.64	33.40
Z02*	zircon	543.84	38.55	425.59	7.89	17.99	0.03	0.89	0.10	28.85	0.43	0.00	0.00	7.7	0.78	57.54
Z03*	zircon	500.70	34.69	377.17	5.44	12.91	0.03	0.33	0.08	25.08	0.21	0.00	0.00	6.2	0.75	51.23
Z04*	zircon	338.96	33.74	242.72	9.47	5.98	0.03	0.58	0.17	16.63	0.28	0.00	0.00	4.5	0.71	43.21
Z05*	zircon	207.16	19.85	159.16	1.58	154.39	0.14	157.18	1.78	86.18	1.17	2.26	5.20	177.4	0.76	47.58

15RAY-MM007A01 *(61.934N, 136.940W) 1165m Early Jurassic, Long Lake Suite, granodiorite*

A01	apatite	64.64	5.60	46.39	1.21	1.82	0.01	4.77	0.18	10.25	0.19	9.36	0.41	7.2	0.71	51.43
A02	apatite	92.82	6.70	74.30	1.04	2.63	0.00	3.92	0.09	10.73	0.13	8.01	0.34	6.4	0.80	73.25
A03	apatite	73.67	5.70	51.71	1.05	3.20	0.01	7.45	0.21	16.61	0.41	6.06	0.74	11.4	0.70	48.06
A04	apatite	67.61	4.98	53.35	1.04	2.97	0.01	5.92	0.18	18.13	0.44	10.31	0.38	10.2	0.79	69.75
A05	apatite	73.14	6.75	46.57	1.21	3.26	0.03	7.96	0.33	20.82	0.18	8.66	0.62	12.9	0.64	39.53
Z01	zircon	175.06	31.92	123.68	1.55	170.70	0.23	229.23	3.24	101.86	1.48	15.87	20.59	253.2	0.70	37.41
Z02	zircon	171.65	12.25	140.19	1.87	91.55	0.09	109.60	1.64	42.80	0.36	2.34	4.72	119.7	0.81	61.53
Z03	zircon	170.61	20.82	129.81	1.38	228.43	0.31	294.35	3.48	120.91	2.08	0.00	0.00	322.8	0.76	46.57
Z04	zircon	162.94	11.68	139.36	1.72	131.60	0.11	161.92	2.20	47.40	0.34	0.53	0.78	173.1	0.85	78.39
Z05	zircon	172.79	12.28	147.85	1.36	201.20	0.14	232.45	2.36	71.25	0.61	0.86	1.95	249.2	0.85	78.56

15RAY-MM009A01 *(61.861N, 136.977W) 1398m Early Jurassic, Long Lake Suite, granodiorite*

A01	apatite	112.89	7.81	85.72	1.02	10.09	0.01	13.70	0.24	32.87	0.43	25.66	1.07	21.4	0.76	59.39
A02	apatite	111.35	7.80	84.12	0.74	13.70	0.02	22.02	0.26	33.15	0.24	19.62	0.42	29.8	0.75	58.57
A03	apatite	93.80	6.90	74.30	1.16	3.45	0.01	6.34	0.13	8.92	0.09	14.28	0.39	8.4	0.79	68.55
A04	apatite	110.84	12.01	64.76	2.49	6.96	0.04	14.13	0.77	23.33	0.52	24.64	1.79	19.6	0.58	32.66
A05	apatite	123.58	9.44	83.88	1.89	6.31	0.02	8.43	0.30	22.36	0.51	19.06	0.44	13.7	0.67	45.35
Z01	zircon	153.76	20.44	113.98	1.37	240.15	0.53	355.99	4.71	132.03	1.33	0.00	0.00	387.0	0.74	42.42
Z02	zircon	148.34	10.81	116.12	1.27	314.69	0.24	460.24	5.58	159.48	1.60	0.00	0.00	497.7	0.78	51.42
Z03	zircon	188.82	13.42	159.90	1.37	487.42	0.54	471.79	4.87	365.23	2.51	2.71	1.85	557.6	0.84	75.00
Z04	zircon	147.80	33.78	99.59	1.18	678.55	0.92	1124.61	15.21	545.59	3.19	20.62	37.84	1252.8	0.67	33.51
Z05	zircon	176.53	30.61	124.03	1.28	227.29	0.26	292.56	3.47	185.61	3.16	8.92	23.48	336.2	0.70	37.11

* Grain not used in (U/Th)/He models

domains (**Figure 4**). These domains were defined by similarities in geography, lithology and primary crystallization age, consequently, the samples in each domain were predicted to preserve similar thermal histories. The three samples within the Northwestern domain are Permian to Early Triassic granitoids and were selected because they belonged to plutonic bodies thus less likely to possess grains with complex and protracted thermal histories, such as would be the case for detrital zircon. Samples 15RAY-MM055A01 and 15RAY-MM063A01 were selected to determine the distal thermal signature recorded from the batholith. Sample 15RAY-JC095A03 was selected to establish a baseline thermal history for the area that would be unaffected by the batholith's thermal signature. Five samples within the Central domain consist of foliated rocks from the Mississippian Simpson Range plutonic suite and vary from granodiorites to granites in composition. All samples were selected due to their proximity to the batholith and samples along the northwestern margin of the batholith were selected on either side of faults to possibly resolve any vertical displacement. The Southeastern domain is comprised of Early Jurassic monzogranite to granodiorite rocks that are all within the Aishihik batholith. Samples were selected from the interior to the margin of the igneous body to examine the differences in cooling patterns within an undeformed batholith.

Whole rock samples were crushed, sieved (63-250 μm), washed and processed through heavy (3.0 g/cm^3) liquid procedures using methylene iodide. (U-Th)/He thermochronology was conducted at the Thermochronology Research and Instrumentation Laboratory (TRaIL) (U-Th)/He facility at the University of Colorado at Boulder, USA. Individual mineral grains are handpicked using a Leica M165 binocular microscope equipped with a calibrated digital camera and capable of both reflected and transmitted, polarized light. The grains are screened for quality, including crystal size, shape, and the presence of inclusions. After characterization, grains are placed into small Nb tubes that are then crimped on both ends. This Nb packet is then loaded into an ASI

Alphachron He extraction and measurement line. The packet is placed in the UHV extraction line (~$3x10^{-8}$ torr) and heated with a diode laser to ~800-1100°C for 5 to 10 m to extract the radiogenic ^{4}He. The degassed ^{4}He is then spiked with approximately 13 ncc of pure ^{3}He, cleaned via interaction with two SAES getters, and analyzed on a Balzers PrismaPlus QME 220 quadrupole mass spectrometer. Degassed grains are then removed from the line, and taken to a Class 10 clean lab for dissolution. Apatite grains, still enclosed in the Nb tubes, are placed in 1.5 mL Cetac vials, spiked with a ^{235}U-^{230}Th tracer in HNO_3, capped, and baked in a lab oven at 80°C for 2 h. Zircon are dissolved using Parr large-capacity dissolution vessels in a multi-step acid-vapor dissolution process. Grains (including the Nb tube) are placed in Ludwig-style Savillex vials, spiked with a ^{235}U-^{230}Th tracer, and mixed with 200 µl of Optima grade HF. The vials are then capped, stacked in a 125 mL Teflon liner, placed in a Parr dissolution vessel, and baked at 220°C for 72 h. After cooling, the vials are uncapped and dried down on a 90°C hot plate until dry. The vials then undergo a second round of acid-vapor dissolution, this time with 200 µl of Optima grade HCl in each vial that is baked at 200°C for 24 h. Vials are then dried down a second time on a hot plate. Once dry, 200 µl of a 7:1 HNO_3:HF mixture is added to each vial, the vial is capped, and cooked on the hot plate at 90°C for 4 h. Once the minerals are dissolved, regardless of the dissolution process, they are diluted with 1 to 3 mL of doubly-deionized water, and taken to the ICP-MS lab for analysis. Mineral standards of Durango Apatite (31.5 Ma) and Fish Canyon Tuff Zircon (28.2 Ma) are routinely analyzed (degassed and dissolved) in conjunction with the samples with each run to ensure data integrity. Sample solutions, along with standards and blanks, are analyzed for U, Th, and Sm content using a Thermo Element 2 magnetic sector mass spectrometer. Once the U, Th, and Sm contents have been measured, He dates (raw date) and all associated data are

calculated on a custom spreadsheet made by CU TRaIL staff. The corrected date is the alpha-ejection corrected age, equal to the raw age divided by the alpha-ejection correction.

3.3. Northwestern domain results

The Northwestern domain is comprised of one Permian and two Triassic samples (**Figure 4; Table 1a**) that were analyzed for both apatite and zircon (U-Th)/He dates. The Stikine Suite is granitic with large potassium feldspar crystals (1-5 cm) and varying amounts of hornblende and biotite. The Sulphur Creek Suite is grey-pink equigranular granodiorite with hornblende and a moderate foliation. The dataset exhibits notable intrasample age dispersion that illustrates no obvious correlation with elevation. Eight apatite dates range from 31.9 ± 5.0 Ma to 84.9 ± 6.2 Ma, with eU concentrations from 0.4 to 26.9 ppm, exhibiting a positive correlation with an inflection at ~12 eU (**Figure 5a**). Twelve zircon dates range from 29.8 ± 5.9 Ma to 90.3 ± 24.0 Ma, with eU values from 2.2 to 2274.6 ppm. Date-eU plots for zircon analyses show that all the grains within each sample are clustered and no relationship is exhibited between the grains within the domain (**Figure 5b**). Date-equivalent spherical radius (ESR) plots for apatite show that the younger grains were smaller in size (30-40 μm) whereas the older grains were larger in size (55-60 μm; **Figure 1a DR**). Date-ESR plots for zircon show no correlation between date and grain size (**Figure 1b DR**). A few grains possessed cooling ages older than the crystallization age of the rock. One zircon grain from sample 15RAY-MM055A01 yielded an age of 492.7 ± 97.8 Ma and an apatite grain from 15RAY-JC095A03 with an age of 259.3 ± 32.4 Ma (**Table 1a**). In both cases, there was little to no uranium measured from the grains to obtain accurate and reliable ages.

3.4. Central domain results

The Central domain is comprised of five Mississippian samples (**Figure 4, Table 1b**) that were analyzed for both apatite and zircon (U-Th)/He cooling ages. The rocks are granite to

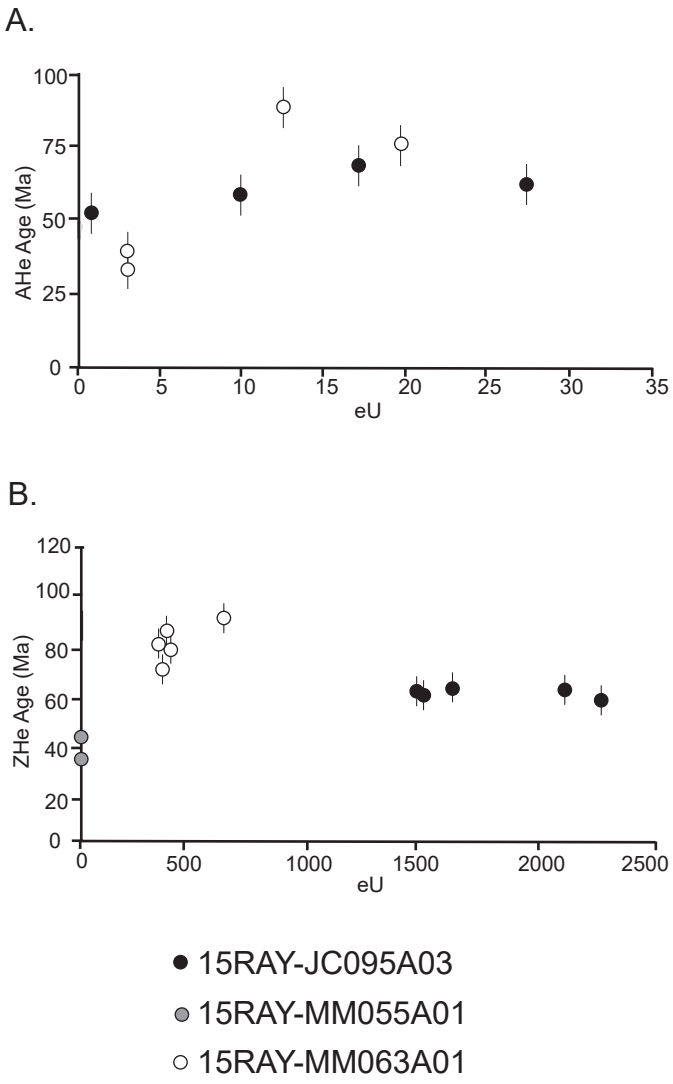

Figure 5: Northwestern domain. **A**: Single crystal (U-Th)/He apatite cooling ages from the Northwestern domain plotted against eU. **B**: Single crystal (U-Th)/He zircon cooling ages from the Northwestern domain plotted against eU. Plotted points of similar colour represent apatite and zircon grains from the same sample.

granodiorite, which are moderately foliated. Eleven apatite dates range from 32.7 ± 2.8 Ma to 178.4 ± 12.4 Ma, with eU values of 0.5 to 45.9 ppm (**Figure 6a**). No correlation is evident within the date-eU data. Seventeen zircon grains with ages from 118.3 ± 8.3 Ma to 309.5 ± 21.5 Ma possess eU concentrations of 37.2 to 1056.6 ppm, which exhibits a negative date-eU correlation (**Figure 6b**). Date-ESR plots for both apatite and zircon show no correlation between age and grain size (**Figure 1c DR; Figure 1d DR**), as well as there is no age-elevation relationship. Four grains with cooling ages older than the crystallization age of the rock were obtained. Sample 15RAYJR035A01 has two zircon grains with ages of 871.2 ± 67.7 Ma and 367.2 ± 25.6 Ma. The Neoproterozoic grain was broken and has a low, yet acceptable, uranium content which may have led to the older age, and the Devonian grain is possibly a xenocrystic component. One apatite grain from sample 15RAY-JR159A01 (256.0 ± 124.8 Ma) and one zircon grain from 15RAY-JR149A02 (1615.9 ± 134.1 Ma) can be explained by very low uranium concentrations (**Table 1b**).

3.5. Southeastern domain results

The Southeastern domain is comprised of eight Early Jurassic samples which are located in the Aishihik batholith (**Figure 4; Table 1c**) that were analyzed for both apatite and zircon (U-Th)/He dates. The rocks are monzonite to granodiorite with large potassium feldspar crystals (2-6 cm) and varying amounts of hornblende and biotite. Twenty-five apatite grains were analyzed, yielding ages range from 48.5 ± 4.9 Ma to 123.6 ± 9.4 Ma and eU values of 3.5 to 29.8 ppm. There lacks a clear date-eU relationship and instead a dispersed spread in He age and eU is evident (**Figure 7a**). Thirty-six zircon grains possess ages from 57.3 ± 5.4 Ma to 188.8 ± 13.4 Ma with a strong negative eU correlation from 16.2 to 1967.0 ppm (**Figure 7b**). Date-ESR plots for both apatite and zircon show no correlation between age and grain size (**Figure 1e DR; Figure 1f DR**). As with the other domains, the samples lack an age-elevation relationship. Some grains with

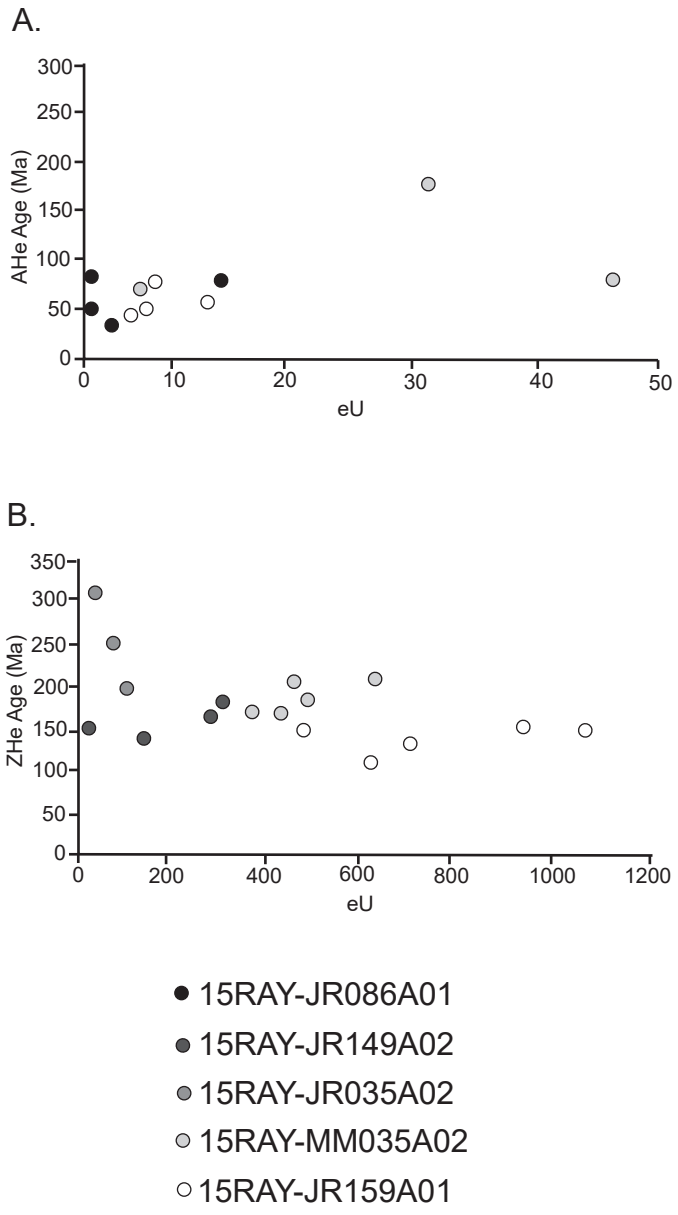

Figure 6: Central domain. **A**: Single crystal (U-Th)/He apatite cooling ages from the Central domain plotted against eU. The error bars on this graph are smaller than the plotted points. **B**: Single crystal (U-Th)/He zircon cooling ages from the Central domain plotted against eU. The error bars on this graph are smaller than the plotted points. Plotted points of similar colour represent apatite and zircon data from the same sample.

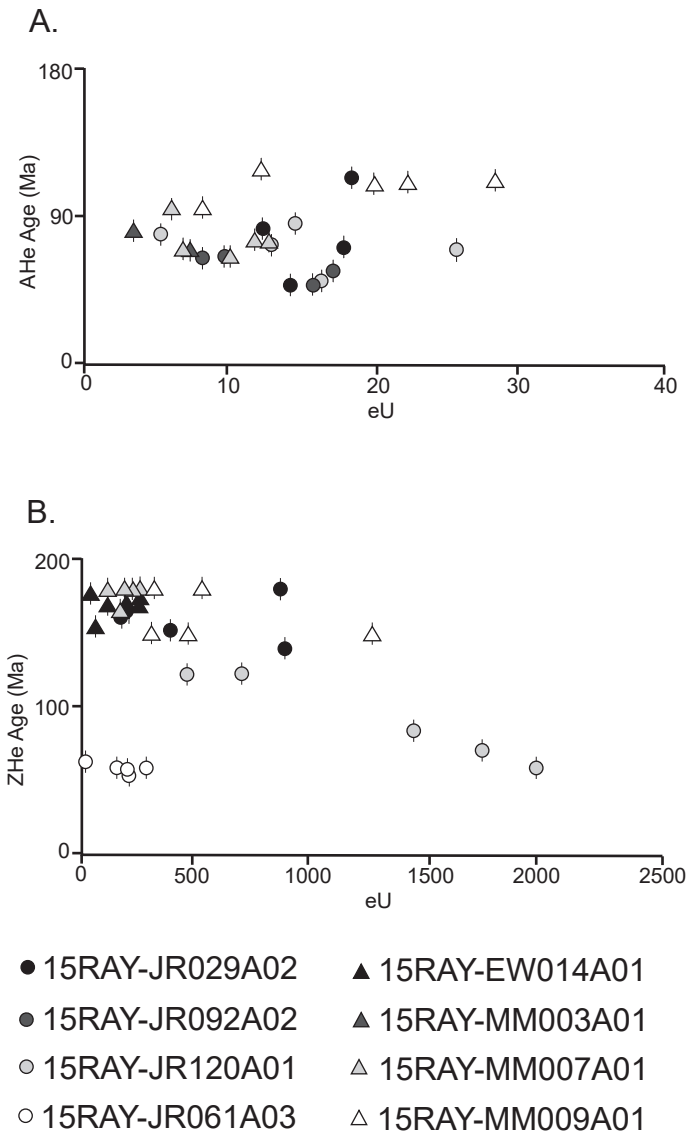

Figure 7: Southeastern domain. **A**: Single crystal (U-Th)/He apatite cooling ages from the Southeastern domain plotted against eU. **B**: Single crystal (U-Th)/He zircon cooling ages from the Southeastern domain plotted against eU. Plotted points of similar colour/symbol represent apatite and zircon data from the same sample.

cooling ages older than the crystallization age of the rock were found. Three zircon grains from sample 15RAY-JR061A03 (1376.6 ± 96.9, 318.8 ± 22.6 Ma and 373.7 ± 31.8 Ma) and two zircon grains from sample 15RAY-EW014A01 (1240.9 ± 339.5 Ma and 203.9 ± 14.1 Ma) are likely not zircon grains (**Table 1c**). All five zircon grains that were analyzed in sample 15RAY-MM003A01 have cooling ages that are older than the crystallization age. Grains 2, 3 and 4 (543.8 ± 38.6 Ma, 500.7 ± 34.7 Ma and 339.0 ± 33.7 Ma) have a low uranium content which may have led to the older ages, and grains 1 and 5 (243.9 ± 16.4 Ma and 207.2 ± 19.9 Ma) are interpreted to be xenocrystic zircons.

4. Numerical modelling

Single grain, corrected ages for each sample may exhibit a large dispersion, which make it difficult to readily interpret the data. Spuriously older dates may be from He implantation from adjacent grains or caused from U-rich inclusions within the grain itself (Flowers et al., 2009; Murray et al., 2014). Young ages may be attributed to broken or zoned grains (Ketcham, 2012; Spiegel et al., 2009). Yet, there is likely meaning in the age dispersion that needs to be reconciled within the context of the local geology. The program HeFTy (Ketcham, 2005) was used to numerically model the data from those samples which are believed to have a shared thermal history (Northwest, Central, Southwest domains). HeFTy uses the apatite radiation damage accumulation and annealing model (RDAAM) and zircon radiation accumulation and annealing model (ZRDAAM) to account for factors (discussed above) that influence a grain's cooling age (Flowers et al., 2009; Guenther et al., 2013). HeFTy produces ten thousand t-T paths between user-specified t-T constraints using a Monte Carlo random search, and calculated a modeled age for the zircon grains while considering zircon specific parameters (composition and grain size). Representative

grains from a sample are chosen for the model that fully capture the dispersion in He-date, size, and eU concentration. HeFTy can produce both forward and inverse models of the data, which are used in parallel to get the most consistent thermal model for each sample. Inverse models require a set of pre-conditions or independent geologic constraints such as unconformities, independent thermochronologic data or other known time-temperature (t-T) events (i.e. Au mineralization) to generate plausible t-T pathways that are applicable to the study area. The different constraints that were used are illustrated as t-T boxes on each inverse model, and the constraint boxes were purposely kept broad in temperature and in time to explore the range of plausible thermal histories. For each inverse model, solution envelopes define the upper and lower temperature boundary of 'good' and 'acceptable' paths at any point in time. 'Good' paths correspond with unitless values of >0.5, with the connotation that the modeled and measured ages overlap (Ketcham, 2013). The goodness-of-fit measurements review the discrepancy between the detected and predicted values for each model, with the intent to be 'good' to the limit of statistical precision, defined so the mean of goodness-of-fit statistics measured is 0.5 and the minimum is 1/(N+1), where N represents the statistical sample size (Ketcham, 2005). 'Acceptable' paths have less consistent modeled and measured ages with values >0.05. In contrast, forward models require the input of a specific t-T paths, usually generated from inverse models of a single sample, and are used to investigate the compatibility of larger sample sizes (i.e. more grains, more samples) with a specific, predicted t-T model. Creating both inverse and forward models for the dispersed cooling ages allows internally consistent thermal models to be evaluated.

4.1. Northwestern domain

Inverse models for each sample in the domain were developed (**Figures 2-3 DR**), however one representative model will be discussed (**Figure 8**). Sample 15RAY-MM063A01 is a

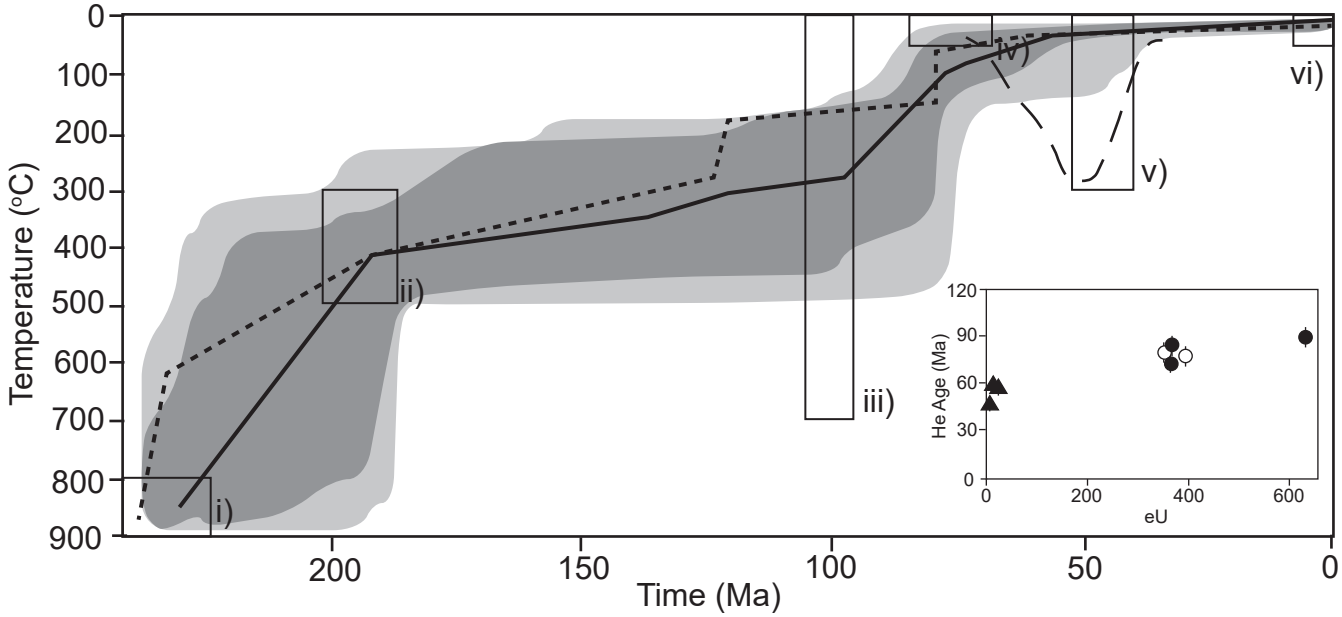

Figure 8: Inverse model for one representative sample (15RAY-MM063A01) for the Northwestern domain. The constraint boxes include: i) crystallization ages, ii) HAr/ BtAr dates, iii) Mount Nansen unconformity, iv) Carmacks unconformity, v) potential Eocene event, and vi) surface. Dark grey envelopes represent t-T pathways with a 'good fit' and light grey envelopes represent t-T pathways with an 'acceptable fit'. Long dashed line represents one sample (15RAY-JC095A03) that exhibits Eocene cooling. The thick black line in the model represents the weighted mean path of the sample and the small dashed line represents the line of best fit. The He age-eU plot in the bottom right corner illustrates apatite (triangles) and zircon (circles) grains from this sample that were used to make the inverse model. Filled symbols indicate that the grain was used in the model, while unfilled symbols denote grains that were not used.

granodiorite from the Late Triassic Stikine Suite and is representative because the model exhibits a common and predominant thermal patterns of all the samples within the Northwestern domain. The Stikine suits is also the most prevalent lithology within the domain. This model uses both apatite and zircon data to determine a robust and plausible thermal history, whereas some of the other models in the domain use fewer minerals to define their t-T path. Raw apatite and zircon dates along with their corresponding U, Th, and Sm values and grain sizes were utilized as the primary input. For 15RAY-MM063A01, six grains (three zircon, three apatite) were selected that represent the range of date and eU variability. For the model, ZHe dates range from 73.0 ± 7.4 Ma to 90.3 ± 24.0 Ma and eU values vary from 364.6 to 628.6 ppm. AHe dates range from 46.7 ± 5.2 Ma to 58.8 ± 9.3 Ma and eU values differ from 9.9 to 26.9 ppm (**Table 1a**). Each model was defined with six independent geological constraints that were used to resolve a plausible t-T pathway: crystallization age, available $^{40}Ar/^{39}Ar$ ages, two known unconformities, an Eocene cooling event and present-day surface conditions. The crystallization age of the Stikine Suite is ca. 228-210 Ma (Zagorevski et al., 2014) and the Sulphur Creek is 265-260 Ma (Mortensen, 1990; Ryan et al., 2014; Ryan, et al., 2016). Published $^{40}Ar/^{39}Ar$ biotite cooling age is 187.0 ± 1.3 Ma and hornblende is 186.0 ± 1.3 Ma (Joyce et al., 2015). There are two known unconformities: ca. 110-90 Ma Mount Nansen unconformity and the ca. 73-68 Ma Carmacks unconformity, both determined based on the age of volcanic rock directly on crystalline basement. An orogen-wide cooling and exhumation event that is recorded in British Columbia and Alaska occurred during the Eocene, and is being evaluated in the (U-Th)/He thermochronology models with a constraint box at that time to allow the model to explore possible heating-cooling events.

Viable 'good' and 'acceptable' t-T paths were generated for sample 15RAY-MM063A01 from the Northwestern domain. The inverse model illustrates relatively rapid cooling (10°C/m.y.)

until 190 Ma when the rate begins to slow to 6°C/m.y. In the middle Cretaceous, cooling accelerates again (10°C/m.y.) until it reaches the surface in the Late Cretaceous. Initial models of sample 15RAY-MM063A01 did not converge to define good paths and were difficult to resolve without including the moderate closure temperature (300-500°C) constraints from the published biotite and hornblende $^{40}Ar/^{39}Ar$ data. The majority of the Northwestern domain apparently remained at the surface until present day conditions. All three samples in the Northwestern domain exhibit similar cooling patterns with only one difference in sample 15RAY-JC095A03. This sample was heated above the ZHe PRZ after the Late Cretaceous, which allowed it to record the Eocene cooling event and has remained at the surface since that time.

Forward models require the input of a specific t-T path and generates limits on date-eU relationships to assess the compatibility of the analytical data against the proposed t-T path, which ideally accounts for the He-date dispersion. One forward model was generated that is representative of the Northwestern domain (**Figure 9a**). A plausible t-T path was selected for the forward model by consulting with the t-T paths that were generated by the inverse models and the lines of best fit from all the samples within the domain (**Figure 8; Figures 2-3 DR**) to ensure that the path would be faithful to the analytical data. The proposed forward t-T path follows a generalized version of the inverse model output for sample 15RAY-MM063A01 (**Figure 9a**). The result of the models are He date-eU curves for both zircon and apatite, which help explain the relationship between variations in cooling age, eU and grain size. Two or more curves define an 'envelope' in date-eU space, capturing a range of plausible ages and eU values that may be obtained with the forward models and allows more confidence in the interpretation. In the example from the Northwestern domain, the 'envelope' for the apatite date-eU plot ranges from 30 to 60 μm (ESR) and for the zircon date-eU plot ranges from 30 to 120 μm (ESR). In the Northwestern

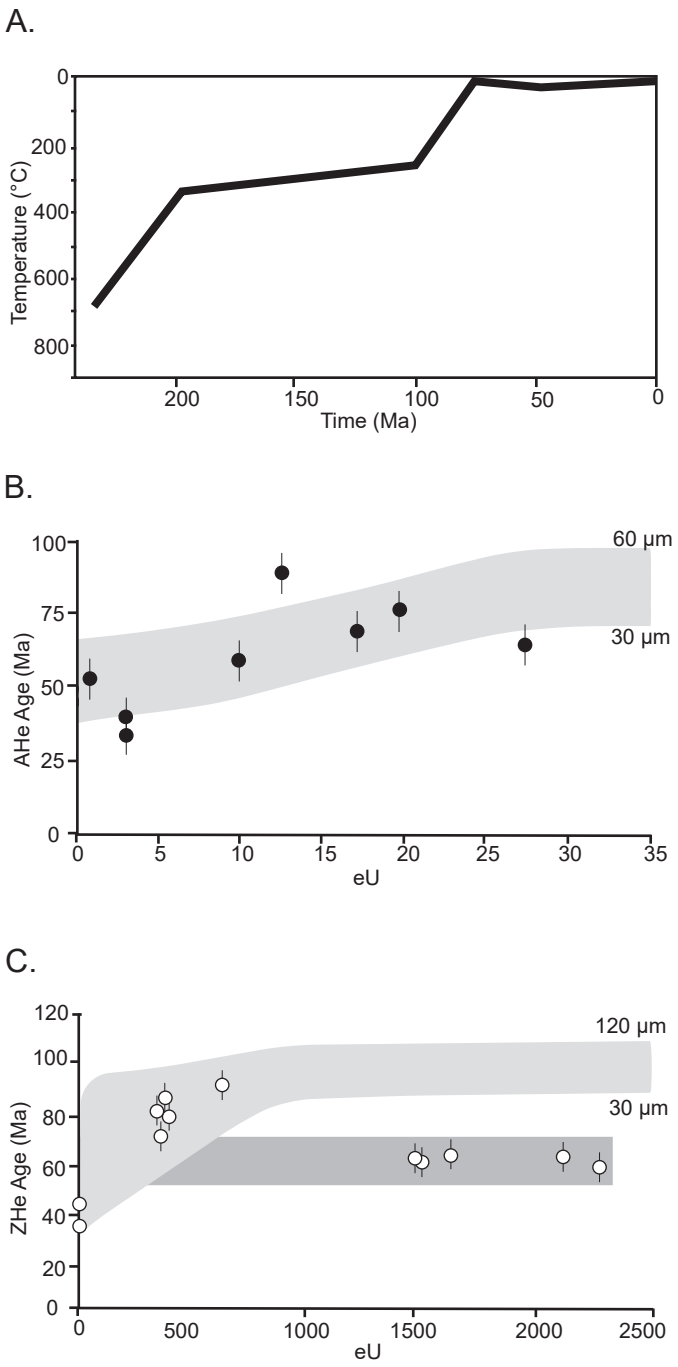

Figure 9: Northwestern domain **A**: Representative forward model of the Northwestern domain which demonstrates a plausible t-T path. **B**: Single crystal (U-Th)/He apatite cooling ages from the Northwestern domain plotted against eU. **C**: Single crystal (U-Th)/He zircon cooling ages from the Northwestern domain plotted against eU. The light grey polygon represents the range in grain size found in the Northwestern domain in apatite and zircon. The five grains outside of the ZHe envelope are all from one sample (15RAY-JC095A03), which is different from the rest of the domain in the case that it is the only sample which exhibits an Eocene cooling event (dark grey polgon).

domain, the proposed forward model is a plausible t-T path for the majority of apatite grains that were analyzed, as most (63%) of the grains lie within the 'envelope' (**Figure 9b**). Date-eU plots for zircon however only satisfy 15RAY-MM063A01 and 15RAY-MM055A01, but the five grains from sample 15RAY-JC095A03 are substantially younger (**Figure 9c**). These zircon cooling dates are all Eocene in age, with markedly higher eU values, suggesting this sample has a different and younger history. Other forward models were attempted (**Figures 4 DR**), which were not supported by the analytical data and consequently were deemed unlikely thermal histories.

4.2. Central domain

Inverse models for each sample of the Central domain were developed, however one representative model will be discussed (**Figure 10**). Sample 15RAY-MM035A02 is a granite from the Mississippian Simpson Range plutonic suite and was selected as the representative sample to model. The apatite and zircon grains chosen within the model were chosen to show a range in grain size, He date and eU. The input parameters are the same as the Northwestern domain with similarly six independent constraints: crystallization age, published $^{40}Ar/^{39}Ar$ data, two known unconformities, an Eocene cooling event and present-day surface conditions. The crystallization age of the Simpson Range Suite is ca. 356-345 Ma (Ryan et al., 2014; Ryan et al., 2016). The $^{40}Ar/^{39}Ar$ cooling age data, timing of the unconformities, and magnitude of the Eocene event are identical as those utilized in the Northwestern domain. For sample 15RAY-MM035A02, three grains (one zircon, two apatite) were selected that exhibit a range of date and eU variability. The ZHe date used is 186.2 ± 20.9 Ma with an eU value of 502.3 ppm (**Table 1b**). Only one zircon grain was used in the simulation, so a zircon with a date closest to the mean ZHe date of the domain was chosen for the representative model. The eU concentration between all of the analyzed grains

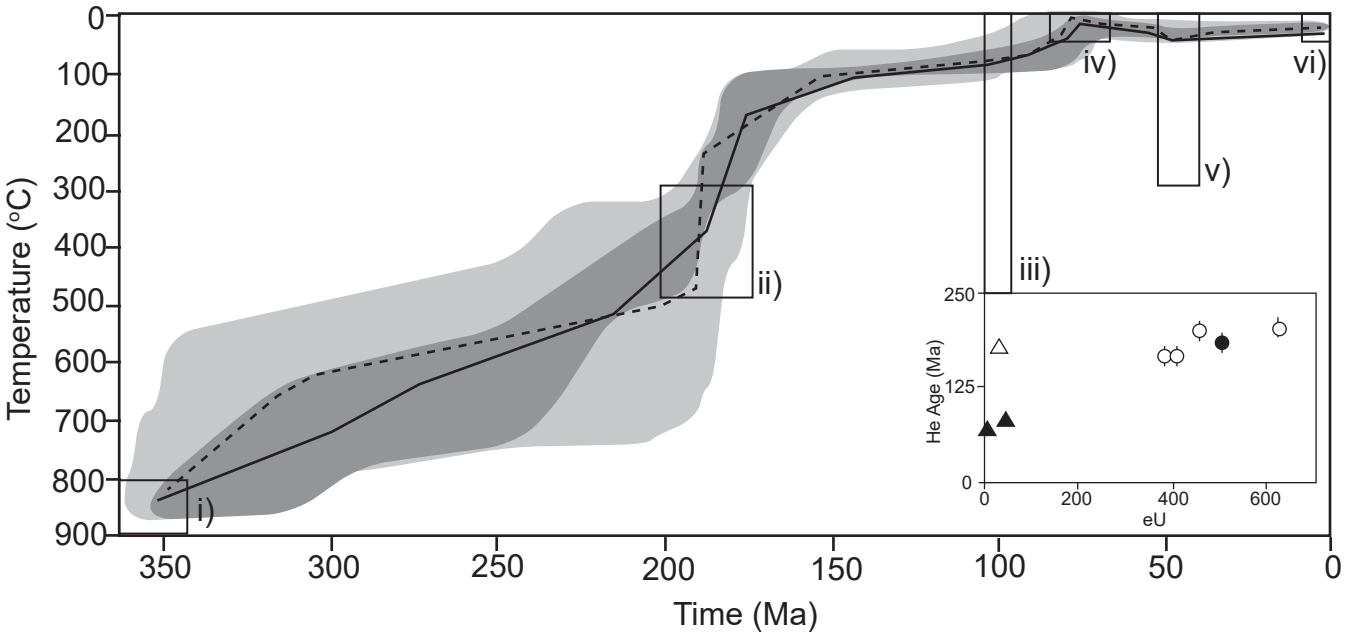

Figure 10: Inverse model for one representative sample (15RAY-MM035A02) for the Central domain. The constraint boxes include: i) crystallization ages, ii) HAr/ BtAr dates, iii) Mount Nansen unconformity, iv) Carmacks unconformity, v) potential Eocene event, and vi) surface. Dark grey envelopes represent t-T pathways with a 'good fit' and light grey envelopes represent t-T pathways with an 'acceptable fit'. The thick black line in the model represents the weighted mean path of the sample and the small dashed line represents the line of best fit. The He age-eU plot in the bottom right corner illustrates apatite (triangles) and zircon (circles) grains from this sample that were used to make the inverse model. Filled symbols indicate that the grain was used in the model, while unfilled symbols denote grains that were not used.

were relatively similar. AHe dates that were selected range from 68.0 ± 6.7 Ma to 81.1 ± 11.5 Ma and eU values between 7.2 to 45.9 ppm (**Table 1b**).

The inverse model resolves steady cooling (5°C/m.y.) until the domain reaches the surface in the Late Cretaceous. Upon closer evaluation of the model there is a possibility of a minor (~25-50°C) re-heating event after it reached surface conditions in the Late Cretaceous (**Figure 10**). However, it is difficult to determine the significance of a relatively small temperature change at such shallow conditions. No obvious Eocene cooling event was recorded in the Central domain as resolved through the inverse models.

One forward model was generated that is representative of the cooling history of the Central domain (**Figure 11a**), and that path is based on the t-T history resolved from the inverse model. By taking into account all of the inverse models and lines of best-fit from the Central domain (**Figure 10; Figures 5-8 DR**), a plausible t-T path was created for the forward model that would represent the domain as a whole. Using this forward model, we evaluated date-eU plots for zircon and apatite grains from the Central domain to test the plausibility of the models generated. Single crystal (U-Th)/He zircon and apatite cooling ages from the Central domain were plotted against eU. Within each sample, there are age and eU dispersions that may be a result from varying grain size because larger grains can retain more ^{4}He, which can record older ages. By modelling two or more date-eU curves, we can obtain an envelope in date-eU space that illustrates the range in grain size within the domain. This envelope should capture a range of plausible ages and eU values that may be obtained with the forward model. The envelope for the apatite and zircon date-eU plots ranges from 30 to 100 μm (ESR). In the Central domain, the age and eU dispersion can be explained from varying grain sizes as the majority (82%) of the apatite grains fall inside the envelope, with the exception of two outliers (**Figure 11b**). The zircon date-eU plot is similar to

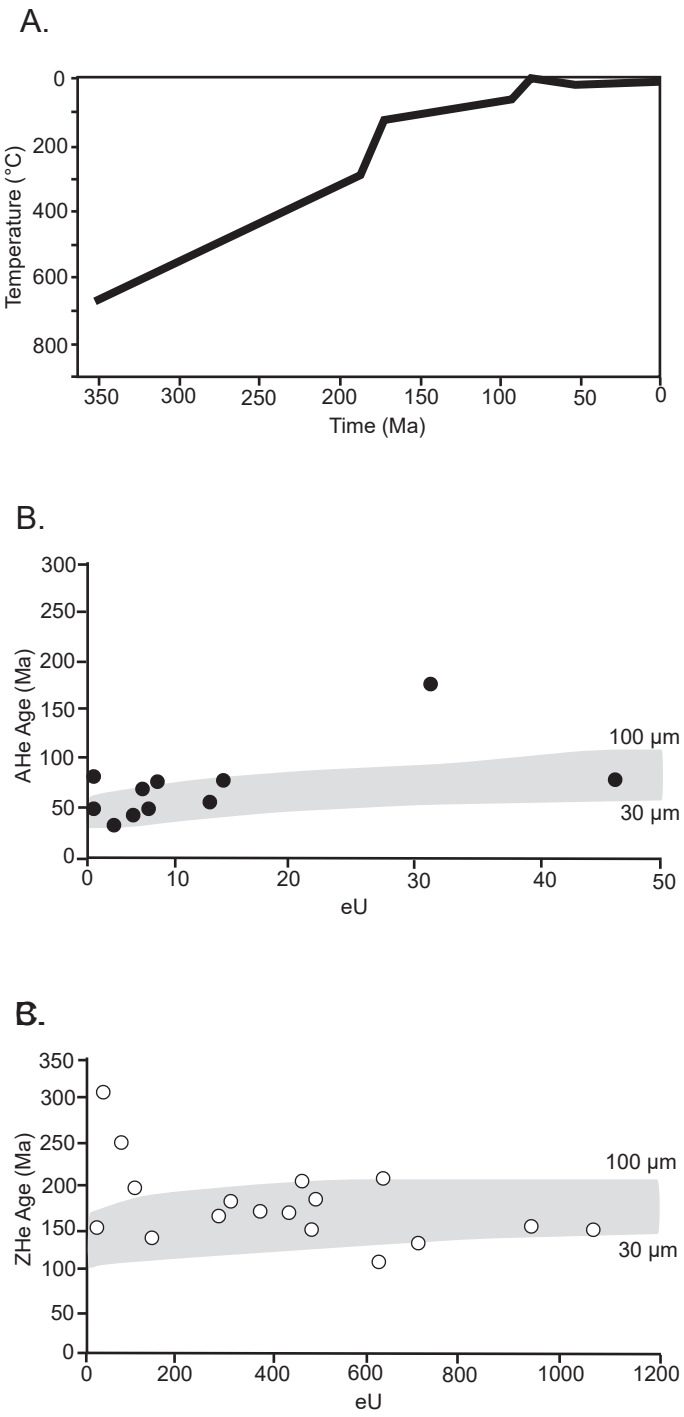

Figure 11: Central domain. **A**: Representative forward model of the Central domain which demonstrates a plausible t-T path. **B**: Single crystal (U-Th)/He apatite cooling ages from the Central domain plotted against eU. The error bars on this graph are smaller than the plotted points. Grey polygon represents the range in grain size found in the central domain. **C**: Single crystal (U-Th)/He zircon cooling ages from the Central domain plotted against eU. The error bars on this graph are smaller than the plotted points. Grey polygon represents the range in grain size found in apatite and zircon the Central domain. Three zircon grains (all from sample 15RAY-JR035A01) have low eU – old ages and are not within the ZHe envelope, which can be explained from He implantation.

apatite, as the majority (76%) of zircon grains lie within the 'envelope' (**Figure 11c**). Three of the zircon grains that do not lie within the envelope, which record older ages with lower eU are from sample 15RAY-JR035A02 and may indicate of He implantation. **Figure 9 DR** show forward models that do not represent the data and therefore are not deemed a plausible thermal history for the domain.

4.3. Southeastern domain

Inverse models for each sample of the Southeastern domain were developed, however one representative model will be discussed (**Figure 12**). Sample 15RAY-MM009A01 is a granodiorite from the Early Jurassic Long Lake Suite at the center of the batholith and both apatite and zircon grains were used in the models. Three grains (two zircon, one apatite) were selected that demonstrate a range of date and eU variability. ZHe dates that were selected are 148.3 ± 10.8 and 147.8 ± 33.8 Ma with eU values of 1252.8 and 497.7 ppm. The AHe date that was selected is 110.8 ± 12.0 Ma and the eU value is 19.6 ppm (**Table 1c**).The input parameters are the same as the other two domains, however only five independent constraints: crystallization age, two known unconformities, an Eocene cooling event and present-day surface conditions. The crystallization age of the Long Lake Suite is ca. 190-180 Ma (Joyce et al., 2016). The timing of the unconformities, and magnitude of the Eocene event are identical as those utilized in the other domains.

The inverse model indicates immediate cooling directly following emplacement of the batholith at a rate of 15°C/m.y. until the Late Jurassic-Early Cretaceous when the rate slows to 2°C/m.y. and reaches surface condition during the mid-Cretaceous (**Figure 12**). Similar to the Central domain, the thermal history slightly changes from 10°C to 50°C after the domain reaches surface conditions in the Late Cretaceous. This is relatively insignificant heating, and no Eocene

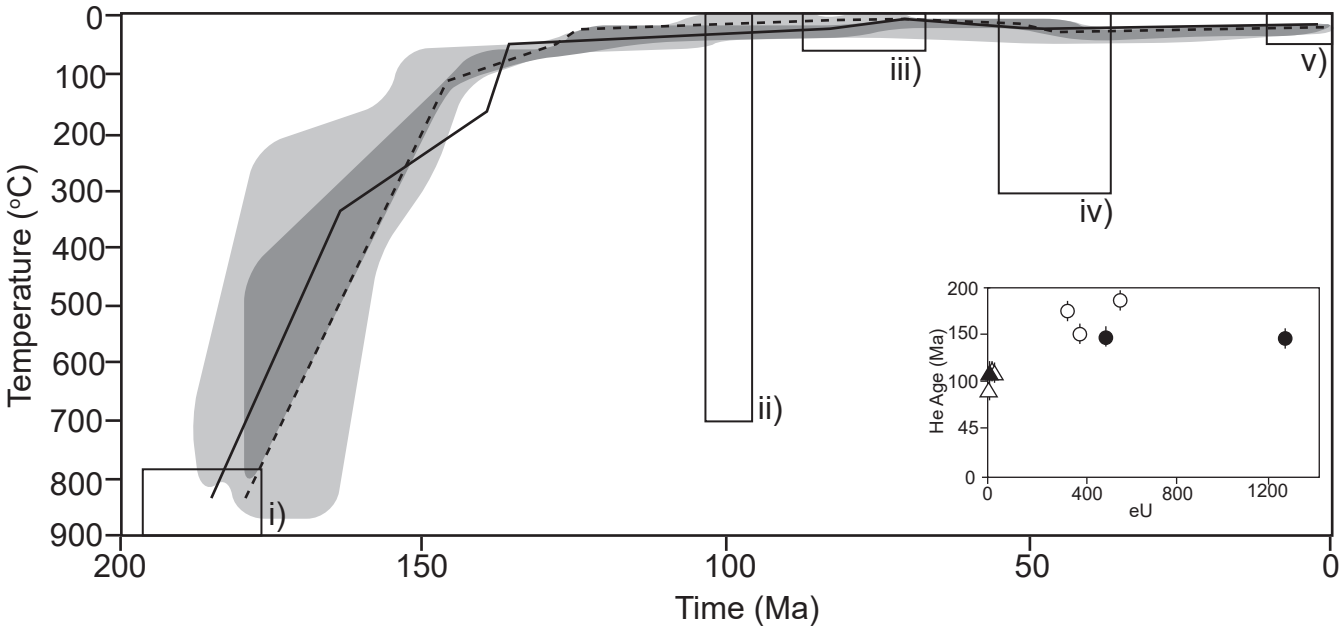

Figure 12: Inverse model for one representative sample (15RAY-MM009A01) for the Southeastern domain. The constraint boxes include: i) crystallization ages, ii) Mount Nansen unconformity, iii) Carmacks unconformity, iv) potential Eocene event, and v) surface. Dark grey envelopes represent t-T pathways with a 'good fit' and light grey envelopes represent t-T pathways with an 'acceptable fit'. The thick black line in the model represents the weighted mean path of the sample and the small dashed line represents the line of best fit. The He age-eU plot in the bottom right corner illustrates apatite (triangles) and zircon (circles) grains from this sample that were used to make the inverse model. Filled symbols indicate that the grain was used in the model, while unfilled symbols denote grains that were not used.

cooling is evident in the Southeastern domain. Initial models of 15RAY-MM009A01 and other samples in the Southeastern domain were not converging due to the fact the batholith was expected to reach the surface by the Early Cretaceous. It was only when the models were adjusted to allow the t-T path to reach surface conditions by the mid-Cretaceous did the models converge.

One plausible forward model was generated that is representative of the Southeastern domain (**Figure 13a**), using all of the inverse models as a template to create a generalized forward model (**Figure 12; Figures 10-16 DR**). Single grain (U-Th)/He zircon and apatite cooling ages from the Southeastern domain were plotted against eU. Using the range of grain size exhibited in the domain, date-eU curves were generated and an envelope was created to represent this information. The range in grain size used to create the envelope for the apatite date-eU plot is 30 to 100 μm (ESR) and 30 to 110 μm (ESR) for the zircon date-eU plot. Typically, grain analyses that accurately represent the model should fall within the grain envelope. With the proposed model, a moderate amount (80%) of the apatite data can be explained by the t-T history (**Figure 13b**), whereas a modest (64%) amount of the grains lies within the zircon 'envelope' (**Figure 13c**). Two samples (15RAY-JR061A03, 15RAY-JR120A01) that do not lie within the ZHe grain envelope and have Cretaceous cooling ages. Both samples are expected to have cooled quickly as their cooling ages are relatively consistent within each sample. Sample 15RAY-JR120A01 has five apatite cooling ages that also reflect this Late Cretaceous cooling recorded by the zircon cooling ages. **Figures 17 DR** show alternative forward models that do not explain the analytical data and are therefore unlikely thermal histories for the domain.

5. Discussion

5.1. Cooling rates and spatial differences

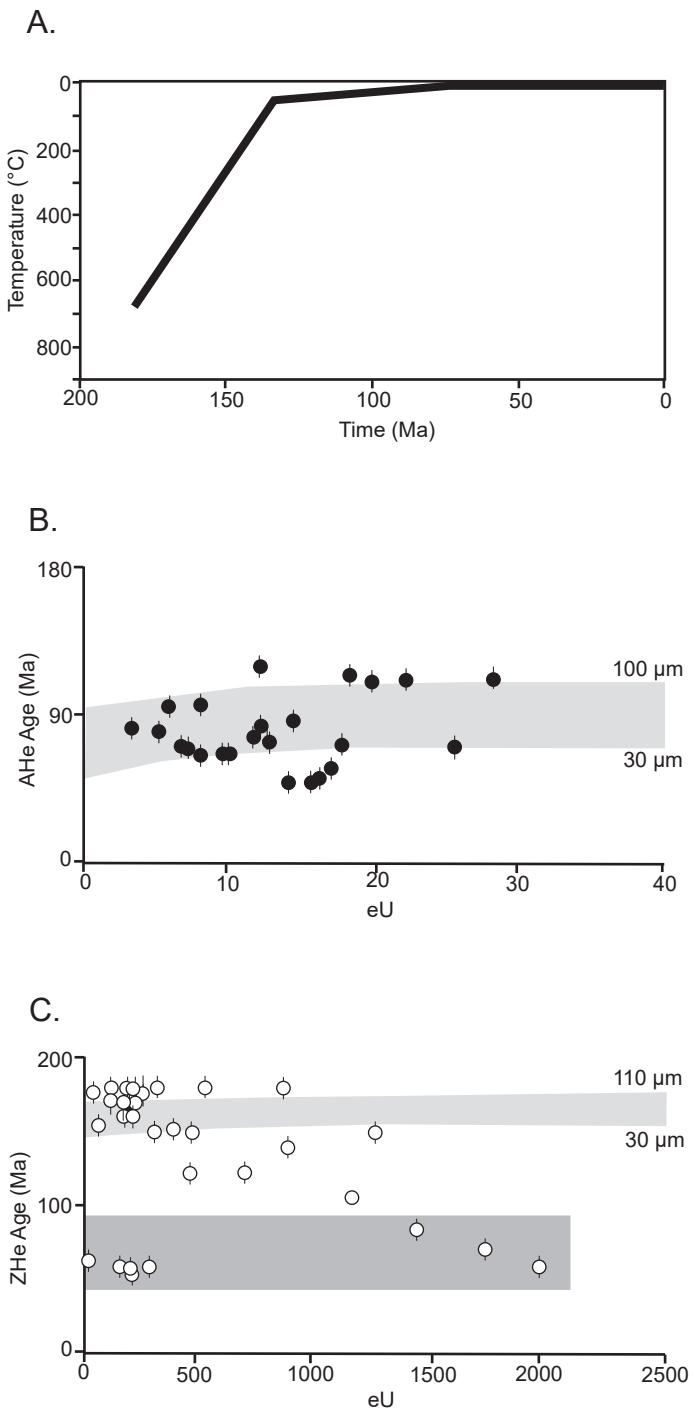

Figure 13: Southeastern domain. **A**: Representative forward model of the Southeastern domain which demonstrates a plausible t-T path. **B**: Single crystal (U-Th)/He apatite cooling ages from the Southeastern domain plotted against eU. **C**: Single crystal (U-Th)/He zircon cooling ages from the Southeastern domain plotted against eU. The light grey polygon represents the range in grain size of apatite and zircon found in the Southeastern domain. The grains that are not within the ZHe envelope are from two samples (15RAY-JR120A01 and 15RAY-JR061A03 - highlighted in the dark grey polygon). Sample 15RAY-JR120A01exhibits high eU – young ages which can be explained by the helium diffusion kinetics. Sample 15RAY-JR061A03 displays moderate eU and young ages that are very close together which can be evidence of a sample that was quickly cooled.

In **Figure 14**, plausible synoptic thermal histories are illustrated for the three domains as resolved by the numerical models of the (U-Th)/He data. In panel A (ca. 180 to 140 Ma), the thermal histories of the Central and Southeastern domains appear to have similar cooling rates, albeit midcrustal cooling is offset by ca. 10 m.y., whereas the Northwestern domain remained warmer and cooled slower. The Aishihik batholith intruded into YTT ca. 190-180 and witnessed relatively rapid cooling and probably exhumation after its emplacement, as exhibited by the Southeastern domain with cooling rates up to ~15°C/m.y. The Central domain mirrored a similar thermal path due to its proximity to the batholith and recorded a cooling rate of ~7°C/m.y. The Northwestern domain is the furthest from the batholith and its thermal history is not apparently affected by the large batholith. Consequently, the Northwestern domain may be considered the baseline thermal history for the exposed crust in the Aishihik region, possessing cooling rates of ~5°C/m.y. until ca. 140 Ma. In panel B of **Figure 14** (ca. 140 to 75 Ma), the batholith is relative cool (<100°C) and continued to cool at a rate that was similar to the adjacent Southeastern domain, which is slightly warmer (and deeper?). The Central and Southeastern domain had cooling rates of ~1.5°C/m.y. The Northwestern domain continued to cool at the rate of ~5°C/m.y., with a very slight increase later in this time period. In panel C in **Figure 14** (ca. 75 Ma to Recent), all of the samples have reached the surface to achieve an unconformity with the Carmacks volcanic sequence. The rocks remained cool and at the surface until present day, with the possible exception of one sample (15RAY-JC095A03), which recorded an Eocene cooling signature. The Central and Southeastern domain were not perceptively heated since the unconformities within the resolution of the (U-Th)/He data. Notably, some models that exhibited cooling in the Cretaceous did not converge until the models were forced to explore an event in the middle Cretaceous that allowed the paths to reach the surface at that time.

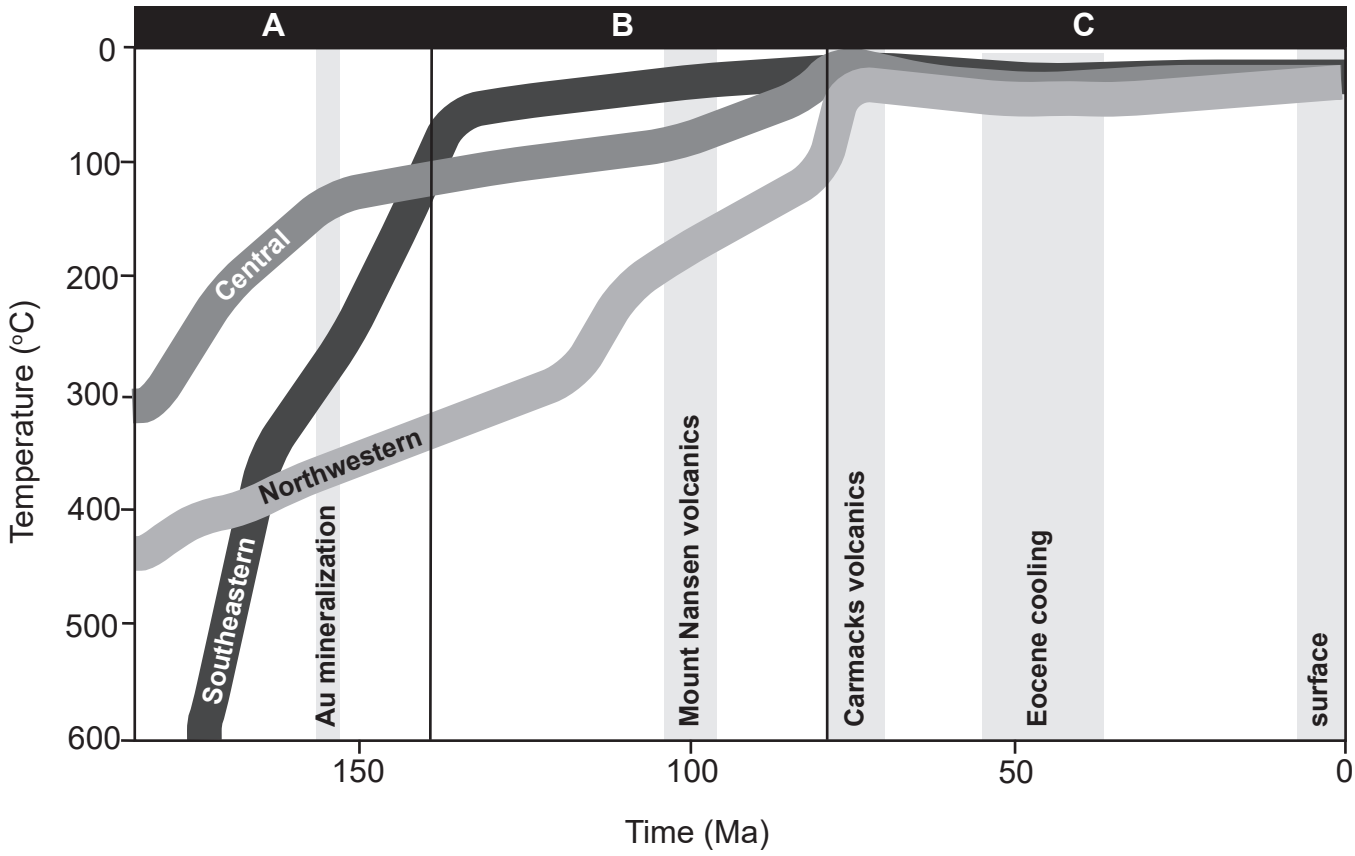

Figure 14: Summary of tectonothermal history of all three domains. The diagram is focused on the low temperature cooling history and only illustrates the thermal history of the samples from 600°C and lower. t-T pathways of each domain represent the line of best fit of each representative inverse model from figures 8, 10, and 12. The timing of various geologic events that may have affected the region are superimposed as shaded columns in the diagram. The figure has been divided into three panels. Panel A (ca. 180 to 140 Ma); Panel B (ca. 140 to 75 Ma); Panel C (ca. 75 Ma to Recent). See text for discussion.

When the Aishihik batholith intruded the northeastern YTT, the host rock was likely still quite warm (300-400°C) based on the $^{40}Ar/^{39}Ar$ ages from the basement. Due to the low (U-Th)/He closure temperature (<200°C) of zircon and even lower closure temperature of apatite, the timing of batholith intrusion is not recorded in the (U-Th)/He data. However, from ca. 190-175 Ma there is a marked increase in the cooling rate in the Central domain within 500 m of the batholith margin (i.e. 15RAY-JR035A01, 15RAY-MM035A02). The domain had been steadily cooling at a rate of 5°C/m.y. for 160 m.y. until 190 Ma when the rate doubled to 10°C/m.y. After 175 Ma, the rate of cooling returned to 5°C/m.y. until reaching the surface in the Late Cretaceous. The other three samples of the Central domain do not show this sharp increase in cooling rate during the emplacement of the batholith. The two samples that record a sharp increase in cooling are close to one another (<1 km) so it is possible that their marked rate change was due to faulting or other tectonism. However, the numerous northwest-southeast trending faults that disjoint the northwestern border of the Aishihik batholith are proposed to be Cretaceous (Ryan et al., 2017) and the sharp increase in cooling rate was recorded in the Early Jurassic, so it was unlikely caused by those mapped faults. The sharp increase in cooling rate could be possibly explained by assessing the batholith's geometry. When a large batholith intrudes into the host rock, space is needed to become available to accommodate the new volume of material, which can cause uplift of the surrounding host rock, in turn causing cooling. However, the Aishihik batholith has a lopolithic body that tapers to the west (Johnston and Erdmer, 1995), which means that the western side of the domain was thinner allowing for less accommodation space to be needed. It is unlikely that a large amount of vertical displacement would have occurred to allow for such a sharp increase in cooling.

Upon examination of the (U-Th)/He data and numerical models in a lateral context, cooling ages are apparently older in the northwest and younger to the southeast. Ignoring the domains and looking solely at when samples cool to surface temperatures, samples that are located in the northwest of the study area reached the surface by ca. 100 Ma to be unconformably overlain by the Mount Nansen volcanic sequence. All of the other samples located in the southeast in the study area reach surface temperatures in the Late Cretaceous to attain an unconformity with the Carmacks volcanics (73-68 Ma), with the exception of sample 15RAY-MM009A01. The approximate southward cooling age trend is consistent with the regional northward tilt of the YTT crust within the Aishihik region (Johnston and Erdmer, 1995), and suggests some crustal block rotation occurred after intrusion of the batholith. Further, there are numerous northwest trending brittle faults along the margin of the Aishihik batholith (**Figure 2**, **Figure 4**) that control some of the placement of the Mount Nansen group indicating that the deformation is middle Cretaceous or younger. The displacement across some of the mapped (or unmapped) faults may explain the slightly variable thermal histories witnessed in the Cretaceous. Within a vertical context, of the sixteen samples collected, the distance between highest and lowest location is ~300 m. Assuming a consistent moderate regional geothermal gradient, it is unlikely that the narrowness of the exposed crustal section is wide enough to have recorded disparate erosive processes and landscape development. Further, a temporary elevated geothermal gradient caused by the batholith cannot be resolved in this study.

The models suggest there has been no major heating events since the Late Cretaceous, and is indicative of how little erosion has occurred since that time. The dataset would exhibit younger cooling ages if there was a higher rate of (or more) erosion. Dusel-Bacon et al. (2016) suggested that 2 km of erosion has occurred in the Yukon-Tanana Uplands, near the US-Canada border, in

the Eocene. Based on our models, that seems unlikely as the data do not illustrate any Eocene events of that magnitude. The differences in thermal histories is unlikely related to topographic evolution, as over the last 100 million years there were relatively low incision rates (Ryan et al., 2017), which allowed for the preservation of middle Cretaceous to Paleocene units. There is no indication that the middle Cretaceous and Paleocene units were thick enough to undergo 2 km of erosion and still have their unconformities preserved today. The present-day erosional surface is at a similar elevation to the ancient unconformities as further evidence that the Yukon exhibits a mature landscape (Ryan et al., 2017).

(U-Th)/He thermochronology from the Aishihik batholith indicates that the interior of the magmatic complex likely cooled slightly earlier than the margins, which is contrary to our understanding of the thermal diffusion in igneous bodies (e.g. Harrison and Clarke, 1979). The interior of the batholith possesses AHe ages of 123-93 Ma whereas AHe ages from the margins are 112-48 Ma and numerical models suggest that the interior may have cooled a few million years before the margins. Nevertheless, cooling rates of 15°C/m.y. as resolved by the models are all relatively consistent within in the Southeastern domain, and both the margins and center of the batholith would have still been at the surface to be unconformably overlain by the 100 Ma Mount Nansen volcanic sequence. The Aishihik batholith is a large lopolithic structure that is east-dipping and tapers to the west (Johnston and Erdmer, 1995). The lopolithic structure is generally a lenticular body with a central region that is thicker and may have acted as the feeder for the system. Lopoliths and similarly laccoliths are thought to exhibit a ballooning stage near the end of the intrusion cycle, but this solid-state phenomenon would have occurred when the rocks were still relatively warm, within error of the Jurassic U-Pb crystallization ages. It is difficult to resolve these cooling rates with the known structure and overall geology of the region.

5.2. Geological implications

As a consequence of widespread mineralization in the Late Jurassic (ca. 155 Ma; Joyce, 2002; Bailey, 2013; Mackenzie et al., 2014), southcentral Yukon is home to numerous mineral endowments (e.g. Minto, Klaza, Cyprus). The mineral deposits in the study area are porphyry to epithermal and seem to be associated to the Late Cretaceous Casino Suite (Hart and Langdon, 1998; Mortensen et al., 2016; Ryan et al., 2016). Casino Suite volcanic plugs and hypabyssal intrusions are located within the study area which could suggest potential mineralization (Ryan et al., 2016). With this insight, the numerical models were allowed to capture this Late Cretaceous thermal event in the (U-Th)/He data to test the possibility of (re)heating due to the mineralization. Within all three of the domains, no significant thermal event as evinced by a change in magnitude or rate of heating or cooling was implicit. The porphyry potential of the Long Lake Suite is not well understood, despite possessing hypabyssal phases within the suite which suggests that the crustal depth is suitable for porphyry mineralization (Ryan et al., 2016). The elevated temperatures in the Northwestern and Southeastern domains are too high to record a thermal pulse at this time with our dataset. However, the Central domain records a cooling rate change from 7°C/m.y. to 2°C/m.y (**Figure 14**). The significance of this change is equivocal, but the coincidence with the timing of regional mineralization is curious.

The Aishihik batholith's cooling history did follow the general cooling patterns of continental arc batholiths when it cooled (**Figure 15**). Intrusions may stay warm (>300°C) for an extended period of time after emplacement, and some batholiths in the Cordillera remained deep and warm for up to 60 m.y. after crystallization (e.g. Fayon et al., 2017). Within the scale of the YTT, the Aishihik batholith began cooling and probably exhuming immediately after its emplacement during the subduction of the Panthalassa Ocean, which is a common phenomenon

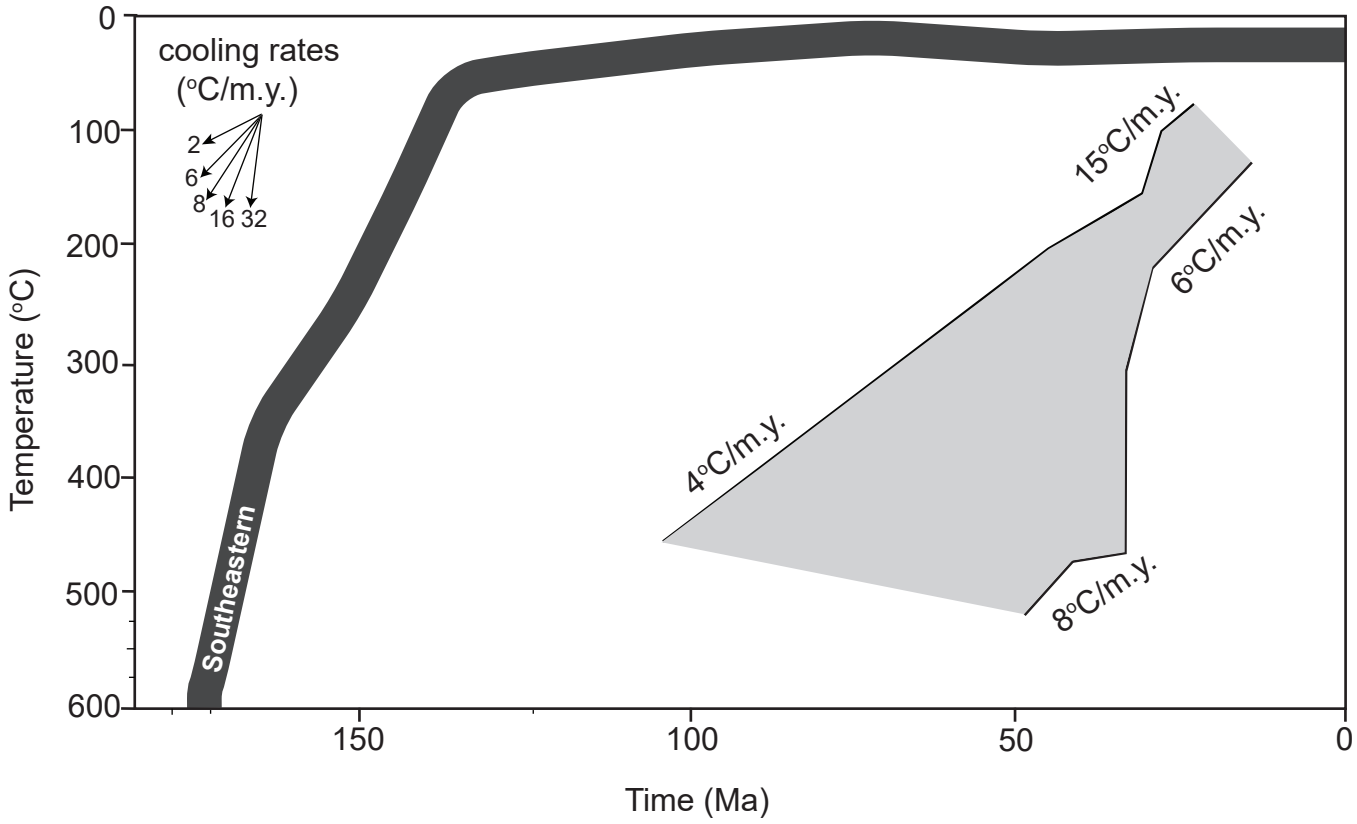

Figure 15: Summary of tectonothermal history of the southeastern domain compared to other continental arc batholiths. The diagram is focused on the low temperature cooling history and only illustrates the thermal history of the samples from 600°C and lower. t-T pathway of the southeastern domain represents the line of best fit of from figure 13. The light grey envelope (independent of time) illustrates the range in t-T pathways from other continental arc batholiths (e.g. Fayon et. al, 2017; Dai et. al, 2013; Adriasola et. al, 2005; Krol and Zeitler, 1996). See text for discussion.

for batholiths within continental arc settings (e.g. Dai et al., 2013). The Aishihik batholith cooled very rapidly until it reached the upper crust (ca. 130 Ma) which is when the rate of cooling dropped and the batholith slowly made its way to the surface. Generally, only intrusions within the upper 10 km of the crust exhibit an initial stage of rapid cooling after emplacement and subsequent slower cooling rates at lower temperatures (e.g. Adriasola et al., 2005). The Aishihik batholith is set to have been emplaced at a depth of 12-15 km (Topham, 2015), so it would have been originally thought to exhibit a moderate and steady cooling rate. The increased rate of cooling could have been explained by a thrust fault along the edge of the batholith that was active coeval with, or shortly following batholith emplacement. Unfortunately, the proposed structural discontinuity (Johnston, 1993; Johnston and Ermder, 1995) along the northwestern margin of the batholith was proven false. Recent mapping (Ryan et al., 2016) indicates that the northwestern margin of the Aishihik batholith is in fact an intrusive contact, and no evidence of a structural discontinuity was found. If there was a large scale structural discontinuity, it would be evident within the thermal models as either side of the fault may have exhibited different cooling histories. The geometry of the batholith would allow for the prediction that diverse cooling histories would be seen across the area (e.g. Fayon et al., 2017), however we are unable to resolve any such noticeable variation. There is still much to learn of the thermal history of these bodies once crystallization has stopped. Depth of emplacement, temperature of country rock, cause of exhumation and shape of the body are all factors that need to be heavily considered in a thermal history interpretation of a batholith.

From the dataset and numerical models, we are able to interpolate the low-temperature tectonic history of the Aishihik region during the Cretaceous period. Regionally speaking, cooling in the Jurassic likely occurred from extension during slab rollback leading to unroofing (Berman et al., 2007; Knight et al., 2013; Staples et al., 2013; Dusel-Bacon et al., 2015), however cooling

within the Cretaceous period occurred from contraction which led to crustal thickening and uplift. Within the Cretaceous (**Figure 14**, panel B), in the Northwestern domain all three of the samples show cooling rates between 4-5°C/m.y. The five samples in the Central domain exhibit cooling rates between 1.5-3.5°C/m.y, and seven of the samples in the Southeastern domain (excluding samples 15RAY-MM003A01 and 15RAY-JR081A03) also show cooling rates between 1.5-3.5°C/m.y. When evaluating the models from the middle to Early Cretaceous (ca. 100-70 Ma) there is a noticeable increase in cooling rates compared to the overall Cretaceous cooling rates in nine out of the sixteen samples. Rates increased between 2.5 to 10°C/m.y within those 30 m.y compared to the overall rate during the Cretaceous. The mechanism of the Cretaceous cooling is unknown, but the dataset provide geologic constraints for other studies looking into the Cretaceous or post-Cretaceous events.

6. Conclusions

(U-Th)/He thermochronologic studies are relatively new and these developing techniques face some challenges and limitations. Although the data can have a significant impact on helping resolve the timing of upper crustal / near surface deformation, large thermochronologic data sets are required to determine the distribution and timing of faulting or extension (Stockli, 2005). Combined datasets using several mineral systematics can allow for the thermal history to be more comprehensive. The accuracy of these studies is also limited by the how well the (paleo) geothermal gradient has been temporally and spatially modelled. Thus, it is useful if independent geologic constraints are available, which are required to create plausible thermal histories (Spotila, 2005). Despite the challenges, the (U-Th)/He data presented in this thesis significantly adds to our

network of thermochronologic data within the Yukon, and improves our understanding of shallow crustal processes and the nature batholith cooling.

An extensive data set of thermochronological ages presented here illuminate the Jurassic-Cretaceous tectonothermal history of south-central Yukon Cordillera. Early Jurassic and Late Cretaceous cooling ages across the study area suggest widespread regional cooling and exhumation. The YTT host rocks exhibited steady cooling of ~5°C/m.y from the Early Jurassic to the Late Cretaceous, when it reached the surface. Regions closer the Aishihik batholith displayed a relatively quicker cooling rate of 7°C/m.y from the Early Jurassic to the Late Jurassic and then slowed down to 1.5°C/m.y from the Early Cretaceous until it reached the surface in the Late Cretaceous. The batholith itself exhibits relatively fast cooling from the Early Jurassic to Late Jurassic (15°C/m.y) and then it slowed down considerably in the Early Cretaceous (1.5°C/m.y) until it reached surface conditions in the Late Cretaceous. Rocks were at the surface at the latest by the Late Cretaceous and show no indication that there were any significant thermal events after such time. This confirms the proposal of Ryan et al. (2017) suggesting that the Yukon has an old landscape compared to the Cordillera in Alaska and British Columbia. The geometry and mechanics of a batholith play an important role in interpreting its thermal history. Recent mapping suggests that the northwestern margin of the Aishihik batholith is an intrusive contact, which has implications for the level of crust that is preserved since Jurassic time. The dataset is relevant to some of the various mineral endowments that are located across the Yukon Cordillera, as most of the mineralization is Cretaceous in age. Having a better understanding of low-temperature Cretaceous tectonism can potentially lead to the exploration and discovery of new deposits.

References

Adriasola, A.C., Thomson, S.N., Brix, M.R., Hervé, F. and Stöckhert, B. (2005) Postmagmatic cooling and late Cenozoic denudation of the North Patagonian Batholith in the Los Lagos region of Chile, 41°-42°15'S. International Journal of Earth Sciences, v. 95, p. 504-528.

Bailey, L.A. (2013) Late Jurassic fault-hosted gold mineralization of the Golden Saddle Deposit, White Gold District, Yukon Territory. MSc University of British Columbia.

Berman, R.G., Ryan, J.J., Gordey, S.P. and Villeneuve, M. (2007) Permian to Cretaceous polymetamorphic evolution of the Stewart River region, Yukon-Tanana terrane, Yukon, Canada: P-T evolution linked with in situ SHRIMP monazite geochronology. Journal of Metamorphic Geology, v. 25, p. 803–287.

Braun, J. (2002) Estimating exhumation rate and relief evolution by spectral analysis of age-elevation datasets. Terra Nova, v. 14, p. 210-214.

Chew, D.M. and Spikings, R.A. (2015) Geochronology and thermochronology using apatite: Time and temperature, lower crust to surface. Elements, v. 11(3), p. 189-194.

Clark, A.D. (2017) Tectonothermal history of mid-crustal rocks at Aishihik Lake, southwest Yukon. MSc Simon Fraser University.

Colpron, M., Nelson, J.L. and Murphy, D.C. (2006) A tectonostratigraphic framework for the Pericratonic terranes of the northern Canadian Cordillera. Special Paper – Geological Association of Canada, v. 45, p. 1-23.

Colpron, M., Nelson, J.L. and Murphy, D.L. (2007) Northern Cordilleran terranes and their interactions through time. Geological Society of America Today, v. 17, p. 4-10.

Colpron, M. and Nelson, J.L. (2011) A digital atlas of terranes for the Northern Cordillera (1 : 5 000 000 scale). Yukon Geological Survey.

Dai, J., Wang, C., Hourigan, J., Li, Z. and Zhuang, G. (2013) Exhumation history of the Gangdese Batholith, Southern Tibetan Plateau: evidence from apatite and zircon (U-Th)/He thermochronology. Journal of Geology, v. 121, p. 155-172.

Dodson, M.H. (1973) Closure temperature in cooling geochronological and petrological systems. Contributions to Mineralogy and Petrology, v. 40, p. 259-274.

Dusel-Bacon, C., Aleinikoff, J.N., Day, W.C. and Mortensen, J.K. (2015) Mesozoic magmatism and timing of epigenetic Pb-Zn-Ag mineralization in the western Fortymile mining district, east-central Alaska: Zircon U-Pb geochronology, whole-rock geochemistry, and Pb isotopes. Geosphere, v. 11, p. 1-37.

Dusel-Bacon, C., Bacon, C.R., O'Sullivan, P.B. and Day, W.C. (2016) Apatite fission track evidence for regional exhumation in the subtropical Eocene, block faulting, and localized fluid flow in east-central Alaska. Canadian Journal of Earth Sciences, v. 280, p. 260-280.

Fayon, A.K., Tikoff, B., Kahn, M. and Gaschnig, R.M. (2017) Cooling and exhumation of the southern Idaho batholith. Lithosphere, v. 9, p. 299-314.

Flowers, R.M., Ketcham, R.A., Shuster, D.L. and Farley, K.A. (2009) Apatite (U-Th)/He thermochronometry using a radiation damage accumulation and annealing model. Geochimica et Cosmochimica Acta, v. 73, p. 2347-2365.

Gehrels, G.E., and 15 others (2009) U-Th-Pb geochronology of the Coast Mountains Batholith in north-coastal British Columbia: constraints on age, petrogenesis, and tectonic evolution. Geological Society of America Bulletin, v. 121, p. 1341-1361.

Guenthner, W.R., Reiners, P.W., Ketcham, R.A., Nasdala, L. and Geister, G. (2013) Helium diffusion in natural zircon: radiation damage, anisotropy, and the interpretation of zircon (U-Th)/He thermochronology. American Journal of Science, v. 313, p. 145-198.

Guenthner, W.R., Reiners, P.W. and Tian, Y. (2014) Interpreting date–eU correlations in zircon (U-Th)/He datasets: a case study from the Longmen Shan, China. Earth and Planetary Science Letters, v. 403, p. 328-339.

Harrison, T.M., Armstrong, R., Naeser, C. and Harakal, J. (1979) Geochronology and thermal history of the Coast Plutonic Complex, near Prince Rupert, British Columbia. Canadian Journal of Earth Sciences, v. 16, p. 400-410.

Harrison, T.M. and Clarke, G.K.C. (1979) A model of the thermal effects of igneous intrusion and uplift as applied to Quoottoon pluton, British Columbia. Canadian Journal of Earth Sciences, v. 16, p. 411-420.

Harrison, T.M. and Zeitler, P.K. (2005) Fundamentals of noble gas thermochronology. Reviews in Mineralogy and Geochemistry, v. 58, p. 123-149.

Hart, C.J.R. and Langdon, M. (1998) Geology and mineral deposits of Mount Nansen camp, Yukon. In: Yukon Exploration and Geology (1997), Exploration and Geological Services Division, Yukon Region, Indian and Northern Affairs Canada, p. 129-138.

Hurley, P.M. (1954) The helium age method and the distribution and migration of helium in rocks. In: Nuclear Geology. Faul, H. (Ed.), Wiley & Sons, p. 301-329.

Johnston, S.T. (1993) The geological evolution of Nisling Assemblage and Stikine Terrane in the Aishihik Lake Area, southwest Yukon, In: University of Alberta, D.o.G. (Ed.), Edmonton.

Johnston, S.T. and Erdmer, P. (1995) Magmatic flow and emplacement foliations in the early Jurassic Aishihik Batholith, southwest Yukon: implications for northern Stikina, In: Miller, D. M., Busby, C. (Ed.), Jurassic magmatism and tectonics of the Northern American Cordillera. Special Paper - Geological Society of America, p. 65-82.

Johnston, S.T., Mortensen, J.K. and Erdmer, P. (1996) Igneous and metaigneous age constraints for the Aishihik metamorphic suite, southwest Yukon. Canadian Journal of Earth Sciences, v. 33, p. 1543-1555.

Joyce, N.L. (2002) Geological setting, nature, and structural evolution of intrusion-hosted Au bearing quartz veins at the Longline occurrence, Moosehorn Range area, west-central Yukon Territory. MSc University of British Columbia.

Joyce, N.L., Ryan, J.J., Colpron, M., Hart, C.J.R. and Murphy, D.C. (2015) A compilation of $^{40}Ar/^{39}Ar$ age determinations for igneous and metamorphic rocks, and mineral occurances from central and southeastern Yukon. Geological Survey of Canada, open file 7924.

Joyce, N.L., Colpron, M., Allan, M.M., Sack, P.J., Crowley, J.L. and Chapman, J.B. (2016) New U-Pb zircon dates from the Aishihik batholith, southern Yukon. Yukon Geological Survey, p. 131-149.

Ketcham, R.A. (2005) Forward and inverse modeling of low-temperature thermochronometry data. Mineralogical Society of America, v. 58, p. 275-314.

Ketcham, R.A. (2012). Basin thermal history analysis using (U-Th)/He thermochronology, In: Analyzing the thermal history of sedimentary basins: methods and case studies. Society for Sedimentary Geology, v. 103, p. 105-123.

Koons, P., Zeitler, P. and Hallet, B. (2013) Tectonic Aneurysms and Mountain Building. Treatise on Geomorphology, v. 5, p. 318-349.

Knight, E., Schneider, D.A. and Ryan, J. (2013) Thermochronology of the Yukon-Tanana terrane, west-central Yukon: evidence for Jurassic extension and exhumation in the northern Canadian Cordillera. Journal of Geology, v. 121, p. 371-400.

Krol, M.A., Zeitler, P.K. and Copeland, P. (1996) Episodic unroofing of the Kohistan Batholith, Pakistan: implications from K-feldspar thermochronology. Journal of Geophysical Research, v. 101, p. 28149-28164.

Larsen, E.S. (1945) Time required for the crystallization of the great batholith of southern and lower California. American Journal of Science, v. 243, p. 399-416.

Lovering, T.S. (1935) Theory of heat conduction applied to geological problems. Bulletin of the Geological Society of America, v. 46, p. 69-94.

MacKenzie, D., Craw, D. and Finnigan, C. (2014) Structural controls on alteration and mineralization at the Coffee gold deposits, Yukon. In: Yukon Exploration and Geology (2013) MacFarlane, K.E., Nordling, M.G. and Sack, P.J. (Ed.), Yukon Geological Survey, p. 119-131.

Monger, J.W.H., Souther, J.G. and Gabrielse, H. (1972) Evolution of the Canadian Cordillera: a plate-tectonic model. American Journal of Science, v. 272, p. 577-602.

Morneau, Y.E. (2017) Tectono-Metamorphic evolution of the Snowcap Assemblage, Yukon-Tanana terrane, west-central Yukon. MSc Carleton University.

Mortensen, J.K (1990) Geology and U-Pb geochronology of the Klondike District, west-central Yukon Territory. Canadian Journal of Earth Sciences, v. 27, p. 903-914.

Mortensen, J.K. (1992) Pre-mid Mesozoic tectonic evolution of the Yukon-Tanana terrane, Yukon and Alaska. Tectonics, v. 11, p. 836-853.

Mortensen, J.K., Hart, C.J.R., Tarswell, J. and Allan, M.M. (2016) U-Pb zircon age and Pb isotopic constraints on the age and origin of porphyry and epithermal vein mineralization in the eastern Dawson Range, Yukon. In: Yukon Exploration Geology (2015) MacFarlane, K.E. and Nordling, M.G. (Ed.), Yukon Geological Survey, p. 165-185.

Murray, K.E., Orme, D.A. and Reiners, P.W. (2014) Effects of U-Th-rich grain boundary phases on apatite helium ages. Chemical Geology, v. 390, p. 135-151.

Murphy, D.C., Mortensen, J.K., Piercey, S.J., Orchard, M.J. and Gehrels, G.E. (2006) Mid-Paleozoic to early Mesozoic tectonostratigraphic evolution of Yukon-Tanana and Slide Mountain terranes and affiliated overlap assemblages, Finlayson Lake massive sulphide district, southeastern Yukon. Special Paper – Geological Association of Canada, v. 45, p. 75-105.

Nelson, J.L., Colpron, M., Piercey, S.J., Dusel-Bacon, C., Murphy, D.C. and Roots, C.F. (2006) Paleozoic tectonic and metallogenic evolution of pericratonic terranes in Yukon, northern British Columbia and eastern Alaska. Special Paper – Geological Association of Canada, v. 45, p. 323-360.

Nelson, J.L. and Gehrels G. (2007) Detrital zircon geochronology and provenance of the southeastern Yukon-Tanana terrane. Canadian Journal of Earth Sciences, v. 44, p. 297-316.

Nelson, J.L., Colpron, M. and Israel, S. (2013) The cordillera of British Columbia, Yukon and Alaska: tectonics and metallogeny. Tectonics, metallogeny and discovery: the North American Cordillera and similar accretionary settings. (Ed.), Colpron, M., Bissig, T., Rusk, B.G. and Thompson, J. Special Paper - Society of Economic Geologists, v. 17, p. 53-110.

Ortega-Rivera, A. (2003) Geochronological constraints on the tectonic history of the Peninsular Ranges Batholith of Alta and Baja California: tectonic implications for western Mexico. Special Paper – Geological Society of America, v. 374, p. 297-335.

Paterson, S.R. and Fowler Jr., T.K. (1993) Re-examining pluton emplacement processes. Journal of Structural Geology, v. 15, p. 191-206.

Piercey, S.J. and Colpron, M. (2005) Composition and provenance of the Snowcap assemblage, basement to the Yukon-Tanana terrane, northern Cordillera: implications for Cordillera crustal growth. Geosphere, v. 5, p. 439-464.

Reiners, P.W., Farley, K.A. and Hickes, H.J. (2002) He diffusion and (U-Th)/He thermochronometry of zircon: initial results from Fish Canyon Tuff and Gold Butte, Nevada. Tectonophysics, v. 349, p. 247-308.

Reiners, P.W., Spell, T.L., Nicolescu, S. and Zanetii, K.A. (2004) Zircon (U-Th)/ He thermochronology: He diffusion and comparison with $^{40}Ar/^{39}Ar$ dating. Geochimica et Cosmochimica Acta, v. 68, p. 1857-1887.

Reiners, P.W. and Brandon, M.T. (2006) Using thermochronology to understand orogenic erosion. Annual Review of Earth and Planetary Sciences, v. 34, p. 419-466.

Ryan, J.J., Zagorevski, A., Roots, C.F. and Joyce, N. (2014) Paleozoic tectonostratigraphy of the northern Stevenson Ridge area, Yukon. Geological Survey of Canada, current research 2014-4.

Ryan, J.J., Westberg, E.E., Williams, S.P. and Chapman J.B. (2016) Geology, Mount Nansen Nisling River Area, Yukon. Geological Survey of Canada, Canadian Geoscience Map 292 (preliminary), scale 1:100 000.

Ryan, J.J., Hayward, N. and Jackson, L.E. (2017) Landscape antiquity and Cenozoic drainage development of southern Yukon, through restoration modelling of the Tintina fault. Canadian Journal of Earth Sciences, v. 54, p. 1085-1100.

Rutherford, E. (1905) Present problems in radioactivity. The Popular Science Monthly, p. 1-34.

Spiegel, C., Kohn, B., Belton, D., Berner, Z. and Gleadow, A. (2009) Apatite (U-Th-Sm)/He thermochronology of rapidly cooled samples: the effect of He implantation. Earth and Planetary Science Letters, v. 285, p. 105-114.

Spotila, J.A. (2005) Applications of low-temperature thermochronometery to quantification of recent exhumation in mountain belts. Reviews in Mineralogy and Geochemistry, v. 58, p. 449-466.

Staples, R.D., Gibson, H.D., Berman, R.G., Ryan, J.J. and Colpron, M. (2013) A window into the Early to mid-Cretaceous infrastructure of the Yukon-Tanana terrane recorded in multi-stage garnet of west central Yukon, Canada. Journal of Metamorphic Geology, v. 31, p. 729-753.

Staples, R.D., Gibson, H.D., Colpron, M. and Ryan, J.J. (2016) An orogenic wedge model for diachronous deformation, metamorphism, and exhumation in the hinterland of the northern Canadian Cordillera. Lithosphere, v. 8, p. 165-184.

Stockli, D.F. (2005) Application of low-temperature thermochronology to extensional tectonic settings. Reviews in Mineralogy & Geochemistry, v. 58, p. 411-448.

Tempelman-Kluit, D. (1974) Reconnaissance geology of Aishihik Lake, Snag and Part of Stewart River Map-areas, West central Yukon (115A, 115F, 115G and 115K). Department of Energy, Mines and Resources.

Tempelman-Kluit, D. and Wanless, R. (1975) Potassium-argon age determinations of metamorphic and plutonic rocks in the Yukon Crystalline Terrane. Canadian Journal of Earth Sciences, v. 12, p. 1895-1909.

Tempelman-Kluit, D.J. (1980) Evolution of physiography and drainage in southern Yukon. Canadian Journal of Earth Sciences, v. 17, p. 1189-1203.

Topham, M.J. (2015). Emplacement depth and porphyry copper-gold potential of Late Triassic to Early Jurassic granitoids in Yukon. BSc University of British Columbia.

Wolfe, M.R. and Stockli, D.F. (2010) Zircon (U-Th)/He thermochronology in the KTB drill hole, Germany and its implications for bulk He diffusion kinetics in zircon. Earth and Planetary Science Letters, v. 295, p. 69-82.

Zagorevski, A., Mihalynuk, M.G., Joyce, N. and Martin, K. (2014) Characterization of volcanic and intrusive rocks across the British Columbia – Yukon border GEM 2 Cordillera. Geological Survey of Canada, open file 7697.

Zeitler, P.K., Herczeg, A.L., McDougall, I. and Honda, M. (1987) U-Th-He dating of apatite: a potential thermochronometers. Geochimica et Cosmochimica Acta, v. 51, p. 2865-2868.

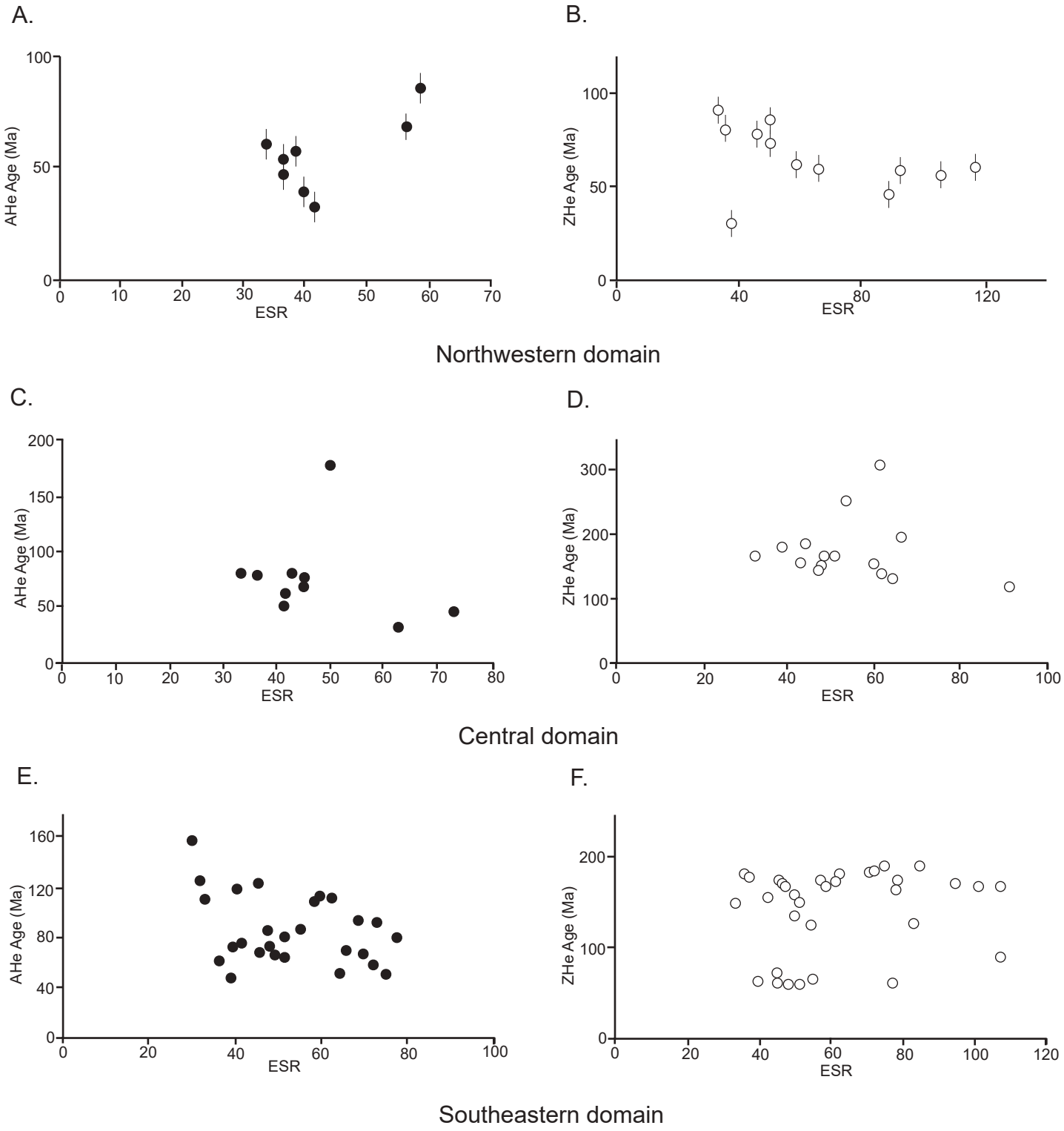

Figure 1 DR: AHe/ESR and ZHe/ESR (equivalent spherical radius) graphs for each of the three domains. Grains that are considered outliers (* in the tables 1a, 1b, 1c) are not included in the plots. Plots that seem to not have any error bars is due to the error bars being smaller than the markers. **A**: AHe/ESR for the northwestern domain. **B**: ZHe/ESR for the northwestern domain. **C**: AHe/ESR for the central domain. **D**: ZHe/ESR for the central domain. **E**: AHe/ESR for the southeastern domain. **F**: ZHe/ESR for the southeastern domain.

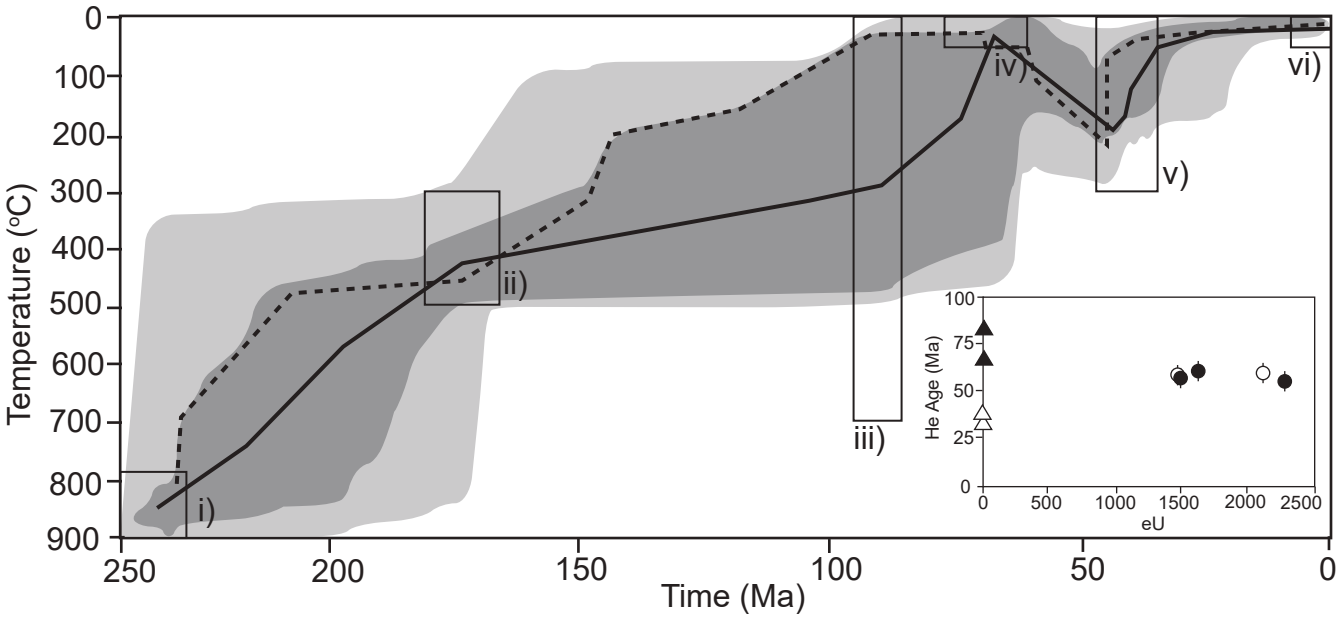

Figure 2 DR: Northwestern domain: Inverse model for sample 15RAY-JC095A03. 3 zircon grains (61.4 ± 4.4 Ma to 55.8 ± 4.0 Ma) and 2 apatite grains (58.8 ± 4.1 Ma to 52.1 ± 3.7 Ma) were used to create the model. The constraint boxes include: i) crystallization ages, ii) HAr/ BtAr dates, iii) Mount Nansen unconformity, iv) Carmacks unconformity, v) potential Eocene event, and vi) surface. Dark grey envelopes represent t-T pathways with a 'good fit' and light grey envelopes represent t-T pathways with an 'acceptable fit'. The thick black line represents the weighted mean path of the sample and the dashed line represents the line of best fit. The He age-eU plot in the bottom right corner illustrates apatite (triangles) and zircon (circles) grains from this sample that were used to make the inverse model. Filled symbols indicate that the grain was used in the model, while unfilled symbols denote grains that were not used.

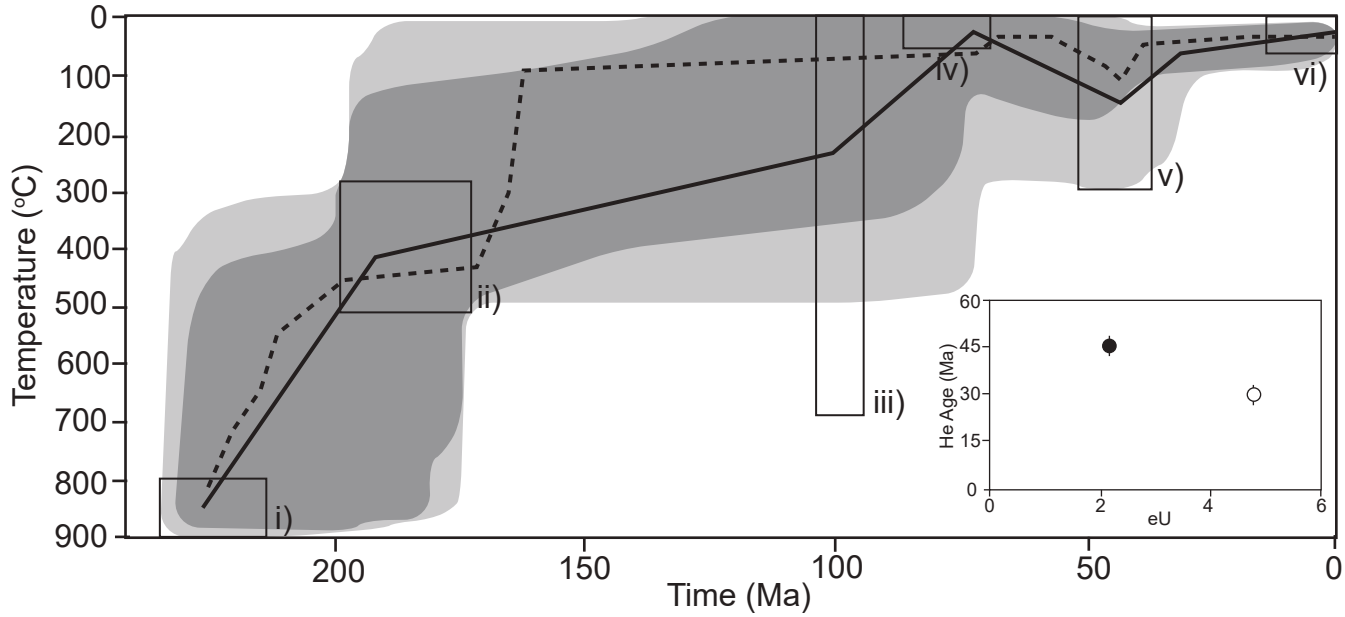

Figure 3 DR: Northwestern domain: Inverse model for sample 15RAY-MM055A01. 1 zircon (45.8 ± 3.5 Ma) was used to create the model. The constraint boxes include: i) crystallization ages, ii) HAr/ BtAr dates, iii) Mount Nansen unconformity, iv) Carmacks unconformity, v) potential Eocene event, and vi) surface. Dark grey envelopes represent t-T pathways with a 'good fit' and light grey envelopes represent t-T pathways with an 'acceptable fit'. The thick black line represents the weighted mean path of the sample and the dashed line represents the line of best fit. The He age-eU plot in the bottom right corner illustrates zircon (circles) grains from this sample that were used to make the inverse model. Filled symbols indicate that the grain was used in the model, while unfilled symbols denote grains that were not used.

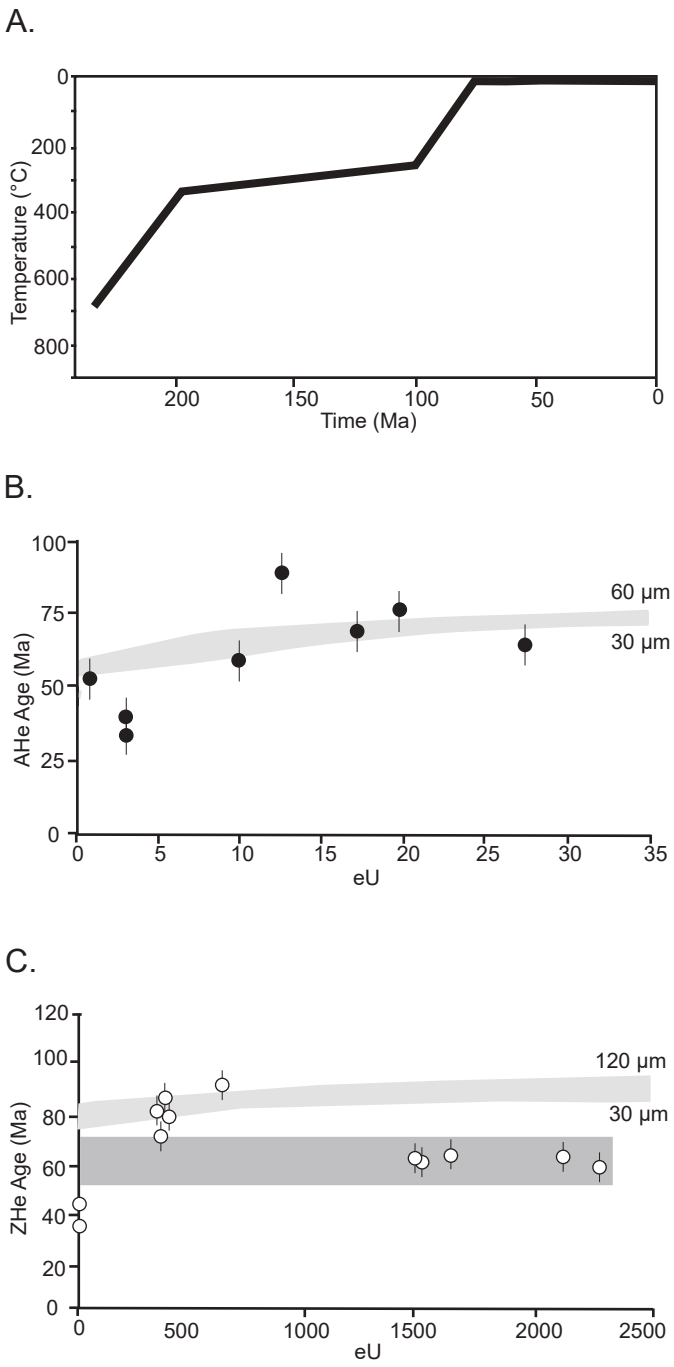

Figure 4 DR: Northwestern domain. **A**: Representative forward model of the Northwestern domain which does not demonstrate a plausible t-T path. The t-T pathway is derived from a earlier inverse model for sample 15RAY-MM035A01 that did not illustrate a plausible thermal path. **B**: Single crystal (U-Th)/He apatite cooling ages from the Northwestern domain plotted against eU. **C**: Single crystal (U-Th)/He zircon cooling ages from the Northwestern domain plotted against eU. The light grey polygon represents the range in grain size found in the Northwestern domain in apatite and zircon. The five grains outside of the ZHe envelope are all from one sample (15RAY-JC095A03), which is different from the rest of the domain in the case that it is the only sample which exhibits an Eocene cooling event (dark grey polgon).

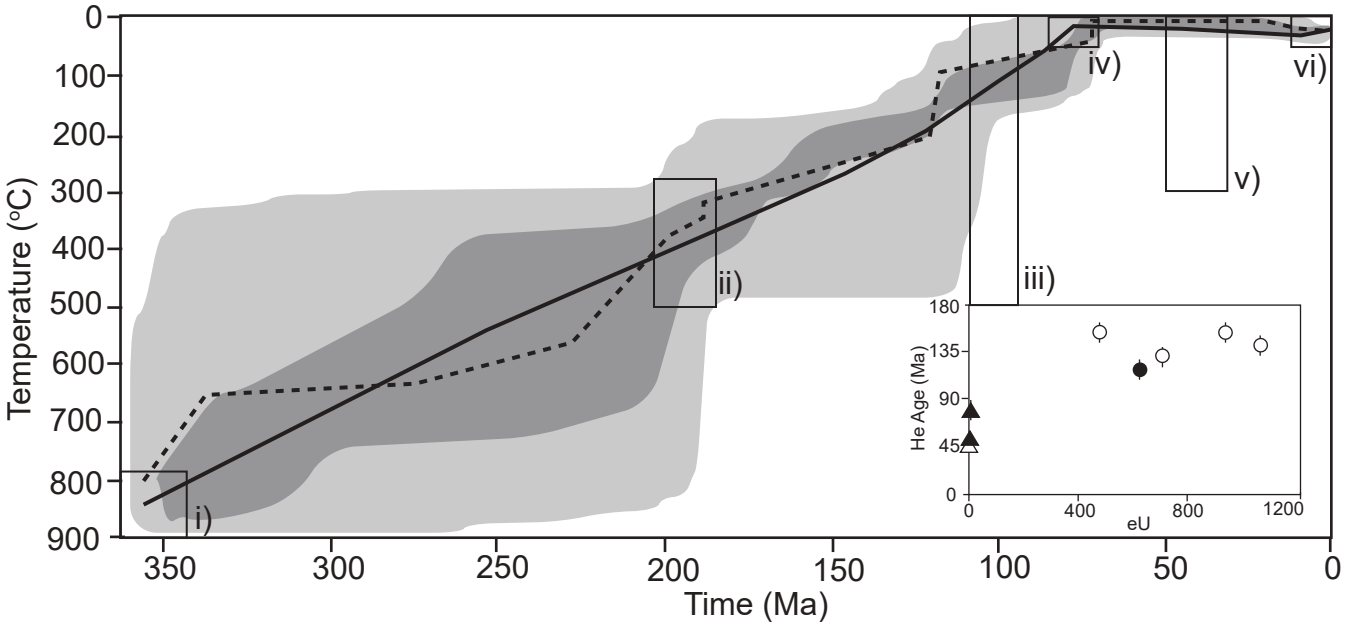

Figure 5 DR: Central domain: Inverse model for sample 15RAY-JR159A01. 1 zircon (118.3 ± 8.3 Ma) and 2 apatite grains (78.7 ± 7.6 Ma to 50.6 ± 4.3) were used to create the model. The constraint boxes include: i) crystallization ages, ii) HAr/ BtAr dates, iii) Mount Nansen unconformity, iv) Carmacks unconformity, v) potential Eocene event, and vi) surface. Dark grey envelopes represent t-T pathways with a 'good fit' and light grey envelopes represent t-T pathways with an 'acceptable fit'. The thick black line represents the weighted mean path of the sample and the dashed line represents the line of best fit. The He age-eU plot in the bottom right corner illustrates apatite (triangles) and zircon (circles) grains from this sample that were used to make the inverse model. Filled symbols indicate that the grain was used in the model, while unfilled symbols denote grains that were not used.

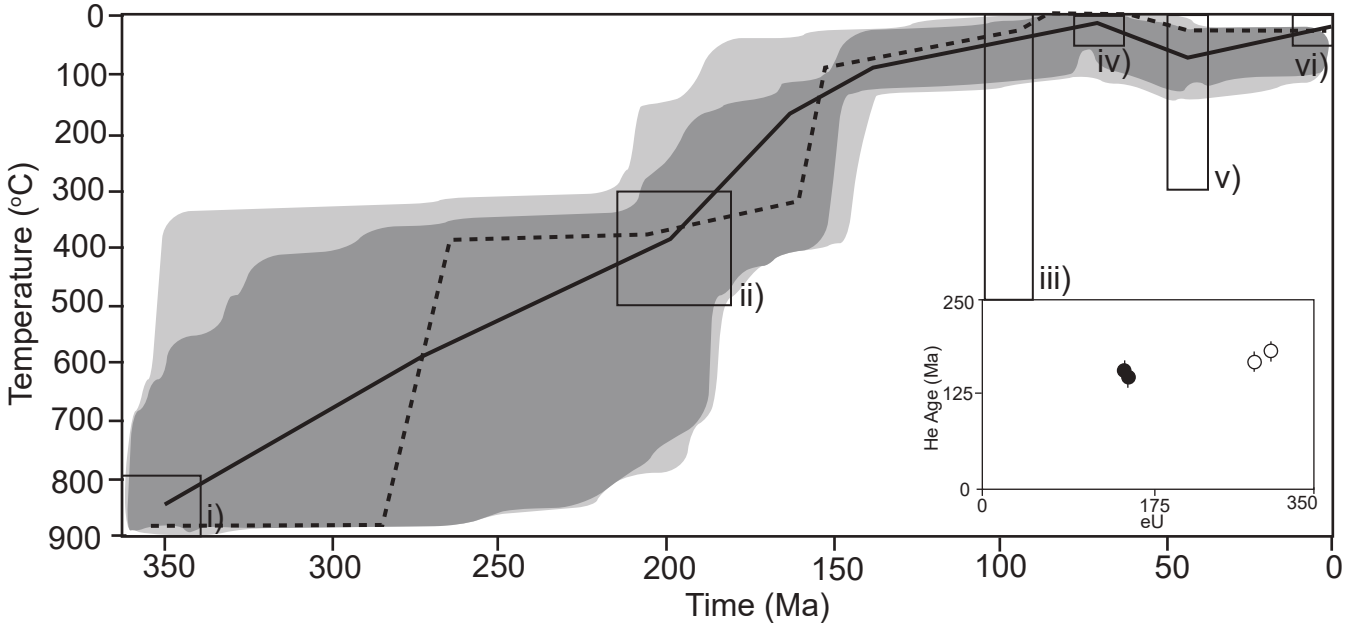

Figure 6 DR: Central domain: Inverse model for sample 15RAY-JR149A01. 2 zircon grains (156.8 ± 17.5 Ma to 145.7 ± 11.4 Ma) were used to create the model. The constraint boxes include: i) crystallization ages, ii) HAr/ BtAr dates, iii) Mount Nansen unconformity, iv) Carmacks unconformity, v) potential Eocene event, and vi) surface. Dark grey envelopes represent t-T pathways with a 'good fit' and light grey envelopes represent t-T pathways with an 'acceptable fit'. The thick black line represents the weighted mean path of the sample and the dashed line represents the line of best fit. The He age-eU plot in the bottom right corner illustrates zircon (circles) grains from this sample that were used to make the inverse model. Filled symbols indicate that the grain was used in the model, while unfilled symbols denote grains that were not used.

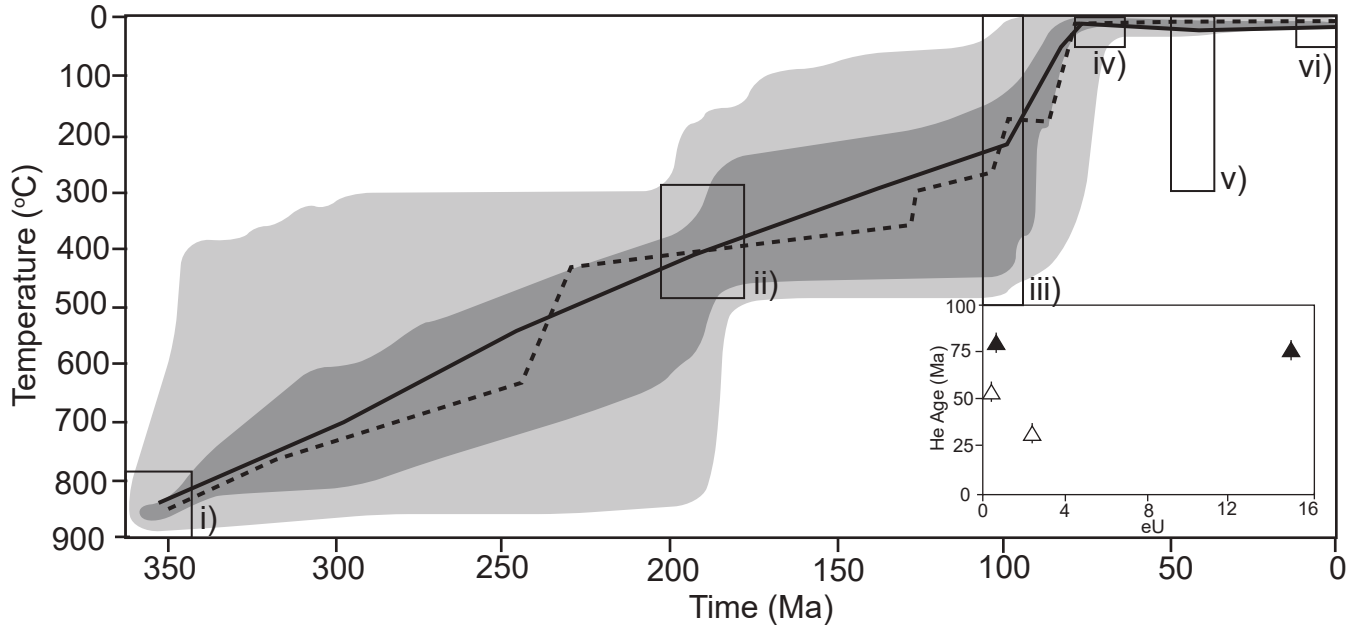

Figure 7 DR: Central domain: Inverse model for sample 15RAY-JR086A01. 2 apatite grains (80.8 ± 13.5 Ma to 76.5 ± 5.5 Ma) were used to create the model. The constraint boxes include: i) crystallization ages, ii) HAr/ BtAr dates, iii) Mount Nansen unconformity, iv) Carmacks unconformity, v) potential Eocene event, and vi) surface. Dark grey envelopes represent t-T pathways with a 'good fit' and light grey envelopes represent t-T pathways with an 'acceptable fit'. The thick black line represents the weighted mean path of the sample and the dashed line represents the line of best fit. The He age-eU plot in the bottom right corner illustrates apatite (triangles) grains from this sample that were used to make the inverse model. Filled symbols indicate that the grain was used in the model, while unfilled symbols denote grains that were not used.

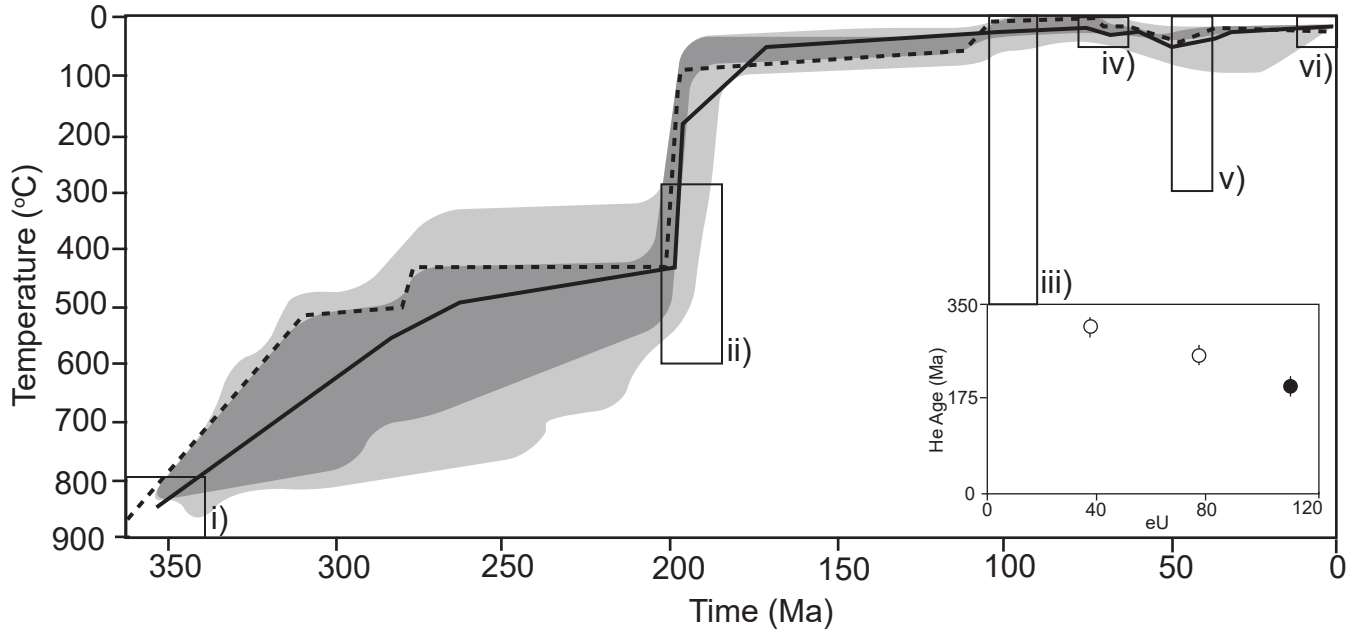

Figure 8 DR: Central domain: Inverse model for sample 15RAY-JR035A01. 1 zircon (198.0 ± 13.7 Ma) was used to create the model. The constraint boxes include: i) crystallization ages, ii) HAr/ BtAr dates, iii) Mount Nansen unconformity, iv) Carmacks unconformity, v) potential Eocene event, and vi) surface. Dark grey envelopes represent t-T pathways with a 'good fit' and light grey envelopes represent t-T pathways with an 'acceptable fit'. The thick black line represents the weighted mean path of the sample and the dashed line represents the line of best fit. The He age-eU plot in the bottom right corner illustrates zircon (circles) grains from this sample that were used to make the inverse model. Filled symbols indicate that the grain was used in the model, while unfilled symbols denote grains that were not used.

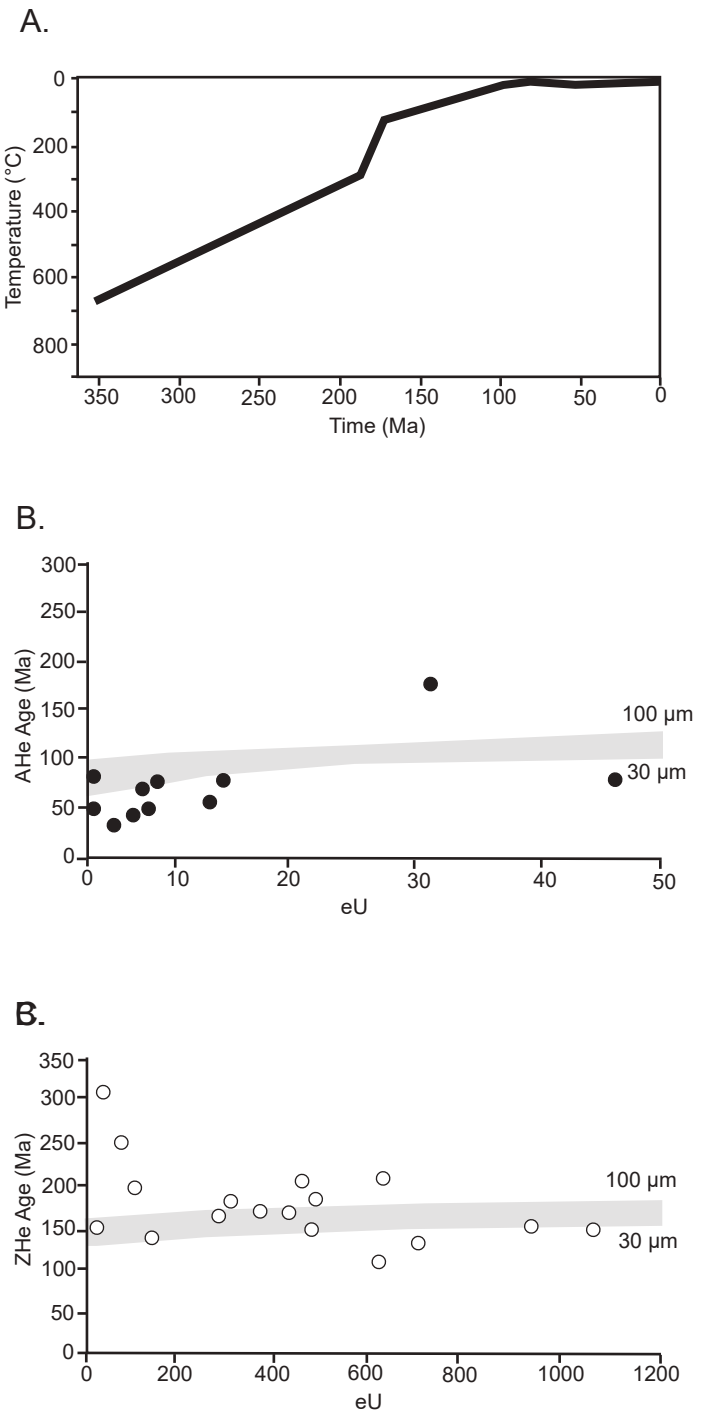

Figure 9 DR: Central domain. **A**: Representative forward model of the Central domain which does not demonstrate a plausible t-T path. The t-T pathway is derived from a earlier inverse model for sample 15RAY-MM063A01 that did not illustrate a plausible thermal path. **B**: Single crystal (U-Th)/He apatite cooling ages from the Central domain plotted against eU. The error bars on this graph are smaller than the plotted points. Grey polygon represents the range in grain size found in the central domain. **C**: Single crystal (U-Th)/He zircon cooling ages from the Central domain plotted against eU. The error bars on this graph are smaller than the plotted points. Grey polygon represents the range in grain size found in apatite and zircon the Central domain. Three zircon grains (all from sample 15RAY-JR035A01) have low eU – old ages and are not within the ZHe envelope, which can be explained from He implantation.

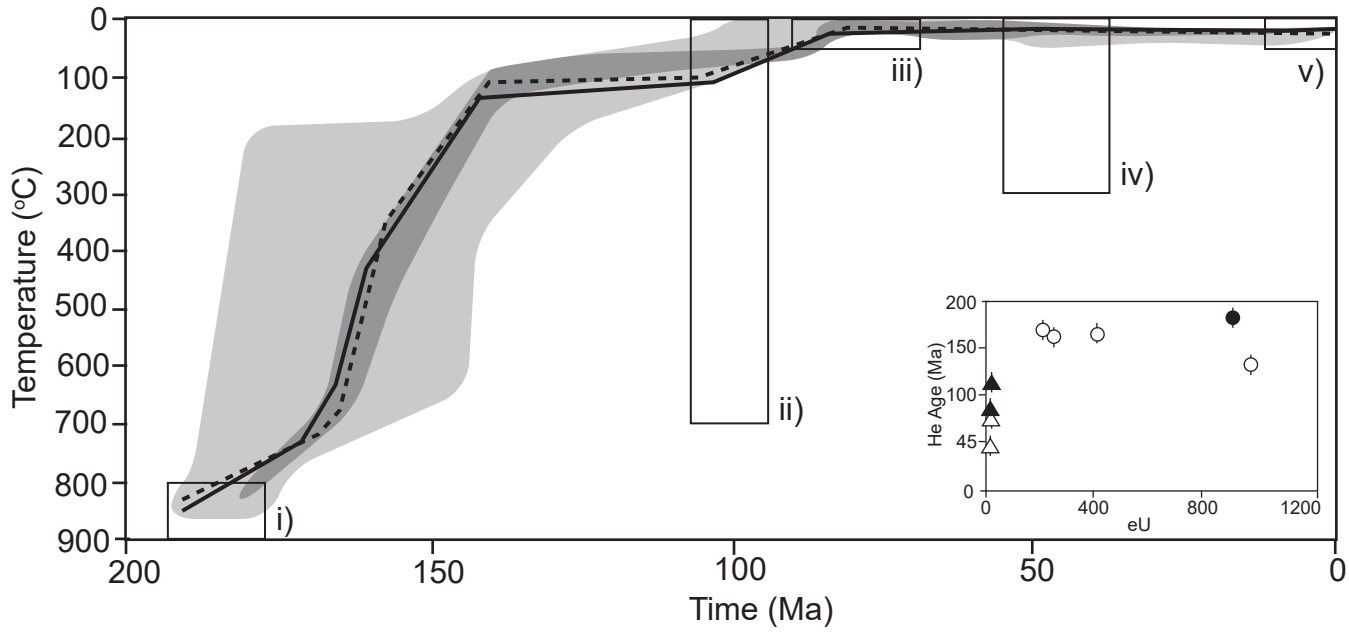

Figure 10 DR: Southeastern domain: Inverse model for sample 15RAY-JR029A02. 1 zircon (182.6 ± 13.0 Ma) and 2 apatite grains (112.8 ± 7.9 Ma to 86.2 ± 6.0 Ma) were used to create the model. The constraint boxes include: i) crystallization ages, ii) Mount Nansen unconformity, iii) Carmacks unconformity, iv) potential Eocene event, and v) surface. Dark grey envelopes represent t-T pathways with a 'good fit' and light grey envelopes represent t-T pathways with an 'acceptable fit'. The thick black line represents the weighted mean path of the sample and the dashed line represents the line of best fit. The He age-eU plot in the bottom right corner illustrates apatite (triangles) and zircon (circles) grains from this sample that were used to make the inverse model. Filled symbols indicate that the grain was used in the model, while unfilled symbols denote grains that were not used.

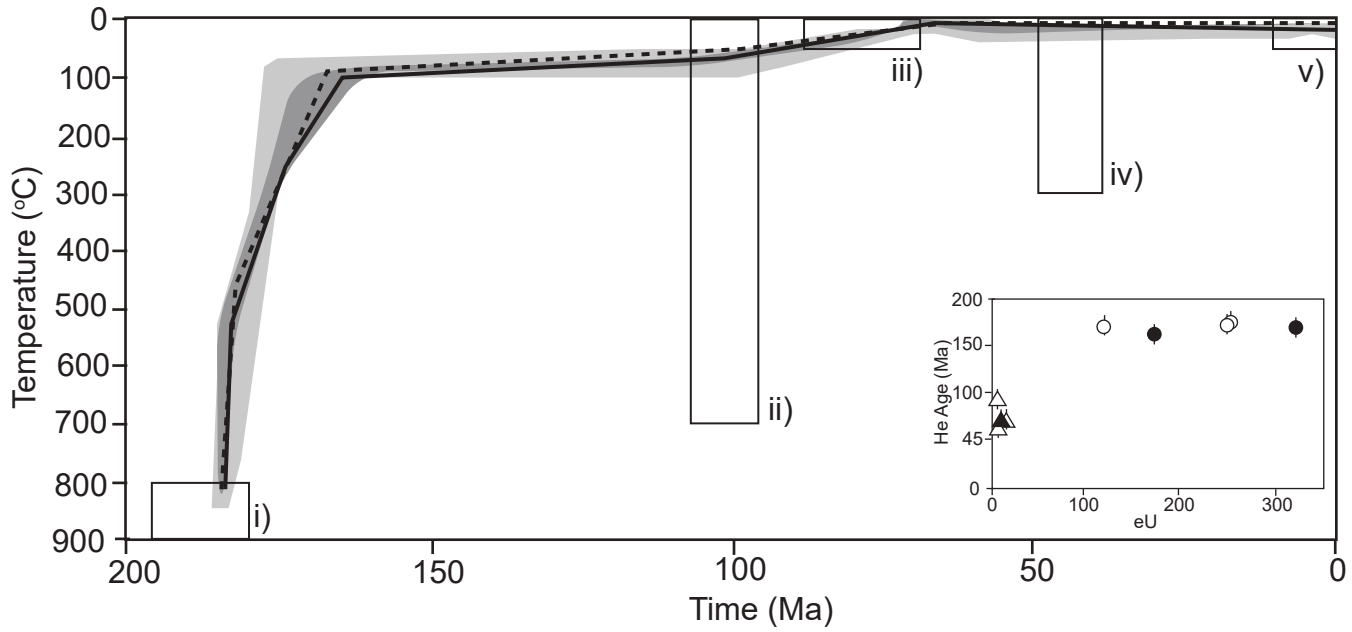

Figure 11 DR: Southeastern domain: Inverse model for sample 15RAY-MM007A01. 2 zircon grains (170.6 ± 20.8 Ma to 162.9 ± 11.7 Ma) and 1 apatite grain (73.7 ± 5.7 Ma) were used to create the model. The constraint boxes include: i) crystallization ages, ii) Mount Nansen unconformity, iii) Carmacks unconformity, iv) potential Eocene event, and v) surface. Dark grey envelopes represent t-T pathways with a 'good fit' and light grey envelopes represent t-T pathways with an 'acceptable fit'. The thick black line represents the weighted mean path of the sample and the dashed line represents the line of best fit. The He age-eU plot in the bottom right corner illustrates apatite (triangles) and zircon (circles) grains from this sample that were used to make the inverse model. Filled symbols indicate that the grain was used in the model, while unfilled symbols denote grains that were not used.

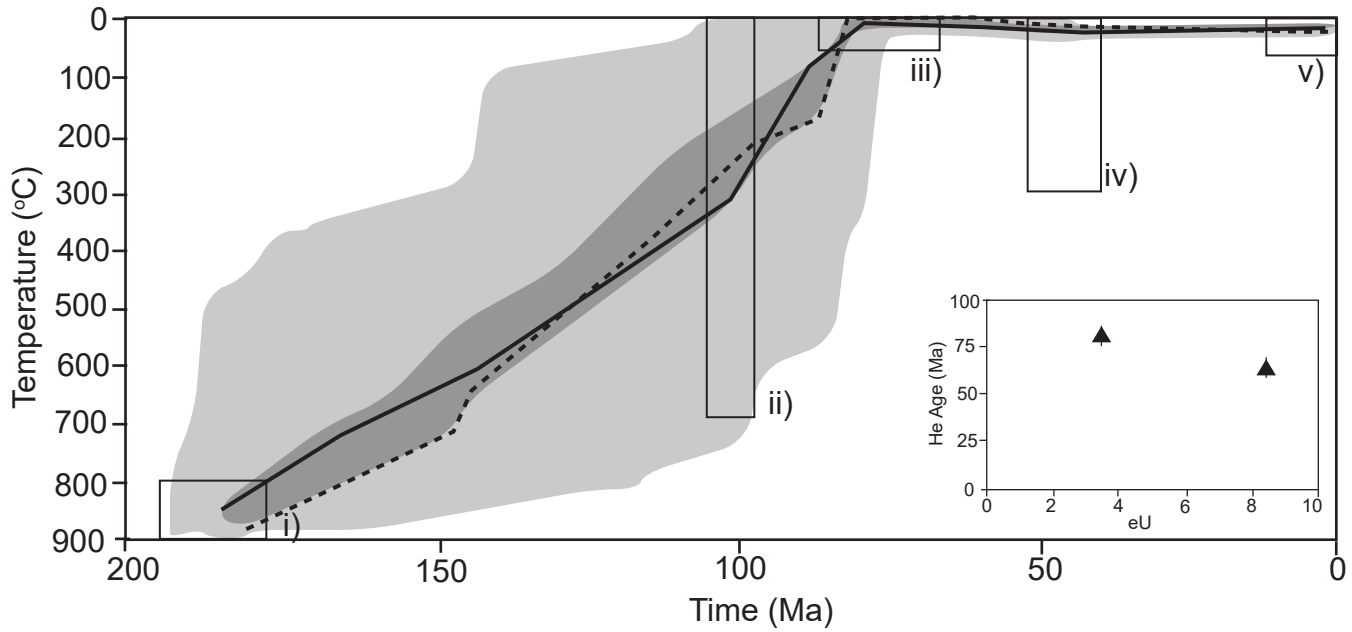

Figure 12 DR: Southeastern domain: Inverse model for sample 15RAY-MM003A01. 2 apatite grains (81.5 ± 6.7 Ma to 65.9 ± 4.6 Ma) were used to create the model. The constraint boxes include: i) crystallization ages, ii) Mount Nansen unconformity, iii) Carmacks unconformity, iv) potential Eocene event, and v) surface. Dark grey envelopes represent t-T pathways with a 'good fit' and light grey envelopes represent t-T pathways with an 'acceptable fit'. The thick black line represents the weighted mean path of the sample and the dashed line represents the line of best fit. The He age-eU plot in the bottom right corner illustrates apatite (triangles) grains from this sample that were used to make the inverse model.

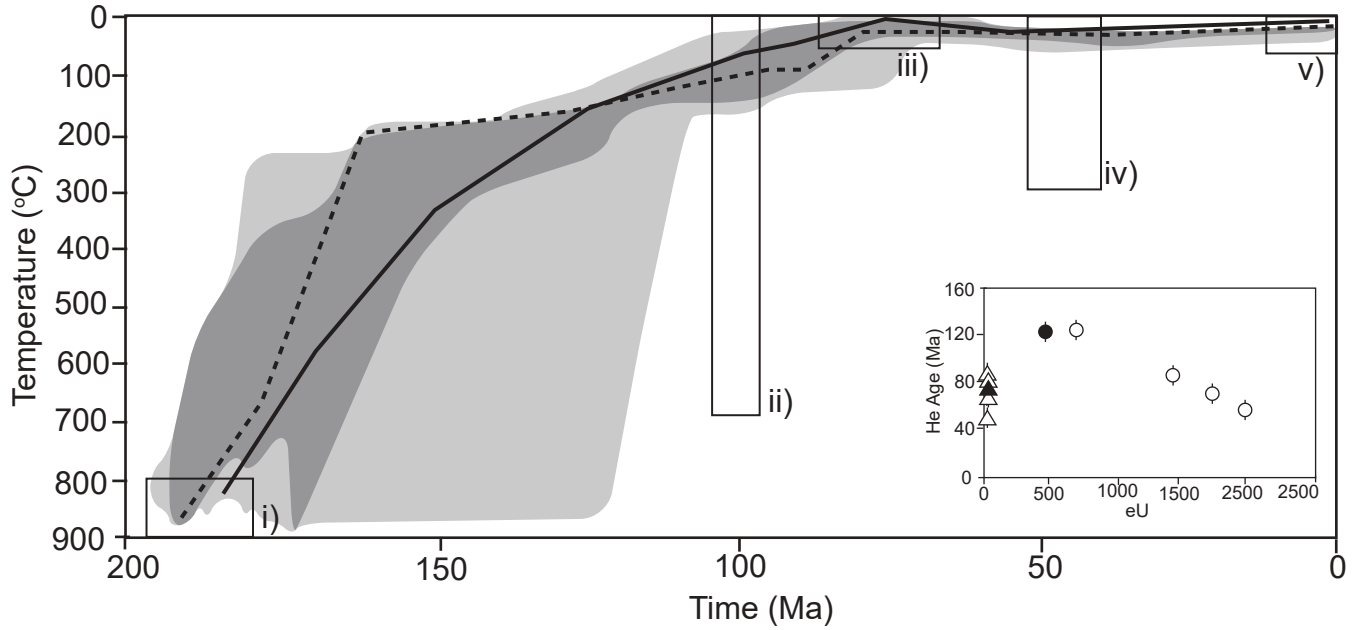

Figure 13 DR: Southeastern domain: Inverse model for sample 15RAY-JR120A01. 1 zircon grain (123.1 ± 9.3 Ma) and 1 apatite grain (70.2 ± 5.0 Ma) were used to create the model. The constraint boxes include: i) crystallization ages, ii) Mount Nansen unconformity, iii) Carmacks unconformity, iv) potential Eocene event, and v) surface. Dark grey envelopes represent t-T pathways with a 'good fit' and light grey envelopes represent t-T pathways with an 'acceptable fit'. The thick black line represents the weighted mean path of the sample and the dashed line represents the line of best fit. The He age-eU plot in the bottom right corner illustrates apatite (triangles) and zircon (circles) grains from this sample that were used to make the inverse model. Filled symbols indicate that the grain was used in the model, while unfilled symbols denote grains that were not used.

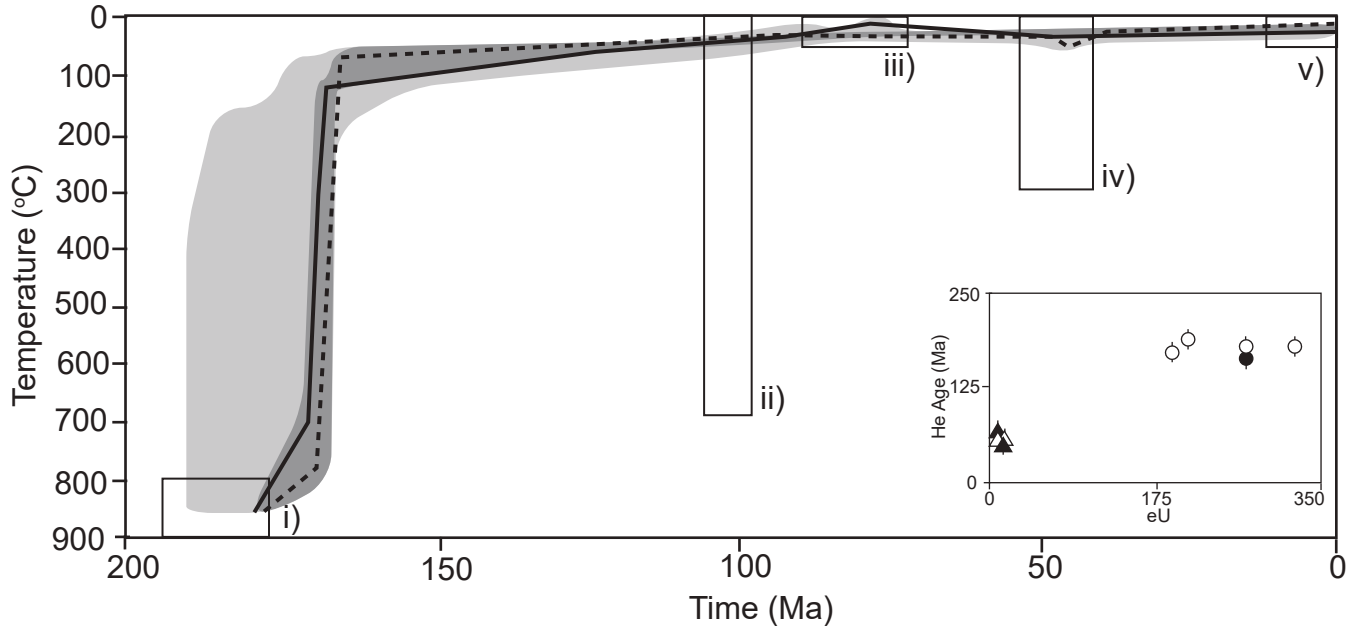

Figure 14 DR: Southeastern domain: Inverse model for sample 15RAY-JR092A02. 1 zircon grain (164.9 ± 11.7 Ma) and 2 apatite grains (68.4 ± 6.5 Ma to 52.1 ± 3.7 Ma) were used to create the model. The constraint boxes include: i) crystallization ages, ii) Mount Nansen unconformity, iii) Carmacks unconformity, iv) potential Eocene event, and v) surface. Dark grey envelopes represent t-T pathways with a 'good fit' and light grey envelopes represent t-T pathways with an 'acceptable fit'. The thick black line represents the weighted mean path of the sample and the dashed line represents the line of best fit. The He age-eU plot in the bottom right corner illustrates apatite (triangles) and zircon (circles) grains from this sample that were used to make the inverse model. Filled symbols indicate that the grain was used in the model, while unfilled symbols denote grains that were not used.

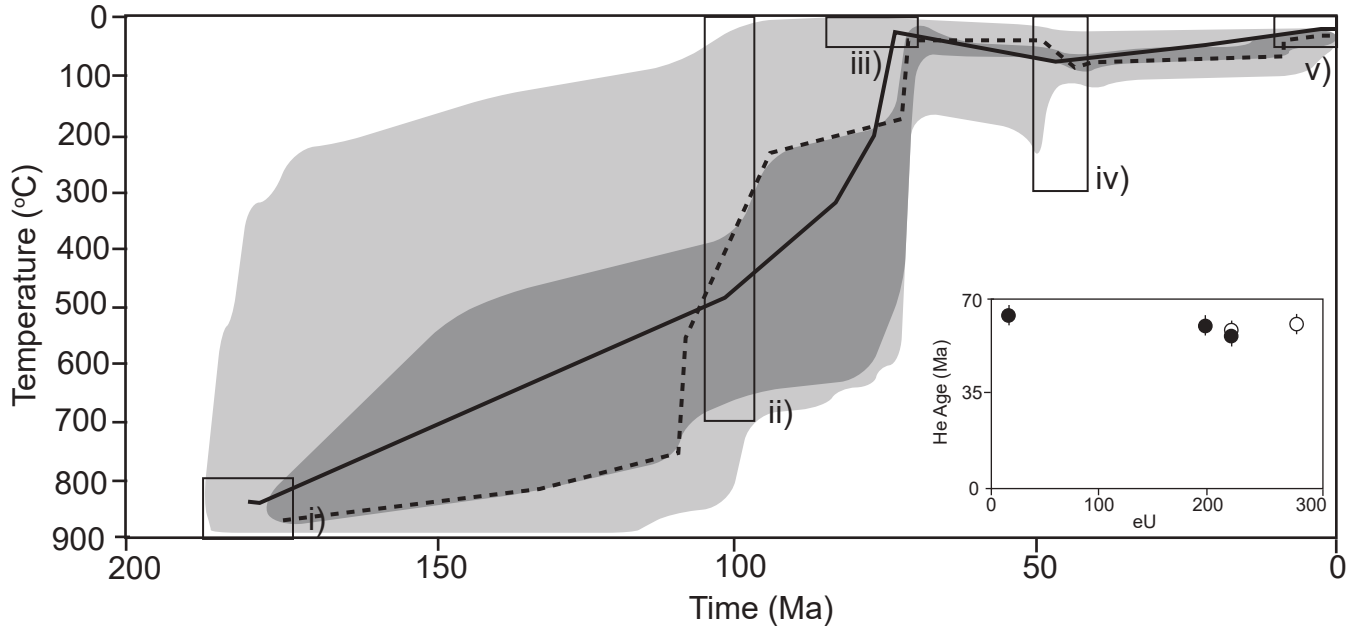

Figure 15 DR: Southeastern domain: Inverse model for sample 15RAY-JR061A03. 3 zircon grains (64.0 ± 4.6 Ma to 57.3 ± 5.4 Ma) were used to create the model. The constraint boxes include: i) crystallization ages, ii) Mount Nansen unconformity, iii) Carmacks unconformity, iv) potential Eocene event, and v) surface. Dark grey envelopes represent t-T pathways with a 'good fit' and light grey envelopes represent t-T pathways with an 'acceptable fit'. The thick black line represents the weighted mean path of the sample and the dashed line represents the line of best fit. The He age-eU plot in the bottom right corner illustrates zircon (circles) grains from this sample that were used to make the inverse model. Filled symbols indicate that the grain was used in the model, while unfilled symbols denote grains that were not used.

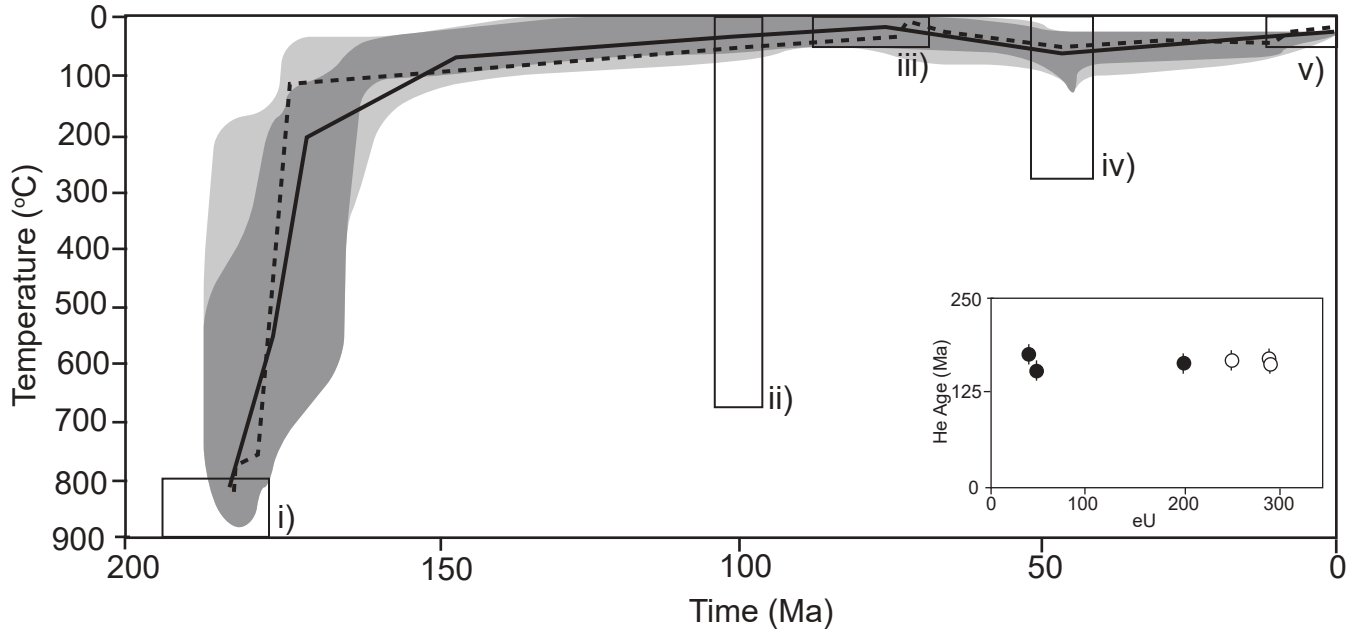

Figure 16 DR: Southeastern domain: Inverse model for sample 15RAY-EW014A01. 3 zircon grains (178.6 ± 12.6 Ma to 157.0 ± 10.3 Ma) were used to create the model. The constraint boxes include: i) crystallization ages, ii) Mount Nansen unconformity, iii) Carmacks unconformity, iv) potential Eocene event, and v) surface. Dark grey envelopes represent t-T pathways with a 'good fit' and light grey envelopes represent t-T pathways with an 'acceptable fit'. The thick black line represents the weighted mean path of the sample and the dashed line represents the line of best fit. The He age-eU plot in the bottom right corner illustrates zircon (circles) grains from this sample that were used to make the inverse model. Filled symbols indicate that the grain was used in the model, while unfilled symbols denote grains that were not used.

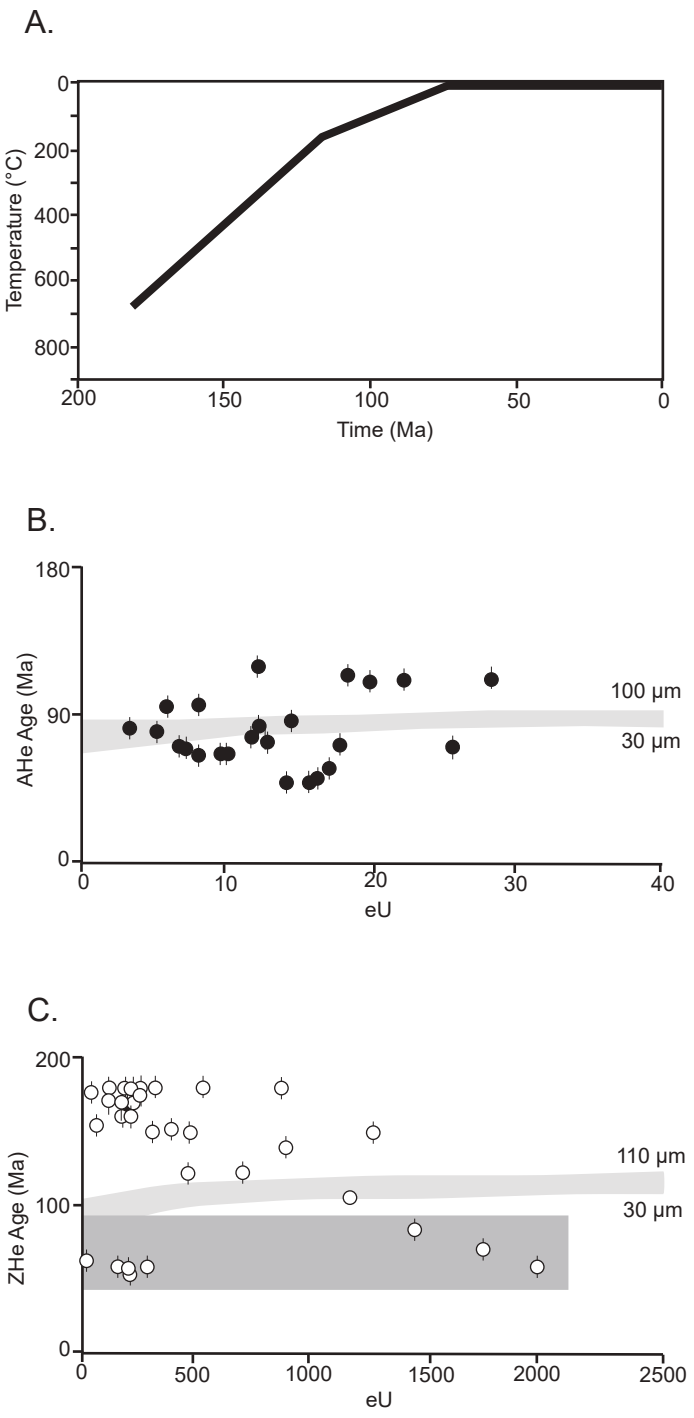

Figure 17 DR: Southeastern domain. **A**: Representative forward model of the Southeastern domain which does not demonstrate a plausible t-T path. The t-T pathway is derived from a earlier inverse model for sample 15RAY-MM009A01 that did not illustrate a plausible thermal path. **B**: Single crystal (U-Th)/He apatite cooling ages from the Southeastern domain plotted against eU. **C**: Single crystal (U-Th)/He zircon cooling ages from the Southeastern domain plotted against eU. The light grey polygon represents the range in grain size of apatite and zircon found in the Southeastern domain. The grains that are not within the ZHe envelope are from two samples (15RAY-JR120A01 and 15RAY-JR061A03 - highlighted in the dark grey polygon). Sample 15RAY-JR120A01exhibits high eU – young ages which can be explained by the helium diffusion kinetics. Sample 15RAY-JR061A03 displays moderate eU and young ages that are very close together which can be evidence of a sample that was quickly cooled.